First Measurement of the Differential Inclusive Cross Section for Jet Production at DØ Run II

by

Gregory Arthur Davis

Submitted in Partial Fulfillment
of the
Requirements for the Degree
Doctor of Philosophy

Supervised by

Professor Thomas Ferbel

Department of Physics and Astronomy
The College
Arts & Sciences

University of Rochester
Rochester, New York

2004

For my dedication, I cannot improve upon Exodus 20:12.

Curriculum Vitae

The author was born in New York, NY, on October 16, 1975. He attended Kenyon College from 1993 to 1997, and graduated with a Bachelor of Arts degree in 1997. He came to the University of Rochester in the Summer of 1997 and began graduate studies in Physics. While at Rochester, he received the Department of Education Graduate Assistance in Area of National Need Fellowship. He pursued his research in Experimental High Energy Physics under the direction of Professor Tom Ferbel and received a Master of Arts degree from the University of Rochester in 1999. In 1999, the author moved to Fermi National Accelerator Laboratory (Fermilab) where he joined the University of Rochester's group at the DØ experiment.

Acknowledgments

Professor Tom Ferbel has been an excellent adviser to me from the time I joined his group in 1998. I thank him for giving me the opportunity to work on the DØ experiment, which by any definition is awesome.

At DØ I met numerous other people whose help has been indispensable. First among these is George Ginther who has taught me so much and been like a second adviser to me at Fermilab. I also want to thank Marek Zieliński, Don Lincoln, Alexander Kupčo, Michael Begel, and John Krane whose help was so important to my analysis. In my other activities on DØ I have had the privilege of working with and learning from Alan Bross, Jadzia Warchol, Juan Estrada, and Drew Alton. There are also many of my contemporaries, too many to name, who have become good friends of mine. I hope I have contributed half as much to them as they have helped me.

I also wish to thank my father Michael Davis who took an adult astronomy class with me while I was in grade school and my mother Madelyn Ollendorff Davis whose advice I have always prized.

I must further acknowledge The United States Department of Energy, The National Science Foundation, and the numerous international funding agencies whose confidence was needed to make DØ a reality.

Abstract

The differential inclusive jet cross section in proton-antiproton collisions at a center of mass energy of 1.96 TeV reaches the smallest distances or equivalently the highest momentum transfers ever probed. We present a preliminary measurement of jet production from the DØ experiment at Run II of the Tevatron. Next-to-leading-order QCD calculations of the cross section are consistent with the data over seven orders of magnitude.

Contents

List of Figures

List of Tables

Chapter 1

The Energy Frontier

One of the most basic questions a scientist can ask about almost anything is: "what is this made of?" Modern science has answered this to a remarkable degree. By the beginning of the twentieth century, scientists had determined that all visible matter in the universe was made of atoms, and they formulated the periodic table of elements. While the table did not list every element that can be found in nature, and new ones have since been manufactured, this was a major success that lead to great progress in answering the above fundamental question. Some scientists believed that atoms were entirely indivisible, but nobody had yet applied enough energy to completely rip them apart and see what they were made of. Chemical reactions typically involve energies of no more than a few eV (electron Volts) per atom, not enough to break them apart.

Early x-ray work reached energies of keV (10^3 eV) but this too was insufficient to break atoms.

There were hints that atoms might be divisible. The electron and other forms of radiation were discovered before the end of the nineteenth century. In the early part of the twentieth century, scientists learned that atoms contained electrons and a positively charged nucleus. The discovery of the nucleus required hitting atoms with other particles that had kinetic energies of several MeV (10^6 eV). Doing this experiment required the use of energetic natural radiation that was also discovered near the turn of the century.

By the mid 1930s, scientists determined that matter was made of three types of particles: electrons, protons, and neutrons. Much of this knowledge came from scattering experiments, the most famous of which was done in Ernest Rutherford's laboratory in 1911. By scattering naturally occurring α particles off thin gold foil, his group discovered that gold atoms have hard cores at their centers. The energy of the naturally occurring α particles was about 6 MeV. With this energy, they could easily penetrate the atom, but not the nucleus. Discovering protons and neutrons in the nucleus required similar energies, but smaller target nuclei. To dig any deeper required higher energies, far beyond the reach of natural radiation.

To probe the nature of electrons, protons, and neutrons requires accelerators.[1] Using primarily accelerator-based experiments, physicists in the twentieth century have constructed the Standard Model of particle physics. In the Standard Model, the electron is a fundamental particle, but the neutron and proton are composites made of indivisible quarks and gluons. As the energy frontier moves forward, we will probe these particles at even smaller distance scales always asking: "what is this made of?" References to all of these discoveries and much more can be found in Ref. [1].

This thesis reports research performed at Fermi National Accelerator Laboratory's Tevatron, currently the world's highest-energy accelerator, where we study the highest energy $p\overline{p}$ collisions. The name Tevatron comes from TeV.

$$1 \text{ TeV} = 1000 \text{ GeV} = 10^{12} \text{ eV} \tag{1.1}$$

We are following the tradition of Rutherford, probing the structure of the proton at the smallest distances we can attain.

[1] Cosmic rays come to earth from space and they can have extremely high energies. These have been used for studying many issues in particle physics, but, unlike particle beams from accelerators, they constitute a poorly controlled laboratory. Accelerators can provide many collisions at a fixed energy; with cosmic rays, you get what comes.

1.1 The Tevatron

Fermilab's Tevatron collides 980 GeV protons with 980 GeV antiprotons at two positions in its ring, B0 and D0, with 396 ns between $p\overline{p}$ crossings. D0 is the site of our DØ experiment, and B0 is the site of CDF, another general-purpose detector. Run II of the Tevatron commenced in March 2001, and is expected to continue until about 2008.

The Tevatron is the largest accelerator in a series of machines that are essential for providing the $p\overline{p}$ collisions at DØ . These machines are the Cockroft-Walton, the Linac, the Booster, the Main Injector, and the Tevatron. Each of these machines takes protons to ever higher energy, at which point they can be inserted into the next accelerator [2]. Figure 1.1 shows the layout of the Fermilab accelerator complex.

Other than the Cockroft-Walton and Linac, each of the accelerators is a synchrotron. In a synchrotron, the particles are accelerated in a beampipe that is approximately circular. Synchrotrons contain dipole magnets to keep the particles circulating through the pipe and quadrupole magnets to keep the beam focused. They also have radio frequency (RF) electric fields at one or more positions around the ring to increase particle energy. As the RF accelerates the particles, the confining magnetic fields are increased to keep the particle trajectories within the vacuum pipe. Each accelerator has both a minimum

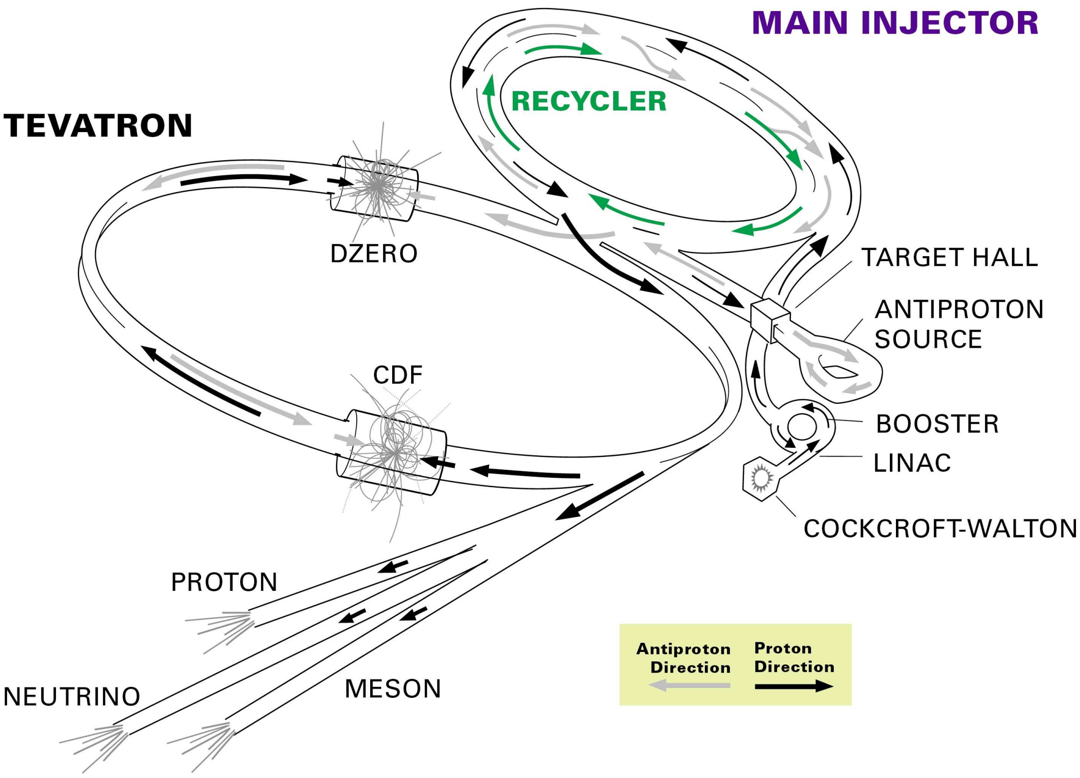

Figure 1.1: Schematic overview of Fermilab's accelerator complex

and maximum energy for which it can hold the beam, and this is why there is a chain of accelerators. The Tevatron's magnet coils are made of superconducting niobium/titanium, which operate at ≈4 K with a magnetic field in excess of 4 T. The other synchrotrons use water cooled copper wire in iron-core magnets that cannot achieve nearly as high currents or magnetic fields.

Using a system of rectifiers to create a high voltage gap, the Cockroft-Walton, also called the Preacc, accelerates a beam of H^- ions to an energy of 750 keV. A linear accelerator, called the Linac, takes the H^- up to 400 MeV, after which they are injected into the Booster.

As the H^- ions are being inserted into the Booster, they are bent by the same magnetic field as the protons already inside. The two beams hit a foil that strips the electrons from the negative ions. All of the particles that pass through the foil are protons that get accelerated in the machine.

Taking protons from the Cockroft-Walton through all the accelerators, up to 980 GeV in the Tevatron, takes about ninety seconds [3]. Preparing the antiproton bunches for collision is far more challenging [4]. The first step is to accelerate a bunch of protons to 120 GeV in the Main Injector and then to put it on a nickel target. This creates a spray of secondary particles. Negatively-charged particles with momentum of $\approx$8 GeV/c are channeled to the Antiproton Source. Every million protons that impact the target yields about twenty usable antiprotons. The antiprotons are focused by a lithium lens and "cooled" [4] into bunches that can be inserted into the Main Injector and then into the Tevatron. Antiprotons are the only particles from the spray that survive the long cooling process.

During the run, the accelerator complex operates continuously in "stack and store mode." While collisions are taking place in the Tevatron (using the present "store"), a new "stack" of antiprotons is generated and cooled in the Antiproton Source. Imperfections in the magnets and the vacuum, as well as the mutual electrostatic repulsion of the protons in the beams, cause particles to be lost so the beam in the Tevatron degrades over time. Thus, the instantaneous luminosity, or, equivalently the number of collisions per crossing, drops with time. When the stack is large enough, the operating store is aborted, and new protons and antiprotons are injected into the Tevatron and accelerated to maximum energy to begin a new store.

Figure 1.1 also includes items that are not used in collider operations. The "proton," "neutrino," and "meson" beamlines are used for fixed-target experiments. These have lower center-of-mass (CM) energies, but can reach higher luminosities than the Collider. The Recycler is a storage ring made of permanent magnets that is situated in the same tunnel as the Main Injector. There are different plans for using this ring, and one that is particularly interesting involves electron cooling of antiprotons [5].

1.1.1 Run II

Tevatron Run II, the source of the data in this thesis, officially commenced on March 1, 2001. Over two years later, improvements are still being made to both the accelerator and to the detectors, but there have been great strides forward. The work presented in this thesis represents preliminary results from Run II.

Run II was marked primarily by the replacement of the old Main Ring with the Main Injector. In Run I, each of the colliding beams had 900 GeV, for a center-of-mass energy ($\sqrt{s}$) of 1.8 TeV; we now have beams of 980 GeV, for a $\sqrt{s}$ of 1.96 TeV. The upgraded accelerator complex also provides more luminosity. In Run I, there were six bunches of protons and six bunches of antiprotons with a crossing every 3500 ns. The complex now provides 36 bunches of protons and of antiprotons in the collider separated into three super bunches. Each super bunch has twelve bunches separated by 396 ns [2].

Substantial changes in both the DØ and CDF detectors were made between the end of Run I in 1996 and the beginning of Run II. Many were mandated by the change in accelerator timing and increased luminosity, but others were made to add new capabilities. DØ added a central solenoid magnet and all-new tracking. For a further discussion of the detector, see Chapter 3.

1.2 The Large Hadron Collider

The Large Hadron Collider (LHC) at CERN in Geneva, Switzerland is expected to take the energy frontier away from Fermilab by the end of this decade [6]. The LHC is still under construction, with magnets and detectors being built all over the world, including Fermilab. The accelerator is located in the 27 km circular tunnel that was previously used for the Large Electron Positron (LEP) Collider. The LHC specifications call for proton on proton collisions at $\sqrt{s} = 14$ TeV, with luminosities about one hundred times greater than at the Tevatron. This improved energy and luminosity will provide greater reach in the search for new physical phenomena. The LHC is the future energy frontier.

Chapter 2

The Physics of Jets

When protons and antiprotons collide at high energies (say 1.96 TeV) one of four types of reactions can take place: elastic, diffractive, soft-inelastic, or hard scatters. Elastic collisions are billiard-ball like interactions, where the initial particles and final particles are of the same type. That is, the proton and antiproton remain whole throughout the collision.

Elastic scattering can be regarded as a diffractive process involving the exchange of quantum numbers of the vacuum. Inelastic diffraction is similar, but one or both of the incident particles break apart. These events often leave striking signatures called "rapidity gaps" in the distribution of final products [7]. These gaps are bands in rapidity (Section 2.1.1) where no particles are emitted.

Soft inelastic collisions also involve the breakup of the incident hadrons, but at low momentum transfers. Momentum transfer, conventionally referred to as Q^2, is the change of momentum of each of the incident particles. These events can often be characterized by exchanges of virtual hadrons, and comprise the largest part of the total $p\overline{p}$ cross section. By counting these events, we can normalize our other measurements to this total cross section.

A hard scatter occurs when constituent partons within the proton and antiproton interact directly. The incident particles break apart and many new particles come into existence. These particles arise from the hard scatter of the partons, as well as from the breakup of the remnants of the incident hadrons, the latter being often called the "underlying event". Hard collisions involve the largest energy and momentum transfers, probe deeply into the structure of hadrons, and are of the greatest interest. DØ and CDF both spend the majority of their resources studying different types of hard collisions. This thesis is about a specific type of hard scattering, to be described below.

2.1 Characterizing Jets

The majority of hard-scatter events contain collimated sprays of hadrons called jets. Usually, each jet has much more transverse momentum than the particles in the underlying event. Jets can be characterized by an energy-momentum four-vector, which is the sum of the four-vectors of all the particles that comprise the jet, and can be parametrized in terms of its energy (E) and the three Cartesian components of momentum. By convention, the z axis is chosen to be the direction of the incident proton, the y axis upward vertical, and, for a right handed coordinate system, the x axis is then chosen to be horizontal and pointing away from the center of the ring. It is useful to define another parameterization for four-vectors:

$$\begin{array}{lll} \text{mass} & m & = \sqrt{E^2 - p_{\mathrm{x}}^2 - p_{\mathrm{y}}^2 - p_{\mathrm{z}}^2} \\ \text{transverse momentum} & p_T & = \sqrt{p_{\mathrm{x}}^2 + p_{\mathrm{y}}^2} \\ \text{rapidity} & y & = \frac{1}{2}\ln\left(\frac{E+p_{\mathrm{z}}}{E-p_{\mathrm{z}}}\right) = \operatorname{arctanh}\left(\frac{p_{\mathrm{z}}}{E}\right) \\ \text{azimuthal angle} & \phi & = \arctan\left(\frac{p_{\mathrm{y}}}{p_{\mathrm{x}}}\right) \end{array}$$

This parameterization is particularly useful because all of the variables except for rapidity are invariant with respect to Lorentz boosts along the z axis. Rapidity transforms in a special way that is described in the next section.

2.1.1 Rapidity and Pseudorapidity

The polar angle θ, defined as:

$$\theta = \arctan\left(\frac{p_T}{p_{\mathrm{z}}}\right) \tag{2.1}$$

is a more obvious variable than rapidity, but not as useful. Rapidity is a useful variable because a Lorentz boost along the z axis adds a constant value to the rapidity of every particle, making differences in rapidity invariant to such transformations. Thus, an event containing two particles with rapidities y_1 and y_2 has a $\Delta y \equiv y_1 - y_2$, which is independent of boosts along the z axis. Furthermore, the shape of the distribution of particle rapidities in an event is invariant to such Lorentz boosts. Rapidity is also preferable to θ, because many particles are produced clustered close to $\theta = \pi/2$ in the center of mass, and rapidity stretches out this region.

We also define a pseudorapidity:

$$\eta \equiv -\ln\left[\tan\left(\frac{\theta}{2}\right)\right] \tag{2.2}$$

Pseudorapidity is the limit of rapidity as the mass of an object becomes insignificant relative to its momentum. For simplicity, we will use η and ϕ coordinates to define the position of a jet or particle.

2.1.2 Mass of a Jet

The energy-momentum four-vector that describes a jet represents a massive system. The mass can come from two sources, first of which is the mass of the individual particles that comprise the jet. Most of the particles in a jet are pions with a mass of $\approx$0.14 GeV/c^2. Jets can also contain more massive particles, but there are few of them. The major contribution to the mass of a jet comes from the relative momenta of the particles, and in our calculation of jet mass, this is the only contribution we used.

2.1.3 The Improved Legacy Cone Algorithm

It is usually easy to point out jets in our events. By their very nature, jets stand out. However, it is not possible to look at every event by eye. Even if we could, while the presence of most jets would be obvious, which particles near the edges of jets ought to be included would still be open to debate. To solve this problem, an algorithm is needed that can be used to identify jets in every event. The algorithm we use was developed jointly by DØ and CDF before Run II started, and it has been whimsically dubbed the "Improved Legacy Cone Algorithm" or ILCA [8].

The algorithm is used for clustering particles, partons, or energy depositions in a detector, generically called "objects." The basic idea is to find all of the circles in $(\eta,\ \phi)$ space (cones in three space) of a preselected fixed radius R that contain "stable" jets.

Each object in an event is assigned a massless four-vector with the object's energy that points along the object's direction. Some of these objects are then chosen as "seeds" for later stages in the algorithm. Such seeds correspond to objects with a p_T greater than some chosen threshold value. Then, for every object, we define a radius r to any seed:

$$r \equiv \sqrt{(\phi_{object} - \phi_{seed})^2 + (y_{object} - y_{seed})^2} \tag{2.3}$$

If r is less than our chosen radius R, the object has its four-vector added to the seed's four-vector to create a "preprotojet" four-vector:

$$p_{\text{preprotojet}} = \sum_{r_j < R} p_j \tag{2.4}$$

where $p_{\text{preprotojet}}$ is the four-vector for the preprotojet, and p_j is the four-vector associated with the j^{th} object.

If the distance between $p_{\text{preprotojet}}$ and p_{seed} in $(\eta,\ \phi)$ is sufficiently small, the cone is said to be stable, and the preprotojet becomes a "protojet". If that distance is too large, then the direction of $p_{\text{preprotojet}}$ is used as the seed, and the process is repeated. This continues until stability is reached, namely when the angle between the center of the cone and the four-vector comprised from the sum of all the objects in the cone is sufficiently small. If a stable cone is unique, meaning that it has not been found by starting from another seed, it is then added to the list of protojets. For considering whether a cone is stable and whether a preprotojet is unique, the direction of the two four vectors is compared, if they are more than 10^{-6} apart in $(\eta,\ \phi)$ they are considered different, otherwise they are the same.

Once all seeds are used, the algorithm focuses on the midpoints between protojets. It takes the sum of every pair of protojets that are within $2R$ of each other, and uses that sum as a new seed. These seeds are used in the same way as the previous seeds, and, if they yield unique stable cones, they too are added to the list of protojets.

Such cones are called protojets rather than jets because they may overlap in $(\eta,\ \phi)$ space. To deal with this, we use a splitting and merging procedure, based on a single parameter called the split/merge fraction, f. The value of f is defined to lie between zero and unity. A low value of f leads to more splitting and more smaller jets, while a high value yields more merging and fewer larger jets.

The protojet with highest p_T is considered first. If it does not share any objects with another protojet, it becomes a jet. If there is sharing, the neighbor with highest p_T is examined. If the shared objects constitute less than f of the p_T of the smaller jet, then they are split with half of the space going to each jet and both are returned to the list of protojets. If the sharing exceeds f, the two protojets are merged, and only one is returned to the list of protojets. In either case, the new protojets no longer comprise stable cones, but their four-vectors are still well defined by the sum of their objects.

For this analysis, the seed threshold is $p_T > 1$ GeV/c, $f = 0.5$, and $R = 0.7$, as suggested in Ref. [8]. Jets with less than 8 GeV/c of transverse momentum are not kept. The objects in DØ data correspond to calorimeter towers that are 0.1×0.1 in $(\eta,\ \phi)$ space. These towers were constructed to have projective geometry at the center of the detector (z = 0). In practice, the positions of the hard scatter interactions, called event vertices, are distributed along z with an RMS of ≈25 cm about z = 0, and are reconstructed using data from our tracking detectors. A tower's four-vector is assigned to have the energy measured in the tower and its momentum points from the reconstructed location of the vertex to the tower's center. For more about the DØ detector, see Chapter 3.

2.1.4 Other Jet Algorithms

Other jet clustering algorithms have been used at different times by different collaborations. Most of these are either cone algorithms similar to ILCA or in the class called k_T algorithms that are more flexible in terms of varying sizes and shapes. Cone algorithms are preferred for use in busier environments, such as those of $p\overline{p}$ collisions at the Tevatron and pp collisions at the LHC. Experiments in lower-multiplicity environments, such as ep and e^+e^- colliders, where there is less of a problem from underlying events, tend to use k_T algorithms.

During Run I of the Tevatron, DØ and CDF used fixed cone algorithms to define jets. Those algorithms used somewhat different techniques for clustering, and CDF's had a system called "ratcheting" built into it. Ratcheting was used to prevent a cone from moving too far away from its seed. In some cases, an event display appears to have two jets close to each other, but the jet algorithm finds only the larger of the two apparent jets. The seed inside the smaller jet gives rise to protojets that migrate to the large jet. CDF has shown event displays with what appears to be a $\approx$60 GeV jet that was not reconstructed because it was too close to another larger jet [9].

Although ILCA is a more elegant fixed-cone algorithm, it too seems to have the same characteristic. CDF has shown that this algorithm can also lose apparent jets of large p_T. Other than ratcheting, a solution that DØ and CDF have considered involves a smaller "search cone" [9]. That is, instead of using the full cone to find jets, a smaller cone is used first. Then, once the jet is found, all of the energy from the larger radius is added into it. This work is still ongoing; a new algorithm has yet to be adopted by DØ and CDF. For now, any clusters of energy that are not reconstructed as jets are not called jets. Fortunately, we know this is a very small effect. Thousands of events were scanned to find any events showing this kind of effect.

Another jet algorithm used at DØ is the "simple cone" algorithm. This algorithm is like the ILCA algorithm, except that it does not use the midpoint of protojets for extra seeds and it does not do any splitting and merging of protojets. Also, rather than add four-vectors it adds the E_T of every tower in the jet to get a total transverse energy ($E_T \equiv E\sin(\theta)$). This algorithm cannot be used for offline analysis, where events must be studied in detail and the number of jets in an event is significant. However, it is useful for triggering where all we need to see is if there is significant energy in jets and the algorithm must run quickly. We use this algorithm in our Level 3 trigger, which is described in Section 3.9.

2.2 QCD

The theory that describes jet production is called quantum chromodynamics, or QCD, and is the gauge theory of the strong (or color) interactions. These are interactions among quarks and gluons. Quarks are spin 1/2 fermions that carry color charge. They come in six flavors (three weak isospin doublets) that have different masses and electric charge [10]. The up-type quarks have an electric charge equal to +2/3 e, while the down-type quarks have an electric charge of –1/3 e.

There are three kinds of color charge, conventionally called blue, green, and red. Colored objects do not seem to exist in nature; instead, quarks form

	First Generation	Second Generation	Third Generation
$Q = +2/3$ e	up (u) 1 - 5 MeV/c^2	charm (c) 1150 - 1350 MeV/c^2	top (t) 174 GeV/c^2
$Q = -1/3$ e	down (d) 3 - 9 MeV/c^2	strange (s) 75 - 170 MeV/c^2	bottom (t) 4.0 - 4.4 GeV/c^2

Table 2.1: The quark masses

baryons and mesons, collectively called hadrons, that are all colorless. Baryons, such as protons and neutrons, can be described as systems with three "valence" quarks. A proton contains one down and two up valence quarks, and a neutron two down and one up quark. Each of these three quarks has a unique color, and the combination is said to be "colorless" or equivalently a color singlet.

A meson contains one valence quark and one valence antiquark of the opposite color. For example, a π^- meson consists of a colorless combination of a down quark and an anti-up quark. The quarks in a meson can be blue and anti-blue, green and anti-green, or red and anti-red. Because these states are entirely indistinguishable, a meson is a superposition state of all three. With only a few exceptions, this elementary quark model accommodates all known baryons (fermions) and all known mesons (bosons) [10]. It also predicts that every hadron has an electric charge that is an integral multiple of the electron charge, and this too is consistent with all observations. The recent discovery of the new hadron X(3872) [11] suggests that there are also five quark baryons ($qqqq\overline{q}$).

Because quarks are found only in bound states, their masses are ill defined, as can be seen in Table 2.1. The top quark is an exception because it decays before it binds with other quarks to form a hadron. Like the other quarks, no bare top quark has ever been observed in a detector, but because it decays before a hadron forms, its mass can be determined from its decay products with a smaller ambiguity.

Gluons are the field particles of QCD. They are vector bosons that carry color but no electric charge. Because gluons carry color charge, they can interact with each other. Figure 2.1 shows the fundamental interaction vertices of QCD.

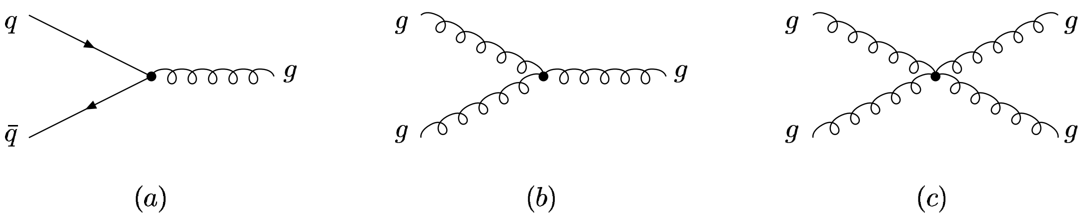

Figure 2.1: The fundamental Feynman diagrams for QCD. (a) shows how gluons and quarks interact with each other. (b) and (c) show two types of gluon self interactions.

The vertices marked (a) and (b) in Fig. 2.1 contribute an order of α_s to cross section calculations, while (c) contributes order ${\alpha_s}^2$. A leading order calculation of $q\overline{q} \rightarrow q\overline{q}$ would use diagrams like those found in Fig. 2.2.

More precise next-to-leading order (NLO) calculations of $q\overline{q}$ scattering, go to third order in α_s and introduce a third parton in the final state. Figure 2.3

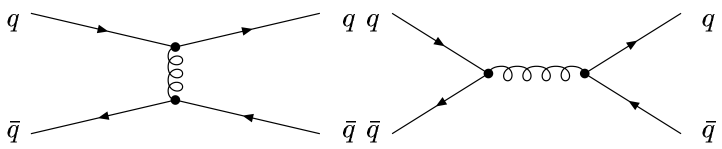

Figure 2.2: The leading order diagrams for quark anti-quark scattering.

shows some of these diagrams.

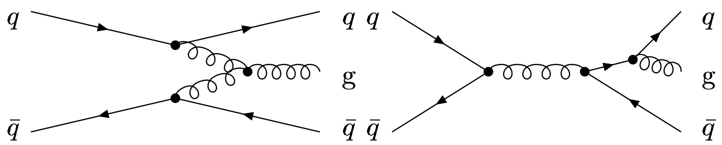

Figure 2.3: Some NLO diagrams for quark anti-quark scattering.

In order to obtain useful results from perturbative calculations, it is essential that higher order terms in the expansion (diagrams with more vertices) contribute less than lower-order terms. At distances of the order of the proton radius, 1.5×10^{-15} m, the strong-force coupling parameter, α_s, is of the order of unity, making perturbative calculations impossible. However, as distances become smaller, α_s decreases, thereby making perturbative calculations for high energy scattering reliable. The formula for this "running coupling constant" is:

$$\alpha_s(|Q^2|) = \frac{12\pi}{(11n_c - 2n_f)\ln(|Q^2|/\Lambda^2)} \tag{2.5}$$

where n_f is six, the number of of quark flavors, and n_c is three, the number of colors. Λ is the scale factor of QCD with units of energy that is defined as follows:

$$\Lambda^2 = \mu_r^2 \exp\left(\frac{-12\pi}{(11n_c - 2n_f)\alpha_s(\mu_r^2)}\right) \tag{2.6}$$

where μ_r is the renormalization scale that is discussed below [10].

2.3 QCD Calculation of the Jet Cross Section

A leading order (LO) picture of a hard scatter at the Tevatron is that a parton (quark, antiquark, or gluon) from within the colliding proton and a parton from the antiproton interact. The outcome is that the partons are ejected while the colored remnants of the incident proton and antiproton travel along the direction of the beampipe. The most common hard scatter is where the two incident partons scatter off each other through a QCD interaction and then recede in new directions. The gluon field from the colored objects creates new particles, most of which are emitted along the direction of motion of the colored objects, thereby creating jets. Perturbative calculations are good for calculating hard collisions of partons. However, they fail to account for the energy regime of parton fragmentation or hadronization.

The process of hadronization (evolution of a colored parton into a colorless jet) is not a major concern in this analysis. We assume that the reconstructed jet has essentially the same four-vector as the final-state parton that gave rise to it. A good jet algorithm should have this quality, and that was one of the ideas that went into designing ILCA [8].

The inclusive differential cross section for producing one parton and anything else (X) in $p\overline{p}$ collisions is given by:

$$\frac{d\sigma(p\overline{p} \rightarrow jet + X)}{dp_{T\,jet}} = \sum_{ijk} \int_0^1 \int_0^1 dx_p dx_{\overline{p}} f_{i/p}(x_p, Q^2) f_{j/\overline{p}}(x_{\overline{p}}, Q^2) \frac{d\hat{\sigma}(ij \rightarrow k + X)}{dp_{T\,k}} \tag{2.7}$$

where i, j, and k represent all of the types of partons, with i the interacting parton from the incident proton and j from the antiproton. x_p is the Bjorken x variable which is the fraction of the proton's momentum that is carried by the interacting parton; $f_{i/p}(x_p)$ is the parton distribution function (PDF) that reflects the probability that a parton of type i carries the fraction x_p of the momentum of a proton; $\hat{\sigma}(ij \rightarrow \ k + X)$ is the perturbative cross section for partons i and j to yield parton k and X. Parton k gives rise to a jet. The total cross section diverges at small p_T. The probability for a parton to emit another parton grows indefinitely as the energy of the emitted parton goes to zero. Predictions must therefore be restricted to regions where that energy is sufficiently high and the calculation reliable. We will measure the dependence of the cross section on jet transverse momentum for jets with $p_T > 60$ GeV/c in a restricted pseudorapidity range. We expect that this p_T should be high enough that the theory calculations should be reasonably accurate [12].

The calculation uses a minimum cutoff value for the square of the four-momentum transfer in the initial collision (Q^2), and considers emitted partons of sufficient energy, where sufficient means they are of the order of the renormalization scale of the perturbative calculation (μ_R). For our calculations, we use $\mu_R = \frac{1}{2}\, p_{Tmax}$, where p_{Tmax} is the transverse momentum of the "leading" jet, the jet with the highest p_T.

As we have indicated, the PDFs, represented in Eq. 2.7 by $f_{i/p}(x_p)$ and $f_{j/\overline{p}}(x_{\overline{p}})$, reflect the probability density of having any given parton inside the proton or antiproton with momentum fraction x_p or $x_{\overline{p}}$. Although these functions cannot be calculated from first principles through QCD they can be evolved as a function of x and Q^2 according to the DGLAP equation [13]. The PDFs are independent of the final state and are the same for $p\overline{p} \rightarrow$jets as for $p\overline{p} \rightarrow t\bar{t}$, Z or any other final state, and can be extracted from fits to a variety of collisions [14].

Electromagnetic interactions between electrons and quarks are well understood. Using this understanding, the PDFs of the quarks have been evaluated over the years by numerous experiments [15] including the latest studies from Zeus [16] and H1 [17] experiments at DESY where they collide electrons or positrons with protons at high energy. The PDFs for gluons are harder to measure. They have been extracted, with larger uncertainty, from past pp and $p\overline{p}$ data, including jet production from DØ [18] and CDF [19] in Run I.

To calculate the jet cross section, we use the PDFs for all partons, as extracted by the MRST2001 [20] and CTEQ6M [21] collaborations. Despite very similar data sets, the cross section obtained using these two PDFs differ by $\approx\pm10\%$.

The calculation of the jet cross section requires an appropriate scale for the evolution of PDFs from some Q^2 value, where the PDFs are known, to the scale appropriate for the collision. This scale is called the factorization scale (μ_F), and is also usually defined to be proportional to the p_T of the leading jet. We use $\mu_F = \mu_R = \frac{1}{2}\, p_{T max}$. The renormalization scale and factorization scale were chosen because they make the calculation of the cross section at leading order and next-to-leading order similar.

2.3.1 Evolving Jets from Partons

Perturbative QCD deals with gluons and quarks. In leading-order (LO) calculations, programs such as HERWIG [23] and PYTHIA [24] are used to transform partons into jets. Because every term at LO has some positive probability associated with it, simulating collisions and evolving them to full events can yield a cross section calculation. However, in more precise next-to-leading-order (NLO) calculations, generated events cannot be counted and jets evolved because there are terms in the perturbative expansion that, due to interference, give rise to negative rather than positive contributions to the production cross section. For this reason, NLO programs only calculate cross sections for partons at various trajectories.

If the emitted partons are sufficiently close together in $(\eta,\ \phi)$ space, then ILCA will group them into a single jet, and, if they are further apart, then ILCA will find two jets. If the transition occurs at some constant separation, $R_{sep} \times\ R$, for the cone of radius R, then R_{sep} can be extracted by analyzing the data. We looked at the distance between jets in our data and saw that the center of two jets was rarely closer than 0.91. From this, we concluded that $R_{sep} = 1.3$ was a good choice [22]. Partons within $1.3 \times 0.7 = 0.91$ of each other in $(\eta,\ \phi)$ are merged into single jets in our calculation.

2.3.2 The Calculation

We calculated the cross section using JETRAD [25], which provides both LO and NLO calculations of QCD observables through Monte Carlo techniques. We used the values for the parameters R_{sep}, μ_R, and μ_F given previously. For these parameters, the LO and NLO results are very similar, which is why we chose these values. These QCD calculations are presented in Chapter 8.

2.4 Measuring the Jet Cross Section

The final cross section presented in Chapter 8 is binned in transverse momentum. The value for each bin is calculated with the following formula:

$$\left\langle \frac{d\sigma}{dp_T} \right\rangle \Bigg|_{p_{T\,average}} = \frac{N_{jets}}{L \times \Delta p_{T\,bin}} \tag{2.8}$$

where N_{jets} is the number of jets in the bin, $\Delta p_{T\,bin}$ is the width of the bin in GeV/c, and L is the integrated luminosity measured in pb^{-1}. There are numerous corrections that are applied to the number of jets that are extracted from the data.

The total cross section for $p\overline{p}$ collision at 1.8 TeV was measured by two experiments in Run I of the Tevatron [26][27]. The luminosity is determined by counting the number of interactions and dividing by the cross section. The details of this process, as well as the theoretical calculations used to extrapolate the cross section to 1.96 TeV, are found in Ref. [28].

Chapter 3

The DØ Experiment

The DØ Collaboration consists of over 600 physicists from 83 institutions in 19 countries [29]. The collaborators designed, built, and are operating the detector, which is pictured in Fig. 3.1, with an enlargement of the central tracking region shown in Fig. 3.2. Being a collaborator offers the privilege of analyzing the interesting data. This chapter provides a description of the detectors that are relevant to this analysis, and a description of how they are used. For a more complete discussion of the detector, see Refs. [30][31].

The Run II DØ detector is essentially a brand new device. While some components, such as the calorimeter, have been retained from Run I, even this element has new electronics to operate in the new environment of more frequent collisions.

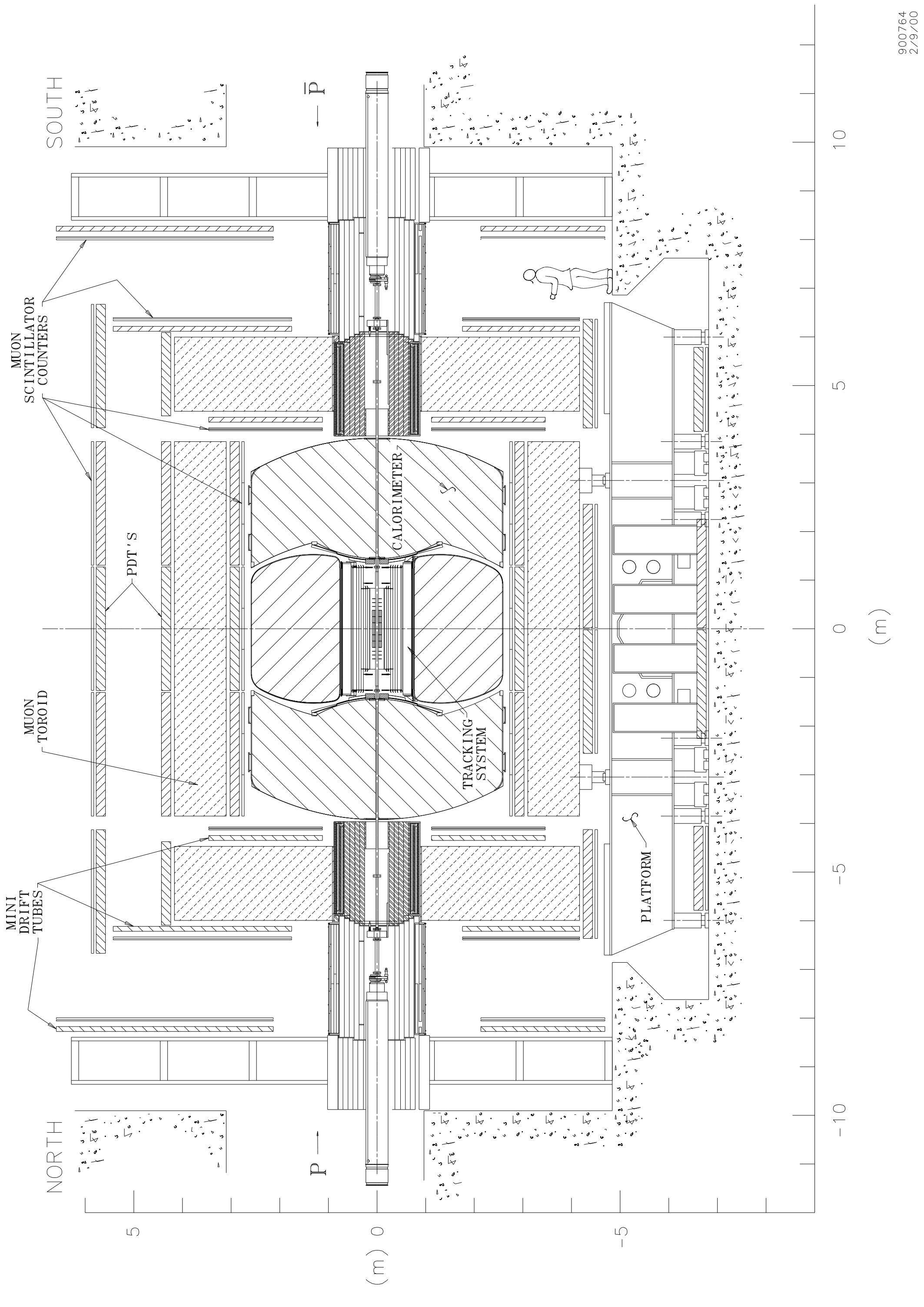

Figure 3.1: Side view through the DØ detector

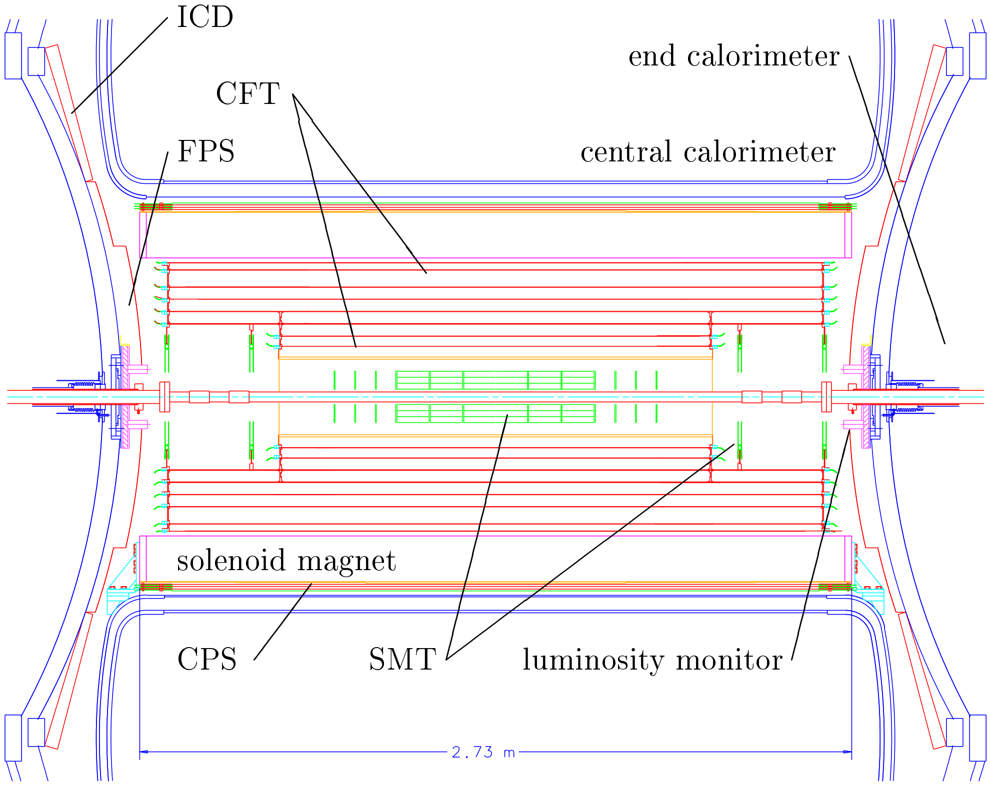

Figure 3.2: Cross-sectional view of the DØ tracking volume. This is a close up of the central section of the DØ detector shown in Fig. 3.1.

3.1 The Luminosity Monitor

Two luminosity monitors in Fig. 3.2 are used to measure the integrated luminosity. When a proton and antiproton collide inelastically, a shower of particles is produced in both directions along the beam axis, and the luminosity monitors can detect them. The luminosity monitors surround the beampipe at z $\approx \pm 1.35$ m from the center of the detector. The monitors are made of wedges of scintillator with a photomultiplier tube attached to each wedge, as shown in Fig. 3.3.

This detector is used to count the number of interactions occurring at D0. Using a calculation of the total inelastic $p\overline{p}$ cross section [28], the instantaneous luminosity can be measured using this detector. The luminosity monitor is also used to identify diffractive events with forward rapidity gaps.

3.2 The Solenoid Magnet

One of the biggest changes to the DØ detector between Run I and Run II was the addition of a superconducting solenoid magnet inside the calorimeter's bore (see Fig. 3.2). The magnet was designed to present only a small amount of material to particles emerging from the point of interaction. This minimizes conversion of photons into e^+e^- pairs and multiple Coulomb scattering. The coil is 2.75 m

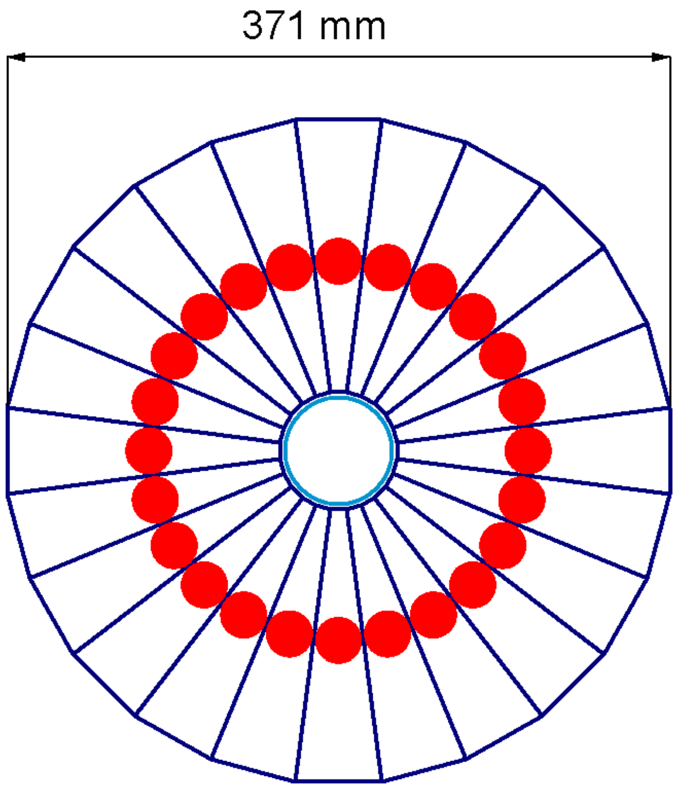

Figure 3.3: Geometry of one of the luminosity monitors, with the beampipe running down the center. The filled circles show the positions of the photomultiplier tubes.

long and 0.32 m thick, which corresponds to 0.188 absorption lengths (λ_0) and 0.88 radiation lengths (X_0) of material at normal incidence. The magnet has been operating reliably for several years at 2 T. For more information on this device, see Refs. [32] and [33].

3.3 The Silicon Microstrip Tracker

When a charged particle from a $p\overline{p}$ collision exits the beampipe, the first detector it encounters is the Silicon Microstrip Tracker (SMT). Silicon detectors are very popular in high energy physics because of their excellent position resolution. The SMT is shown at the center of Fig. 3.2. Figure 3.4 gives an overview of the SMT.

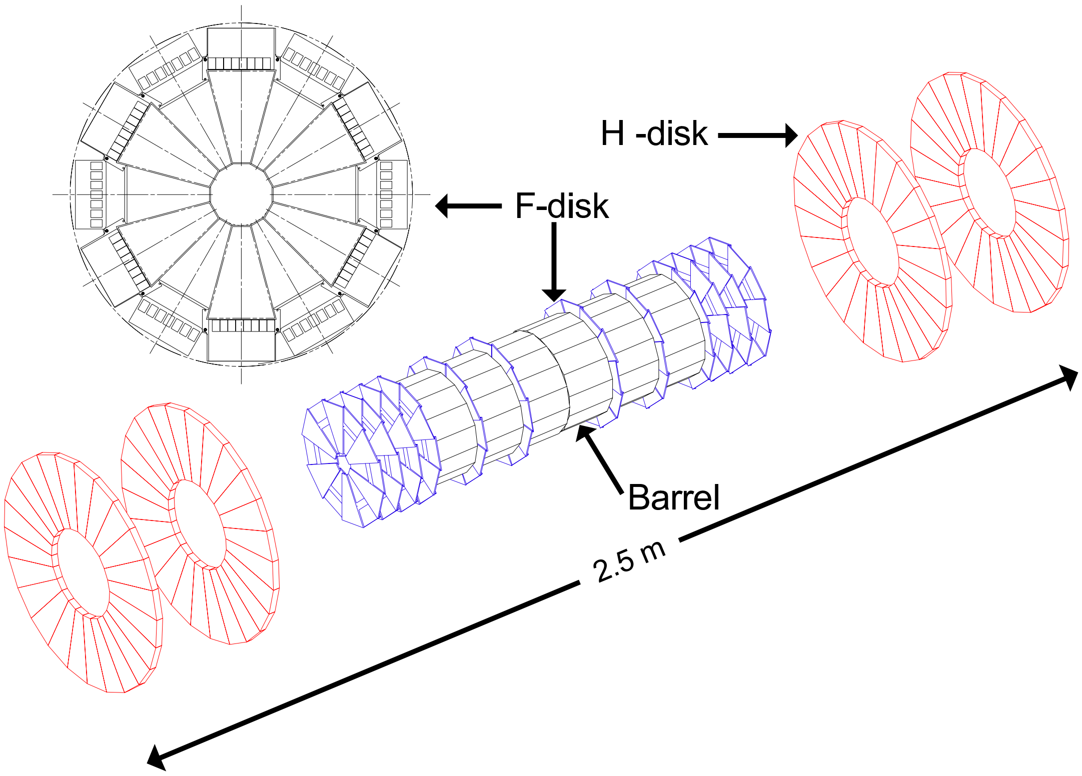

Figure 3.4: Schematic of the SMT

In total, there are more than 800,000 channels in the SMT. These channels are positioned in barrels at small pseudorapidity and in disks at forward pseudorapidities. The detectors collect the electron/hole pairs produced by charged particles passing through the silicon wafer. To collect the flow of electrons, a voltage of $\approx$100 V is put across the wafer. The charge is collected on parallel strips that have a pitch ranging from 50 to 153.5 μm. By measuring the amount of charge deposited on each strip, a hit-position resolution of $\approx$10 μm can be achieved [34].

3.4 The Central Fiber Tracker

Following the SMT, a particle with small pseudorapidity encounters the Central Fiber Tracker (CFT). The active elements of the CFT are 77,000 scintillating fibers. Each one is 0.835 mm in diameter and is mirrored on one end. The precisely placed scintillating fiber is connected at the end opposite the mirroring to a clear fiber-optic waveguide that channels the light signal to "visible light photon counter" (VLPC) chips that detect the small amounts of visible light [35].

The fibers are placed around the beampipe on eight concentric carbon-fiber support cylinders. These cylinders are labeled in Fig 3.2. One layer of fibers is glued directly to each cylinder, with the fibers parallel to the beampipe, these are called the axial layers. Stereo fibers with an angle of 3° relative to the axial fibers are glued on top of them. These stereo layers alternate between being left-handed and right-handed helices, and are called U and V layers. In total, the tracker has eight axial layers, four U layers, and four V layers. When a particle passes through a layer, depending on its path, it can pass through one or two fibers. For ease of manufacturing, the fibers were made into ribbons of 256 fibers before being attached to the cylinders. Figure 3.5 shows several fibers from a single layer of the CFT.

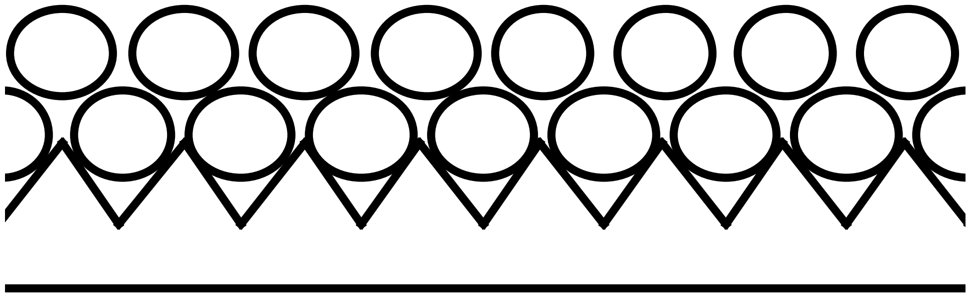

Figure 3.5: The cross section of a segment of a single layer of the CFT. The saw-toothed block is the curved connector located at the end of the cylinder.

The VLPC chips operate at 9 K and are housed in cassettes of 1024 channels. This technology was chosen because the typical signal to reach the VLPC consists of ≈10 visible photons, which is difficult to detect with most technology but is easy for VLPCs. Figure 3.6 shows the output spectrum from a VLPC channel with an average of about one detected photon, this is approximately one tenth of our typical signal.

For the measurement of the inclusive jet cross section, the tracking detectors

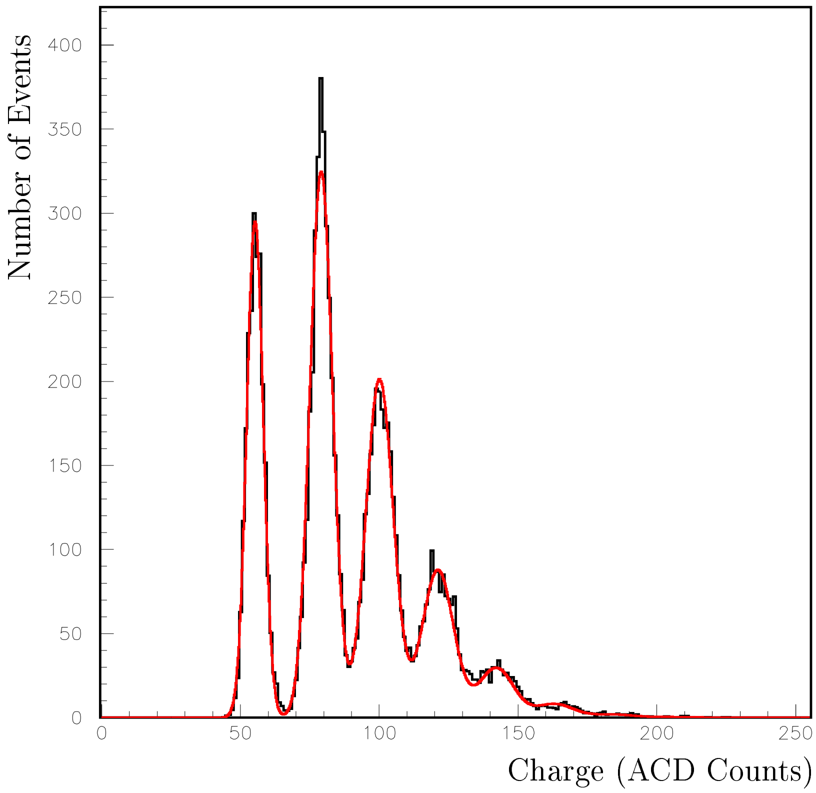

Figure 3.6: The output spectrum from a VLPC channel with a small amount of light incident on the detector element. The first peak corresponds to the pedestal (no photoelectrons), the second peak is one photoelectron and so on. The fit corresponds to a model based on a Poisson-distributed number of photoelectrons and a single parameter for the widths of the peaks.

are used only to find the position of the event's primary interaction vertex.

3.5 The Central Preshower Detector

The central preshower (CPS) detector is located outside the solenoid, and is used primarily to complement the central calorimeter. In Run I, the DØ calorimeter had excellent energy resolution. The Run II design placed the solenoid in front of the calorimeter, which added material and degraded its energy resolution. The preshower detector was designed to recover the energy resolution by sampling particle showers directly downstream of the solenoid. The CPS has a 6 mm lead absorber in front of it to increase the showering of electrons and photons. The initiation of a narrow electromagnetic shower in the lead improves the spatial resolution of the detector for electrons and photons.

The CPS is made of three layers of scintillating strips with triangular cross sections, as illustrated in Fig. 3.7. The strips in the first layer are arranged to run parallel to the beampipe (axial) and the other two layers are U and V stereo at an angle of 23° with respect to the axial strips. Each strip of scintillator has a hole in the center, which is occupied by a wavelength-shifting fiber that directs the light to clear waveguides. These transport the light to VLPC cassettes, just like those in the CFT. To increase the dynamic range, the gain on the electronics is much lower than for the CFT. This provides a measure of the energy deposited by showers, but compromises detection of single particles.

3.6 The Forward Preshower Detector

The design of the Forward Preshower detector, or FPS, is similar to that of the CPS, with the same elements ranging from triangular scintillating strips to VLPC cassettes. The primary difference is that the FPS is in two pieces, each

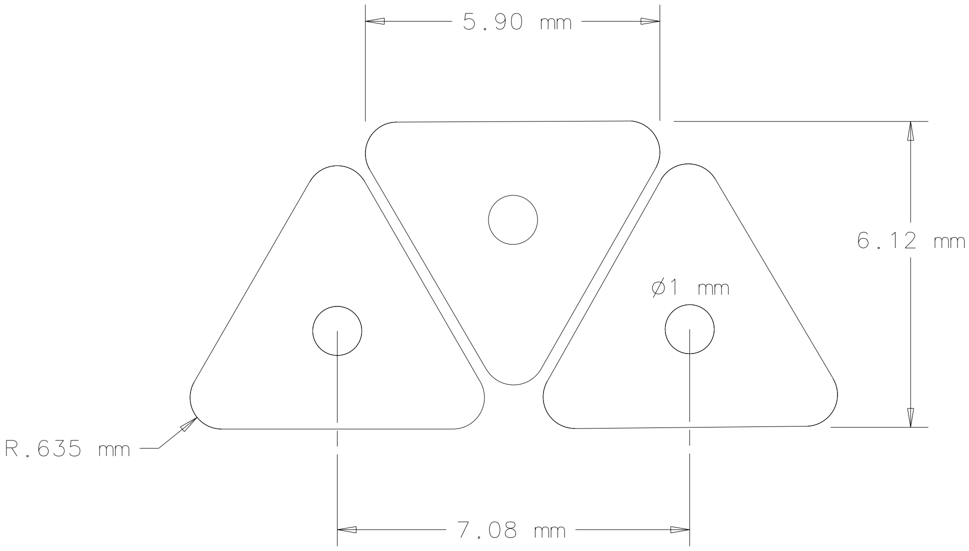

Figure 3.7: The cross section of a layer of the central preshower detector. The triangles are made of extruded plastic scintillator and the circles in the middle of each represent holes that are occupied by wavelength shifting fibers. Each triangular scintillator strip is wrapped in reflective material to increase light yield and reduce cross talk.

mounted on the end calorimeters at the positions shown in Fig. 3.2. There are four layers in the FPS, inner U and V and outer U and V; there are no axial layers. There is an 11 mm lead absorber plate between the inner and outer layers. The inner layers usually detect minimally-ionizing particles, or MIPS, while the outer layers can detect the beginning of showers, which generate much larger signals. Because of this, the layers are often referred to as the MIP and shower layers. The gains on the MIP layer channels are set to detect small signals (similar to the CFT), while the shower layer channels have lower gain (similar to the CPS) to measure showers.

The solenoid does not shadow the forward calorimeters from the interaction region at the center of the detector. The function of the FPS is therefore not to improve energy resolution as in the case of the CPS; rather, its primary purpose is to discriminate between photons and electrons, which is difficult to do with only the calorimeter. If a particle is not observed in the MIP layer, but has a shower in the outer layer, it is likely to be a photon that did not interact in front of the lead. If there is a signal in the MIP layer and a shower in the shower layer, then the incident particle is likely to be an electron.[1]

3.7 The Calorimeter

The calorimeter system is critical to the analysis in this dissertation; its purpose is to measure the energy of particles that enter it. The locations of the calorimeters are displayed in Fig. 3.1, and details are illustrated in Figs. 3.8 and 3.9. Figure 3.10 shows the reconstructed energies (lego plot) in a typical interaction observed in the calorimeter. The calorimeter system is housed in three large cryostats, one central and two forward. The central calorimeter (CC) weighs $\approx$330 tons, and each of the two end calorimeters (EC) weigh $\approx$240 tons.

A typical cell in the calorimeter consists of a metallic absorber plate, followed

[1] A charged pion can have a signature similar to an electron in the FPS, but it generally has very different showering properties in the calorimeter, where photons and electrons have very similar signatures.

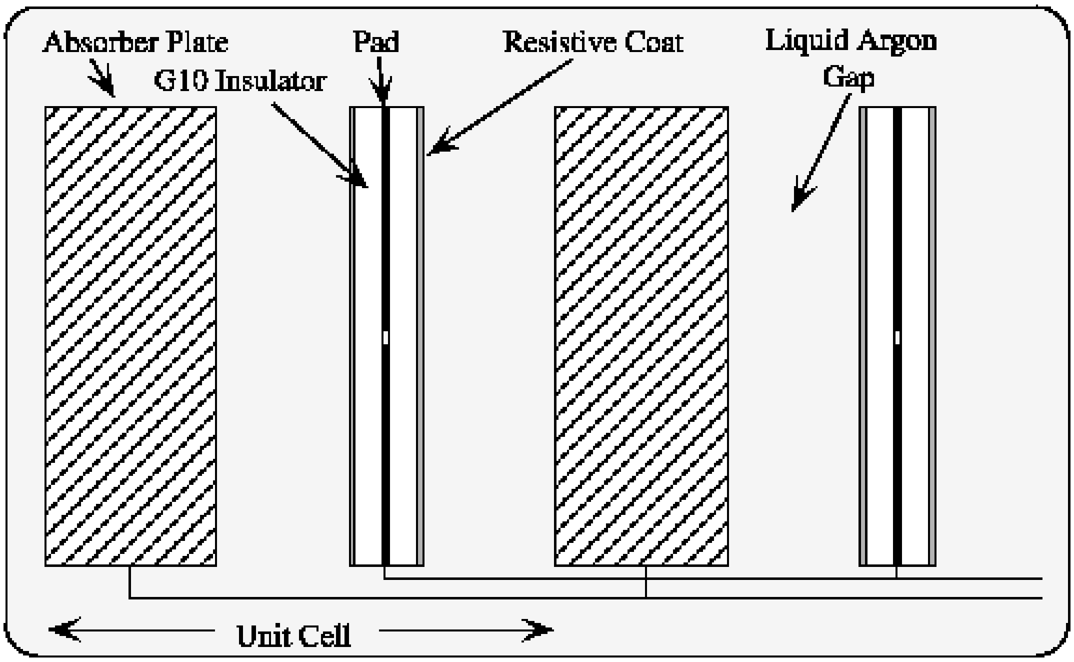

Figure 3.8: Schematic of two calorimeter cells.

by a gap filled with liquid argon. In the center of the gap is a G-10 board. When a particle enters the calorimeter, it showers inside the absorber plate and the particles from the shower ionize the argon atoms. The ionization electrons are attracted to copper pads on the G-10 boards which have a thin resistive coating, and are held at high positive voltage. The drifting electrons create an image charge on both sides of the copper pads, which is read out at the edges of the board via copper channels. The gap between absorber plates is 2.3 mm and the electron drift time across the gap is ≈450 ns. Figure 3.8 shows a schematic of two typical calorimeter unit cells. Several unit cells are stacked on top of each other to create a layer in the calorimeter. All of the cells in the layer are read out together to get the energy deposited in that layer, constituting a "readout cell." In other chapters of this dissertation, calorimeter cell always means readout cells not unit cells.

The central calorimeter spans a pseudorapidity of about ± 0.8. The four innermost layers are called the electromagnetic (EM) layers. The third layer is where the maximum number of particles in an electromagnetic shower is expected to occur, and the cells there are 0.05×0.05 in $(\eta,\ \phi)$ space; the other layers have 0.1×0.1 cells. As mentioned before, the cells are arranged in a projective geometry relative to the nominal center of the detector. Plates of ^{238}U (3 mm thick in the EC and 4 mm in the CC) are used as absorber material in the EM cells, and the EM layers are read out in groups of 2.0, 2.0, 6.8, and 9.8 radiation lengths (X_0) (for particles entering at normal incidence).

The next three layers of the CC are the fine hadronic layers. These also have uranium absorbers that are 6 mm thick. The separate layers are 1.3, 1.0, and 0.9 nuclear interaction lengths (λ) deep. The final layer, called the coarse hadronic layer, has 46.5 mm thick copper absorbers that are that total 3.2 λ deep.

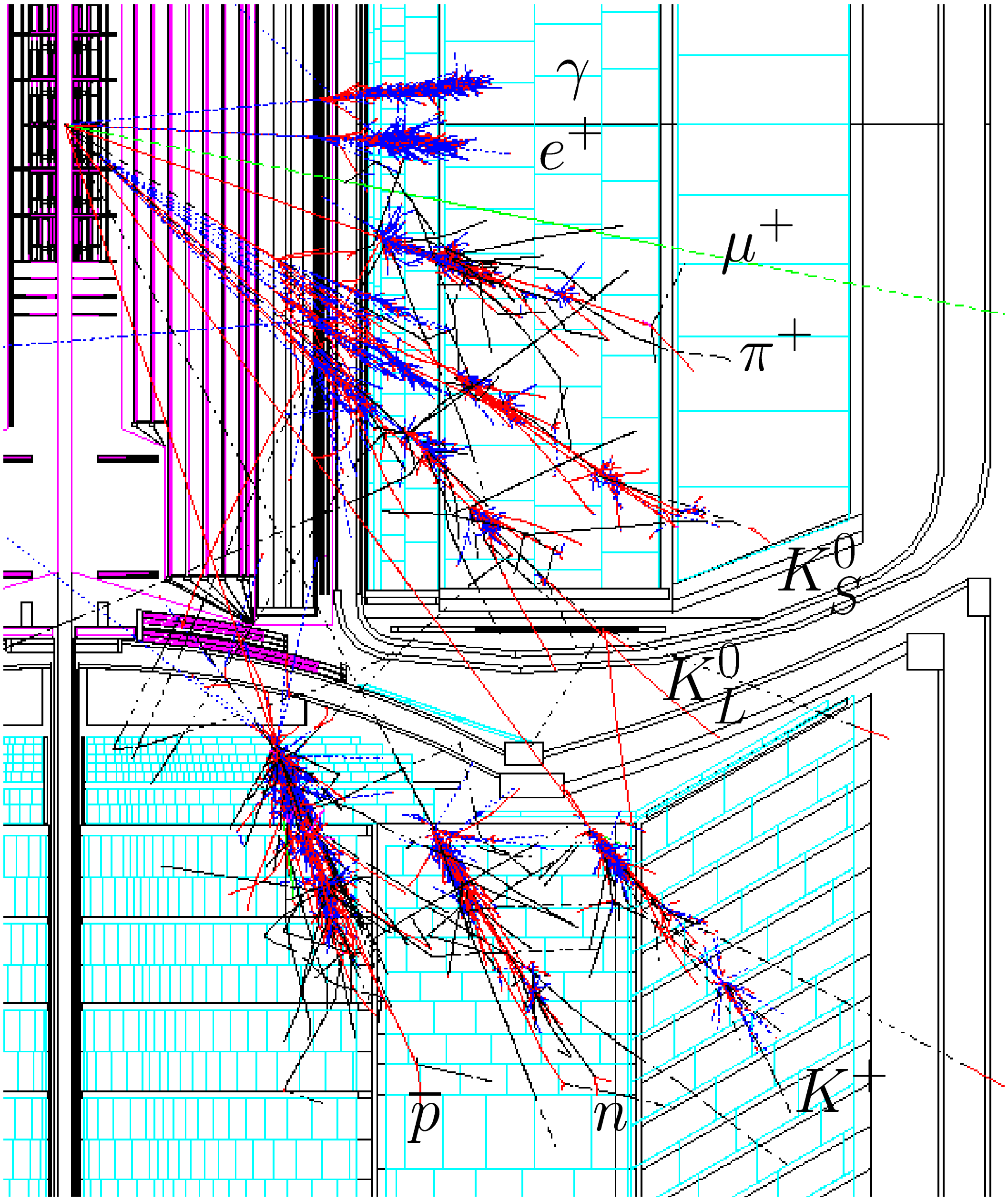

Figure 3.9: A cross sectional view of a portion of the DØ calorimeter with overlaid simulated showers. Each object has a transverse momentum of 50 GeV/c. The beampipe is the vertical open channel at the left edge of the image.

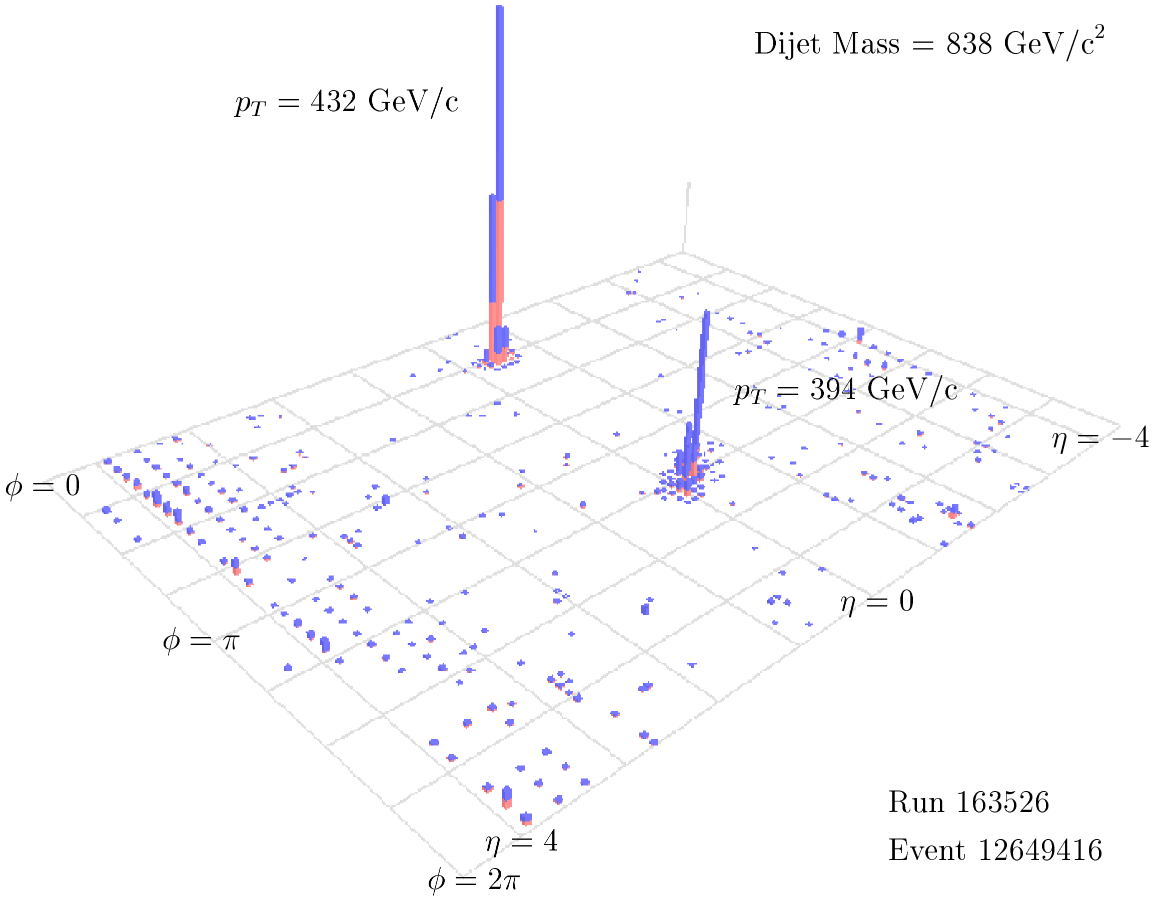

Figure 3.10: A "lego plot" of a typical two jet event. This plot shows the quantity and location of energy deposited in the calorimeter towers. Each upward pointing prism represents a tower, with its height proportional to the deposited transverse energy. The transverse momentum of the jets was calculated using ILCA with $R = 0.7$.

The readout cells in each layer line up with readout cells in the layers in front and behind them, creating projective towers with each readout cell in the tower having the same value of ϕ and η_d. Detector eta (η_d) is η calculated from the center of the detector. The summed energy in a tower is used instead of the readout cells for many of the measurements made with the calorimeter, and the transverse energy of a readout cell or tower, defined as $E_T \equiv E\ \sin(\theta)$, is often the most important measurement.

Each end calorimeter is similar to the CC, but with somewhat different layers and materials. Between the CC and EC, are the inter cryostat detectors (ICD) and the "massless gap" detectors. These compensate for the uninstrumented regions between the cryostats, but do not have the fine energy resolution of the main calorimeter. The ICD consists of slabs of scintillator, read out with photomultiplier tubes located in the space between the cryostats. The massless gap detectors are inside the cryostats and are extra readout pads that sample the shower as it develops between the CC and the EC. The inter cryostat region ranges from $0.8 \lesssim |\eta_d| \lesssim 1.4$, and the EC covers particles emitted further forward ($1.4 \lesssim |\eta_d| \lesssim 4.0$).

All of the detectors at DØ have "zero-suppression" thresholds to keep the event size and readout times at reasonable levels. In most, this is just a cutoff value for each channel, where the result is not recorded unless the signal is larger than a specified value. The calorimeter is different. Calibration runs are performed that measure an ADC energy spectrum for each channel when there is no signal, and these distributions have been shown to be Gaussian in character [36]. A channel's value is recorded in an event if it is some number of standard deviations above or below the mean value. By reading out the negative values, positive and negative fluctuations that are just above threshold cancel on average.

The calorimeter is the only detector that is physically the same as in Run I, and so Ref. [30] is therefore still appropriate for its description. The electronics that are used to read out the signals, however, have changed significantly in order to take data at 396 ns bunch spacing.

3.8 Muon System

DØ has a large muon system outside of the calorimeter [31]. It uses wire chambers for precision tracking and scintillators with photomultiplier tube readouts that are used for fast triggering. Since the muon system is not used in this analysis, we will not elaborate on it any further.

3.9 Triggering

The Tevatron provides DØ with 36 bunch crossings every 21 μs or 1.7×10^6 crossings per second.[2] The average event written to tape contains ≈300 kilobytes of data, recording the information at every crossing would therefore yield more than 500 gigabytes of data per second. This is well beyond anything DØ could hope to record or analyze. Selective triggering is used therefore to choose the events of greatest interest.

The triggering systems reduce the rate to tape to about 50 events per second. There are three levels of triggering, and each takes progressively more time to sort through the remaining candidate events and reduce the acceptance rate. The first level (L1) reduces the rate to ≈1400 Hz, and L2 reduces it further to ≈800 Hz. L3 is the last step that takes the rate to ≈50 Hz. DØ has numerous triggers to select many different types of events. In this section, we will focus on the jet triggers that are used for collecting events used in this particular analysis.

A trigger corresponds to a list of requirements at each level. In certain triggers, one or more levels have no requirement. Every event that is written to tape includes a list of the triggers that fired. Each trigger has a name that reflects its requirements, for example, "JT_45TT" selects events with at

[2] These crossings are not uniformly distributed in time (see Section 1.1.1).

least one jet candidate with a transverse momentum in excess of 45 GeV/c, "EM_MX" selects events with high energy photons or electrons (EM objects), and "zero_bias" selects events with no requirement other than being in time with a beam crossing. If an event passes an L1 requirement, then that trigger's L2 requirements are checked, and similarly for L3. If an event passes L1 because it meets the requirements for something other than a jet trigger, then it will not be checked for jets at levels two or three.

Some triggers are prescaled. If a trigger has a prescale value of 5, then only one randomly-selected event in five that passes that trigger is written to tape. This is accomplished by considering only one out of every five events for that trigger at L1; in essence, that trigger gets only one fifth of the luminosity that an unprescaled trigger gets. Triggers that fire only on rare events are not prescaled (have prescale values of 1), but triggers that fire often must be prescaled. Prescales are changed frequently, depending on the instantaneous luminosity. When the instantaneous luminosity is low, there are fewer rare events, and so the prescales on more common events can be reduced to keep the rate of events recorded on tape at $\approx$50 Hz. Doing this allows us to never miss rare events, and make the best use of the time when the Tevatron is providing low instantaneous luminosity.

The zero_bias trigger is satisfied at every bunch crossing. This trigger is used primarily to study the detector and has an enormous prescale factor to keep its rate to ≈0.5 Hz. The minimum_bias trigger is similar to zero_bias, but it also requires hits in the luminosity monitors. It too is usually greatly prescaled to achieve a rate of ≈0.5 Hz to tape.

The specific triggers that were used for measuring the inclusive jet cross section are JT_95TT, JT_65TT, JT_45TT, and JT_25TT_NG. The "JT" part of their names refers to jets. "TT" means that they are triggered with trigger towers at L1 (described below). The number is the transverse energy in GeV required at L3 to fire the trigger. The "NG" in JT_25TT_NG means "no gap," to distinguish it from other 25 GeV jet triggers that require rapidity gaps for studying diffractive physics.

3.9.1 Level 1

The Level 1 trigger provides the biggest reduction in rate. At every beam crossing when the detector is ready to record data, the L1 trigger analyzes the event to determine whether it should be accepted. Only four detectors are used at L1: the CFT, the muon system, the calorimeter, and the luminosity monitors. Because the response must be fast, the algorithms applied must be especially designed for high speed. L1 accepts events that are of great interest, at the price of keeping many events that are not so interesting.

The calorimeter portion of L1 uses information from trigger towers in the calorimeter. Each such trigger tower is formed from four standard towers, grouped together into non-overlapping 0.2×0.2 areas in $(\eta,\ \phi)$ space. In the fast readout, the energy for each trigger tower is summed to a total energy that has a least count value of 0.5 GeV. An example of a typical trigger requirement is (2, 5). This requirement will be met if two trigger towers detect more than 5 GeV of transverse energy. The distance between those towers is not considered in the algorithm, and so the signals can arise from a single jet or from different jets. The signals can even correspond to electron showers. Because these towers are much smaller in $(\eta,\ \phi)$ than the jets we want to study, it is thought that these multi-tower triggers are reasonable vehicles for triggering on jets with high transverse momentum.

When an L1 "accept" is issued, the entire detector is read out. While this is happening, the detector cannot respond, giving rise to "dead time," during which another event cannot be considered. The fraction of dead time during a good run is usually kept under $\approx$10%.

3.9.2 Level 2

The L2 system operates on computers called "alpha boards." These are mounted on single boards within VME crates and use the Linux operating system. Each of these boards runs a single algorithm that uses data read out at L1. One of these analyzes calorimeter data in search of both jets and EM objects, another analyzes the central muon data, and a third the forward muon data. Two more run tracking algorithms for CFT data and a subset of SMT data. These boards transmit their results to a global alpha board that is used to decide whether the information warrants an accept at L2.

The L2 system for the calorimeter, uses the same fast readout information as L1. The difference is that it uses a more sophisticated algorithm for identifying jets. This algorithm clusters trigger towers into five by five groups centered on the towers with highest p_T. If any of these pseudo jets is above the trigger's L2 threshold, the event is accepted. Certain jet triggers have no L2 requirement, so if an event satisfies the L1 requirements it will automatically pass L2.

3.9.3 Level 3

If an event is accepted at L2, then all of the collected information, including the slow precision readout, is passed for analysis to a node of the L3 computer "farm". The L3 node then partially reconstructs the event to determine whether it meets the criteria for acceptance.

If an event passes the L1 and L2 components of a jet trigger, the L3 node then runs the "simple cone" clustering algorithm on the calorimeter data. This uses the slower full precision readout of the calorimeter, but because of time constraints, does not perform a full jet reconstruction. For example, full reconstruction provides the position of the collision vertex, which can be more than 0.5 m from the center of the detector along the z axis. At L3, the event vertex is assumed to be at z=0. The simple cone algorithm is not as sophisticated as the Improved Legacy Cone Algorithm run offline (see Section 2.1.3). The primary difference between the algorithms is that the simple cone algorithm does not use midpoints, and it does not split or merge jets. Because there is no splitting and merging, L3 can decide that a given tower in the calorimeter contributes its full energy to multiple jets in the event. As long as the trigger requirements only relate to the highest p_T jet in the event, this does not pose a significant problem.

Most triggers have a specified Mark and Pass (M&P) rate at L3, where marked events are analyzed as usual, but recorded whether or not they meet the L3 requirements. Events recorded with the M&P designation provide a way to check the performance of L3. If the rate is set to 100 for a given trigger, then one out of each 100 events accepted at L2 by that trigger will be marked.

3.10 Offline Reconstruction

Once an event passes one or more triggers, it is written to tape and stored for subsequent use. DØ has a farm of 250 Linux computers that run the offline reconstruction program "reco" on every event in runs that are designated to be of high quality.

The first part of reconstructing an event involves the unpacking of information. At this stage, the data bits from all detector elements are interpreted to form clusters. These correspond to hits, such as energy in calorimeter towers or locations in the trackers where a particle was detected. During the unpacking, calibrations are applied to determine the energy in each calorimeter cell. The clusters are used to reconstruct physical objects such as jets, muon trajectories, electrons, etc, that form the basis of the following data analysis.

The tracking algorithm forms the clusters in the CFT and SMT into helices, corresponding to the trajectories of charged particles in a magnetic field [37]. Such "tracks" are then used to find all the interaction vertices and to select the primary one [38]. To choose the primary vertex, each possible vertex is assigned a figure of merit, F_{vertex}, that is defined as follows:

$$F_{vertex} \equiv \sum_j \log(p_{T\,j}) \tag{3.1}$$

where p_{Tj} is the transverse momentum of each track that intersects the others at that vertex. The vertex with the highest value for the figure of merit is selected as primary.

Once the primary vertex is identified, each calorimeter tower is assigned a four-vector momentum. That four-vector corresponds to a massless particle with the energy measured in the tower, and a three-momentum calculated from the angles defined by the primary vertex and the center of that tower. These four-vectors are clustered together using the Improved Legacy Cone Algorithm, as described in Section 2.1.3.

The unpacking and reconstruction is performed with the goal of maximizing efficiency at the expense of purity of signal in data. Anything that resembles a jet is therefore identified as such at this stage. The drawback is that some false jets due to, for example, electron or photon showers, calorimeter noise, or cosmic rays, are often included. The methods used to remove such backgrounds will be discussed in Section 5.2.

Chapter 4

Data Selection

The data used in this analysis are referred to as the "2003 Moriond Data Set." That is to say, the data was used for DØ approved results presented at the Spring 2003 conferences. After all selections, this dataset contains 34.3 pb^{-1} of data.

4.1 The Data

The data sample is comprised of runs starting with Run 162468 (August 22, 2002) and ending with Run 170361 (January 11, 2003). The starting date corresponds to the full commissioning of all the major detector systems.

Originally, parts of this data set was reconstructed using different versions of reconstruction code, but eventually all was reprocessed using only two versions of the offline code: p13.05.00 and p13.06.01. The p13 releases prior to p13.05.00 did not contain cell-by-cell corrections for converting calorimeter ADCs into energy. It was thought that such corrections might cancel out, but our analysis indicated that this was not the case. Fortunately, there was enough time available before the conferences for reprocessing all of the data with p13.05.00 or p13.06.01.

4.2 Good Runs

Once the range of runs was selected, it was clear that not every run in the range had data of acceptable quality. Some of the runs were recorded while the detector was temporarily compromised. The first check of run quality is performed by "shifters" in the control room who assess the quality while the data is being collected. If the shifters do not think the run reliable, the data is not used. Unfortunately, often there are problems that the shifters do not detect, and we must therefore apply some basic selection criteria to assure the overall quality of the data.

4.2.1 Run Size

The first requirement involves the size of any run. If a run does not contain at least fifty events that fired the JT_25TT_NG and JT_65TT triggers, it is dropped. This assures having enough events for checking other criteria. We do not use the JT_45TT trigger for selecting runs because it had a large prescale factor in some runs. The higher-p_T triggers are not considered at this step because their rates are so low.

4.2.2 Missing Transverse Energy: METC

The next criterion refers to the missing transverse momentum, or $\not{E}_T$. The variable we use is called METC. METC is an "uncorrected" $\not{E}_T$, calculated using just the event's primary vertex and the energies in the cells of the calorimeter. It is a vector in the (x, y) plane, defined as follows:

$$\overrightarrow{\mathrm{METC}} \equiv \sum_j E_{Tj}(\hat{\mathrm{x}} \cos\phi_j + \hat{\mathrm{y}} \sin\phi_j) \tag{4.1}$$

where j refers to every cell in the calorimeter that is above threshold. Along with the magnitude of METC, we also use the x and y components of METC. If the mean value of METC or either component in a run is far from the average value in all data, the entire run is removed. (For details, see Ref. [39].)

4.3 Triggers

As indicated previously, the events used in this analysis were collected using the jet triggers labeled JT_25TT_NG, JT_45TT, JT_65TT, or JT_95TT. These triggers fire when Level 3 finds at least one "jet" with more than 25, 45, 65, or 95 GeV of E_T, respectively. As a fine point, it should be re-emphasized that L3 uses a "simple cone" algorithm, and these jets are therefore more properly specified by E_T not p_T, and are fundamentally different than those reconstructed offline. The full criteria for each trigger are specified in Table 4.1. Since JT_95TT was not prescaled, the redundant trigger JT_125TT is not used in this analysis. In addition, trigger CJT5,[1] which does not have any L2 or L3 requirements, is used to monitor the turn-on for trigger JT_25TT_NG. Figure 4.1 shows the uncorrected inclusive differential cross section for jet production for $|\eta| < 0.5$ as a function of jet transverse momentum for the different triggers. This is just the number of jets divided by the integrated luminosity of the respective event sample. The data have not been corrected for inefficiencies nor for migrations of jets from bin to bin caused by resolution in jet transverse momentum. The transverse momentum in all plots is corrected for the jet energy scale (JES) (Chapter 6).

[1]CJT5 is a name coined prior to the implementation of L2 or L3 and refers to its L1 requirement (1, 5).

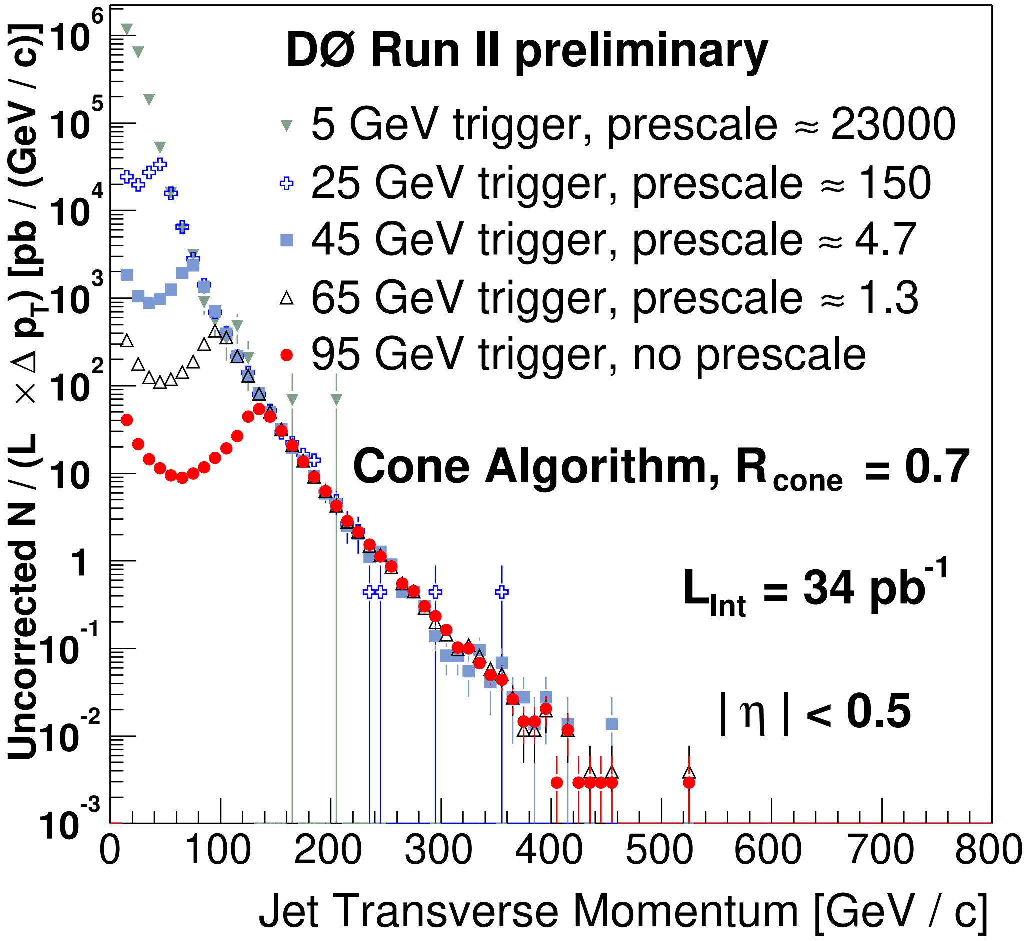

Figure 4.1: The uncorrected inclusive jet cross section for five triggers.

Trigger	Level 1 Requirement	Level 2 Requirement	Level 3 Requirement
CJT5	(1, 5)	-	-
JT_25TT_NG	(2, 5)	-	25
JT_45TT	(2, 5)	-	45
JT_65TT	(3, 5)	20	65
JT_95TT	(4, 5)	40	95

Table 4.1: Requirements for triggers used in this analysis. For more explanations, see Sec. 3.9.

We assume that each of our four triggers becomes fully efficient for events with a central jet of sufficiently high transverse momentum. For example, we expect that any event with a 400 GeV/c central jet will always fire the JT_25TT_NG trigger, as long as the prescale factor does not exclude it through random selection. To find the value at which any trigger becomes fully efficient, we plot the ratio of the uncorrected cross section for each trigger relative to that for the trigger of next-lower threshold. The trigger with the higher threshold is as efficient as the one with the lower threshold when the cross sections become the same. We assume that at this point, the efficiency of the higher trigger is greater than 99 percent. These efficiency points are given in Table 4.2, and the plots of ratios are shown in Fig. 4.2. The ratio for the JT_25TT_NG trigger looks peculiar, but this is because without a Level 3 requirement, the CJT5 trigger fires on events where the JT_25TT_NG does not.

For several reasons, the triggers do not turn on instantly. First, different jet algorithms are used online at L3 and offline. Second, the L3 trigger does not use the event's reconstructed vertex, but rather assumes it to be at the center of the detector. Third, the p_T used in the offline analysis is corrected for jet energy scale (see Chapter 6), while L3 is not.

The regions in which each trigger is used are all at higher transverse momenta than their thresholds (Table 4.2). This was done because the analysis is not limited by statistics near any of the transitions between triggers.

In forming the inclusive jet cross section, we use events from only one selected trigger in any bin of transverse momentum. Consequently, for example, the bin between 100 and 110 GeV is from the JT_45TT trigger. This ignores jets that might be in events fired by the JT_65TT or JT_95TT triggers. Except for prescaling, the JT_45TT trigger is fully efficient in that range, so using it alone causes no bias. Thus the trigger at the lower-p_T threshold is used exclusively until the higher-p_T trigger becomes fully efficient.

Trigger	Minimum Transverse Momentum GeV/c	Maximum Transverse Momentum GeV/c	Integrated Luminosity (pb^{-1})
JT_25TT_NG	60	100	0.227
JT_45TT	100	140	7.255
JT_65TT	140	180	25.626
JT_95TT	180	-	34.026

Table 4.2: The range of transverse momentum in which each trigger was used. There is a $\pm 10\%$ overall systematic uncertainty in the luminosities.

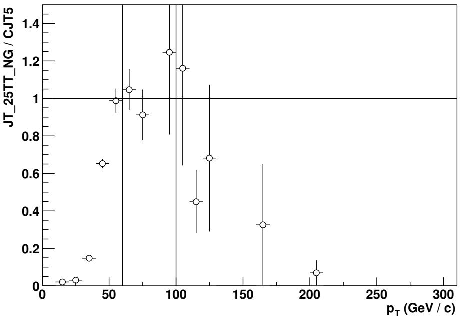

(a) JT_25TT_NG / CJT5

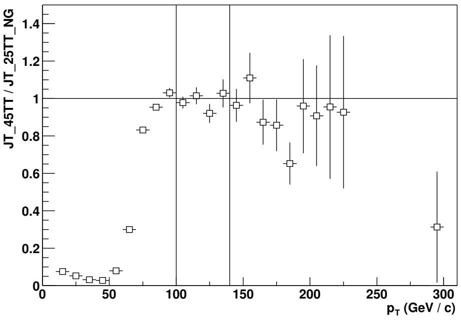

(b) JT_45TT / JT_25TT_NG

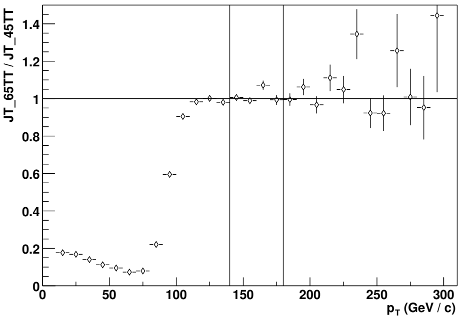

(c) JT_65TT / JT_45TT

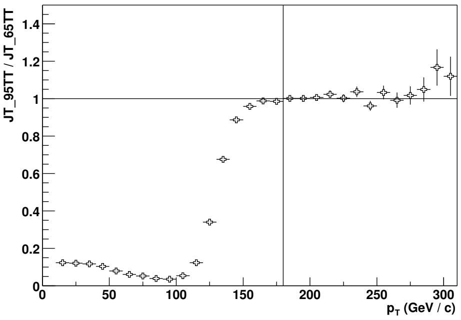

(d) JT_95TT / JT_65TT

Figure 4.2: Relative "turn-on" efficiency for triggers JT_25TT_NG, JT_45TT, JT_65TT and JT_95TT relative to their next lower triggers. These triggers are assumed to be fully efficient in the following regions: JT_25TT_NG ($p_T \geqslant 60\,\mathrm{GeV/c}$), JT_45TT ($p_T \geqslant 100\,\mathrm{GeV/c}$), JT_65TT ($p_T \geqslant 140\,\mathrm{GeV/c}$), and JT_95TT ($p_T \geqslant 180\,\mathrm{GeV/c}$). The vertical lines show the regions in which the data are used for obtaining our cross section; for the JT_95TT trigger, the region is everything to the right of the single vertical line.

Chapter 5

Data Quality

Every event must satisfy certain quality requirements before it is used in the measurement of the cross section. Furthermore, each jet in an event must also satisfy quality requirements before it is used. Such requirements remove certain jets, and after implementing the selection criteria, corrections are therefore required to obtain an unbiased cross section.

5.1 Event Selection Criteria

Two requirements are made on each event that satisfies any of our triggers. The first requirement is related to the primary vertex and the second to the $\not\!\!E_T$.

5.1.1 Vertex Requirements

Proper offline reconstruction of a jet's properties depends on a good measurement of the event's primary interaction vertex. Figure 5.1 displays the number of tracks (N_{Tracks}) pointing to the reconstructed primary vertex in events that fired the JT_95TT trigger. The distribution of the z-position of the event vertex (z_{vtx}) is displayed in Figs. 5.2, 5.3, and 5.4 for events with one, two, and three or more jets in the central region ($|\eta| < 0.5$) that satisfy all jet and event quality criteria, but without any requirement on jet transverse momentum, except for the implicit cutoff of $p_T > 8$ GeV/c used in the reconstruction software.

We require at least five tracks to point to the primary vertex, and a reconstructed z-position within 50 cm of the center of the detector. We assume that the jets in an event with a primary vertex that does not meet these requirements is poorly measured, and the efficiency of both vertex criteria is therefore defined by the ratio of events in the range $|\mathrm{z_{vtx}}| < 50$ cm, with $N_{Tracks} \geqslant 5$ to the whole range of $\mathrm{z_{vtx}}$ values, without separate regard to the requirement on N_{Tracks}. The peak in Fig. 5.1 suggests that events where the vertex has too few tracks are different and we assume that this is mis-measurement. The efficiency is determined separately for each specific trigger, and for event samples with one, two, and more than two jets in the central region. The results are given in Table 5.1.

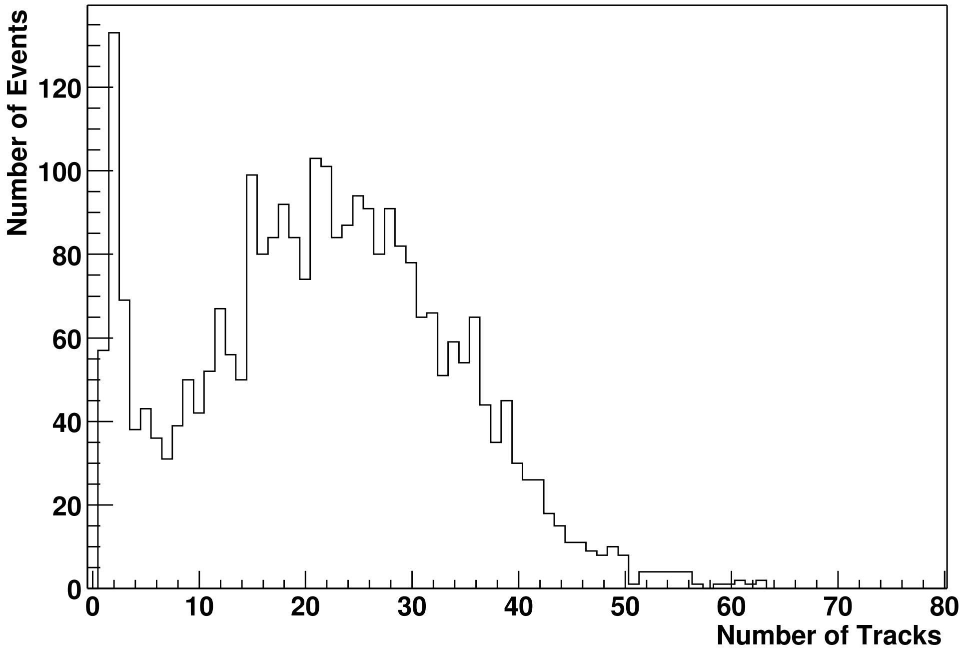

Figure 5.1: Histogram of the number of tracks used in the reconstruction of the primary vertex for events that passed the JT_95TT trigger and the $\not{E}_T$ requirements described below.

To check the impact of the vertex position requirement, we compared the result of the analysis for $|z_{vtx}| < 50$ cm with the criterion $|z_{vtx}| < 40$ cm and $|z_{vtx}| < 60$ cm. The results of this variation are shown in Fig. 5.5. There is indeed a small shift in the cross section, and we therefore include a systematic uncertainty in our measurement that varies between 0.5% and 2.5%, from 60 to 560 GeV/c in transverse momentum to account for this difference.

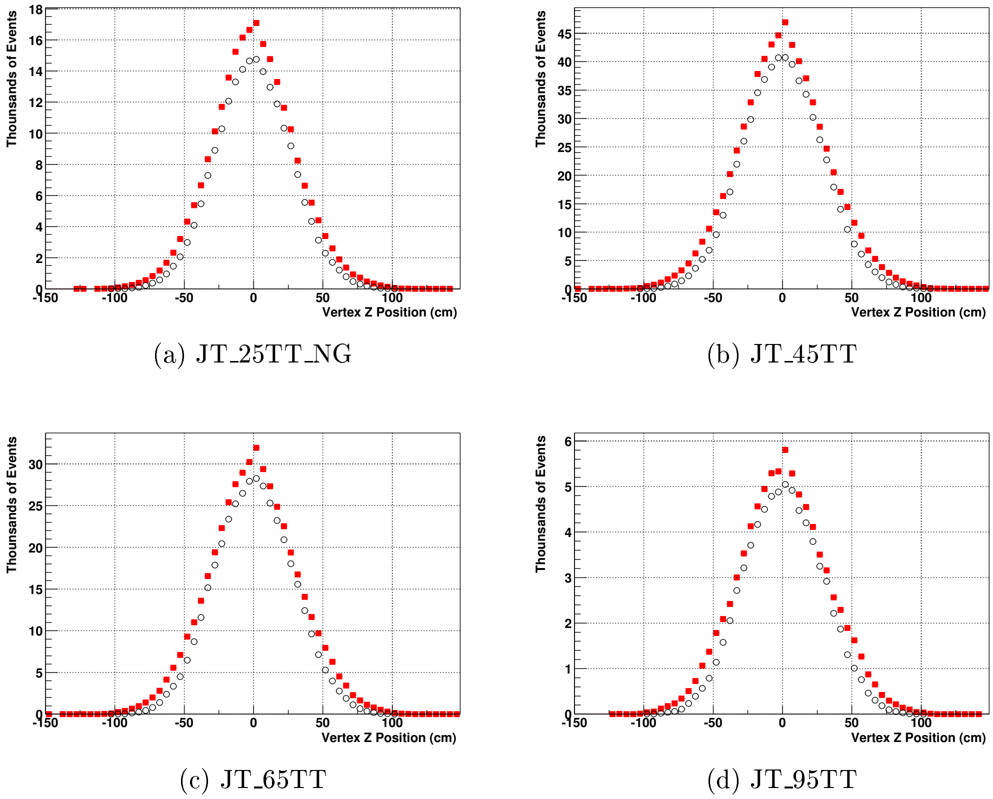

(a) JT_25TT_NG

(b) JT_45TT

(c) JT_65TT

(d) JT_95TT

Figure 5.2: Distributions of the reconstructed z position of interaction locations for events with one jet in the central region ($|\eta| < 0.5$) that satisfied all jet quality criteria. The distributions are shown for each trigger, before (squares) and after (circles) requiring $N_{Tracks} \geqslant 5$. An additional selection of $|z_{vtx}| < 50$ cm is applied subsequently.

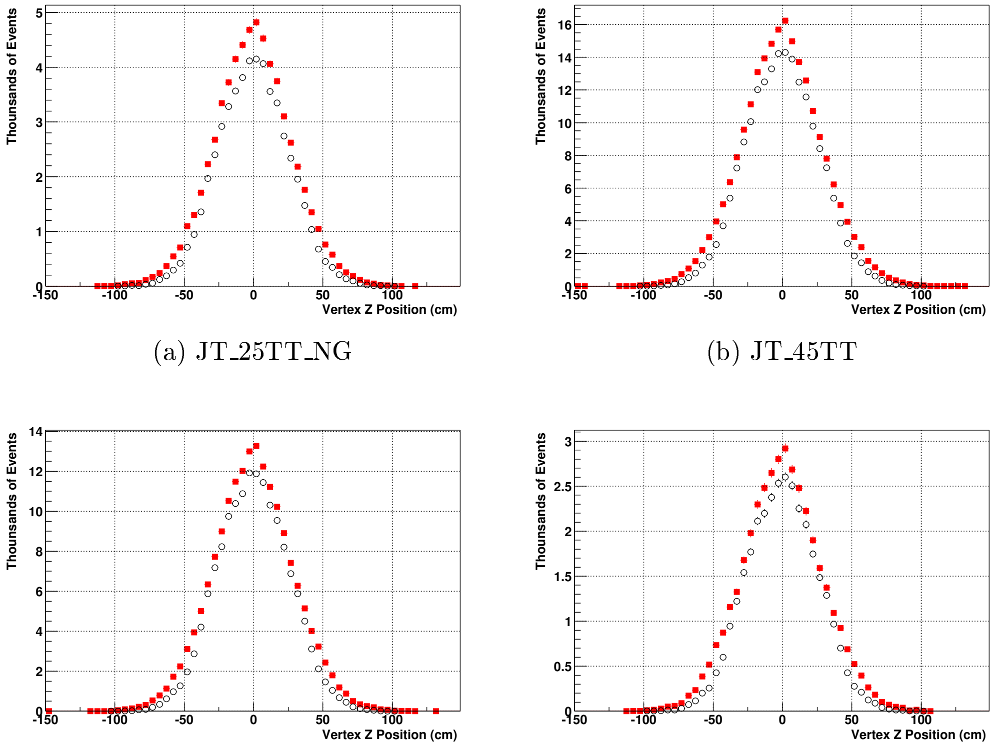

(a) JT_25TT_NG

(b) JT_45TT

(c) JT_65TT

(d) JT_95TT

Figure 5.3: Distributions of the reconstructed z position of interaction locations for events with two jets in the central region ($|\eta| < 0.5$) that satisfied all jet quality criteria. The distributions are shown for each trigger, before (squares) and after (circles) requiring $N_{Tracks} \geqslant 5$. An additional selection of $|z_{vtx}| < 50$ cm is applied subsequently.

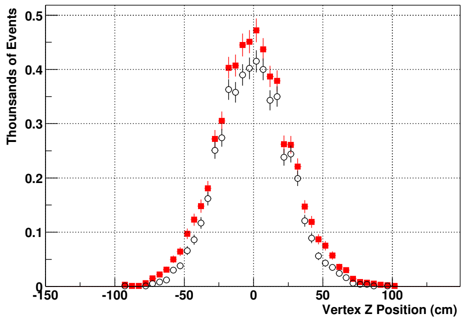

(a) JT_25TT_NG

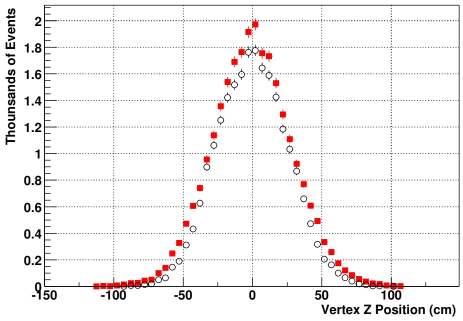

(b) JT_45TT

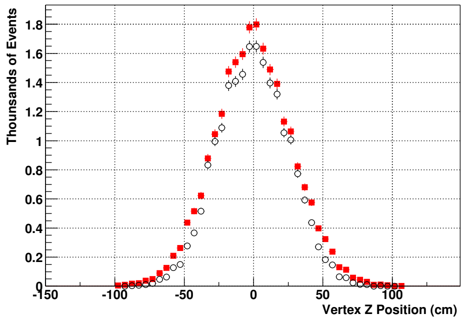

(c) JT_65TT

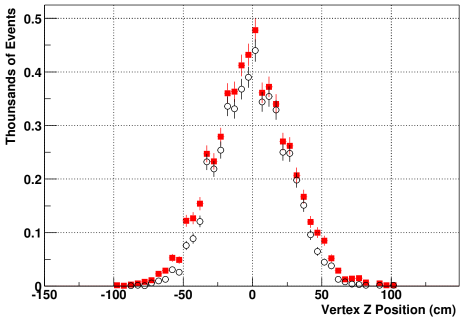

(d) JT_95TT

Figure 5.4: Distributions of the reconstructed z position of interaction locations for events with three or more jets in the central region ($|\eta| < 0.5$) that satisfied all jet quality criteria. The distributions are shown for each trigger, before (squares) and after (circles) requiring $N_{Tracks} \geqslant 5$. An additional selection of $|z_{vtx}| < 50$ cm is applied subsequently.

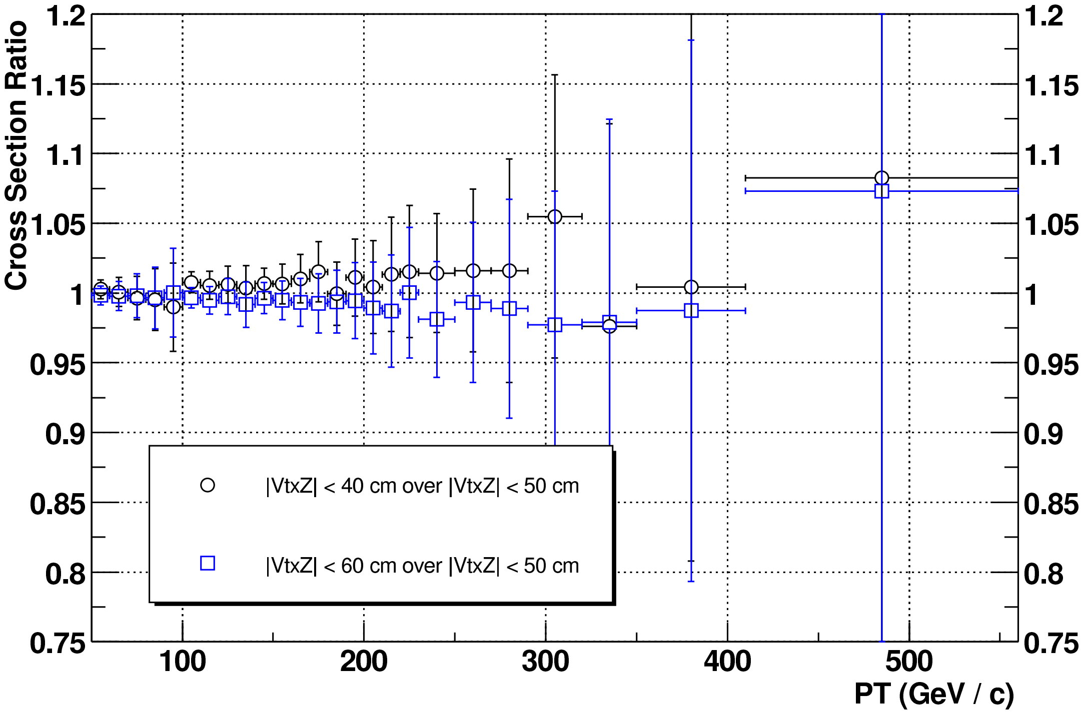

Figure 5.5: Dependence of cross section when the vertex requirement is varied. Shown is the ratio of the corrected cross section using different ranges of z_{vtx} to the cross section for the default value of $|z_{vtx}| < 50$ cm.

Trigger	Number of Central Jets: 1	2	$\geqslant 3$
	Fraction of events kept in sample		
JT_25TT_NG	0.7826 ± 0.0009	0.7975 ± 0.0016	0.8164 ± 0.0050
JT_45TT	0.7834 ± 0.0005	0.8089 ± 0.0008	0.8266 ± 0.0024
JT_65TT	0.7961 ± 0.0006	0.8214 ± 0.0009	0.8393 ± 0.0024
JT_95TT	0.7820 ± 0.0014	0.8133 ± 0.0020	0.8411 ± 0.0048

Table 5.1: Acceptance for events with different triggers and different number of central jets.

p_T range (GeV/c)	Relative Systematic Uncertainty on Cross Section
60 – 70	0.0052
70 – 80	0.0056
80 – 90	0.0060
90 – 100	0.0064
100 – 110	0.0068
110 – 120	0.0072
120 – 130	0.0076
130 – 140	0.0080
140 – 150	0.0084
150 – 160	0.0088
160 – 170	0.0092
170 – 180	0.0096
180 – 190	0.0100
190 – 200	0.0104
200 – 210	0.0108
210 – 220	0.0112
220 – 230	0.0116
230 – 250	0.0122
250 – 270	0.0130
270 – 290	0.0138
290 – 320	0.0148
320 – 350	0.0160
350 – 410	0.0178
410 – 560	0.0220

Table 5.2: Systematic uncertainty on the cross section from the requirement of $|z_{vtx}| < 50$ cm.

5.1.2 Missing Transverse Energy

The other criterion we used to evaluate event quality is based on the $\not\!\!E_T$ in the event. Momentum conservation requires that the sum of the vector transverse momenta of all particles must be zero in each event. However, some events contain large-momentum particles that are difficult to measure precisely (e.g., highly energetic muons), or that escape detection (e.g., neutrinos). In these events, conservation of transverse momentum will seem to be grossly violated. In our jet sample, events containing such high momentum particles should be quite rare, and their impact on our measurement negligible. However, the number of events where a cosmic ray particle deposits energy in the detector, or the detector malfunctions causing a large $\not\!\!E_T$ is not negligible. Of course, in addition, fluctuations in the development of hadronic showers and the energy resolution can also induce large $\not\!\!E_T$.

The criterion used for accepting an event requires

$$\mathrm{METC} < 0.7\ p_T[0] \tag{5.1}$$

where METC is the same $\not\!\!E_T$ variable defined in Sec. 4.2.2, and $p_T[0]$ is the uncorrected p_T of the event's leading jet. The leading jet is used in this criterion, even if that jet fails other quality criteria or is outside of our pseudorapidity range. We do not use JES corrected jet p_T because METC is also not corrected for the jet energy scale. Figure 5.6 shows the METC spectrum for all events that passed the JT_95TT trigger.

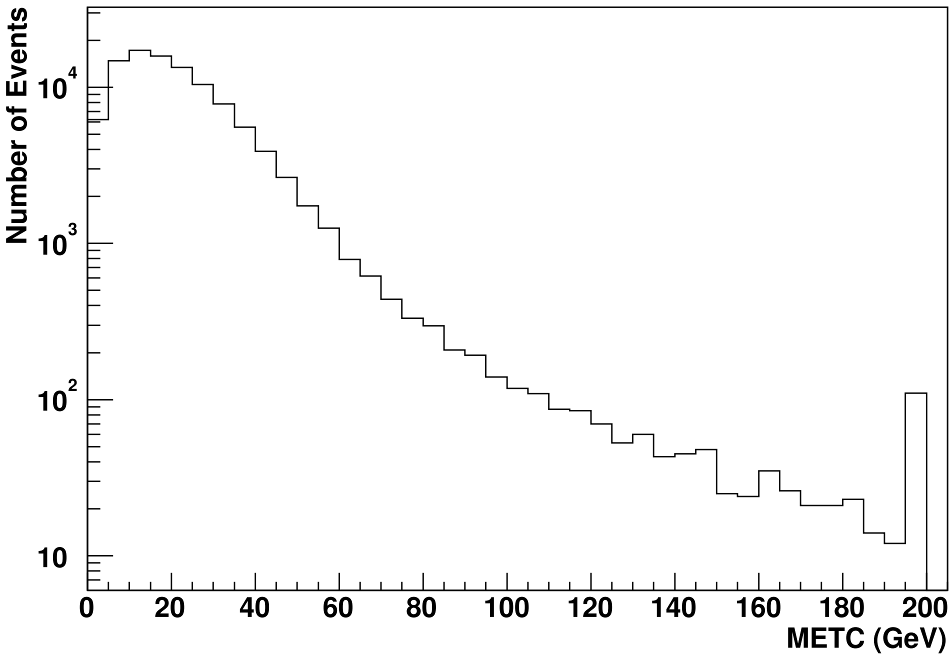

Figure 5.6: The METC spectrum for all events that passed the JT_95TT trigger. This distribution is capped at 200 GeV, with all overflows appearing in the last bin.

The histograms in Fig. 5.7 show the ratio of $p_T[0]$ to METC for all jets in six regions of p_T. There is one entry for each central jet, despite the fact that $p_T[0]$/METC has a unique value for any event. Consequently, an event with four central jets contribute four identical entries to the distributions. (This was done to make corrections to the cross section easy to apply.) The fits shown in this figure are discussed below.

The jets providing entries to these plots have met all other event and jet quality requirements, except for METC. The peak at $p_T[0]/\text{METC} \approx 1$ is likely to be caused by background processes such as cosmic rays and calorimeter malfunctions. This is consistent with the observation that the peak is most pronounced in the distribution for leading jets in Fig. 5.8, which includes all single-jet events.

As can be seen from Fig. 5.6, the METC variable is set equal to 200 GeV for all values of METC $\geqslant$ 200 GeV, and we therefore required that all acceptable events have METC $<$ 200 GeV. This requirement removes events only with $p_T[0] \gtrsim 286$ GeV/c because if the leading jet has less transverse momentum, our $p_T[0]/\text{METC}$ requirement removes it. The value is not precisely 286 GeV/c, because the selection is applied based on the transverse momentum before the JES correction is applied. A scan of the rejected events indicates that they can all be attributed to background and not to multiple jet final states.

To determine the fraction of good events that are affected by the $\text{METC}/p_T[0]$ requirement, we extrapolate linearly the signal assumed in Fig. 5.7 to the background region. We also estimate the contamination of the final jet sample from, for example, cosmic ray events, by extrapolating the peak at small $p_T[0]/\text{METC}$ to the signal region, assuming a Gaussian distribution for background. These fits are indicated in Fig. 5.7, and provide a good description of the data. The statistics for the highest region of p_T are too poor to perform a fit. This presents no problem because the METC < 200 GeV requirement makes the $p_T[0]/\mathrm{METC}$ requirement redundant in this region because it is not possible to have sufficient METC for the event to be rejected. The criterion of the ratio is fully efficient in this range. The estimated values for efficiency and background are highly correlated, and we therefore quote only a single result for the correction factor c_{MET}:

$$c_{MET} = 1 + \frac{S_{\mathrm{out}} - B_{\mathrm{in}}}{N_{\mathrm{MET}}} \tag{5.2}$$

where N_{MET} is the number of events that satisfy the $\not{E}_T$ requirements, and S_{out} and B_{in} are the fitted integrals for the signal that fails and the background that passes the requirement, respectively. To estimate the uncertainty of this procedure, the correction factors are re-evaluated after fitting a Gaussian function to the signal instead of a linear form. These fits assume a much wider signal region. The difference of the two correction factors is quoted as the corresponding uncertainty. The correction factors are consistent with unity, and the uncertainties in those factors are $\leqslant 2\%$. The values for each region of transverse momentum are listed in Table 5.3.

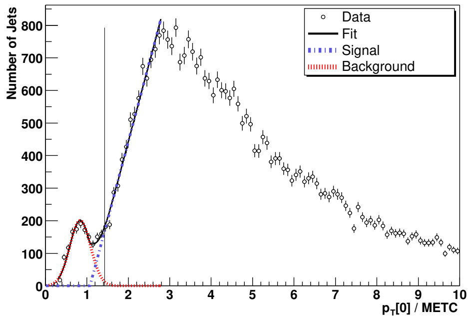

(a) $60 < p_T < 100$ GeV/c

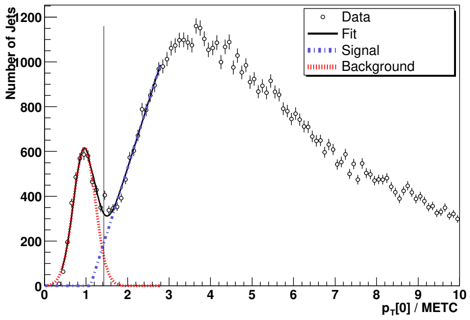

(b) $100 < p_T < 140$ GeV/c

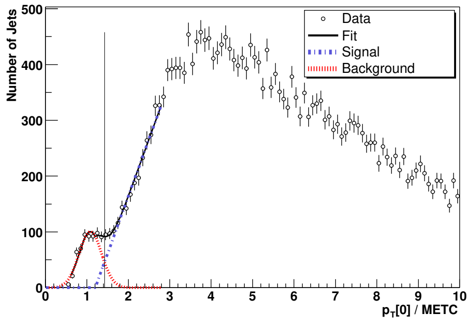

(c) $140 < p_T < 180$ GeV/c

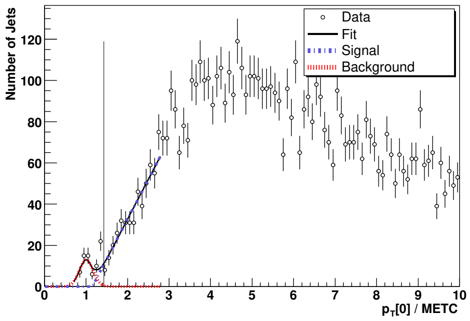

(d) $180 < p_T < 230$ GeV/c

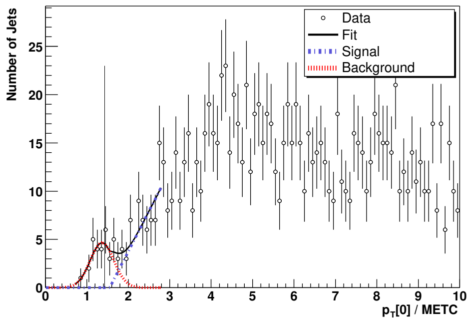

(e) $230 < p_T < 320$ GeV/c

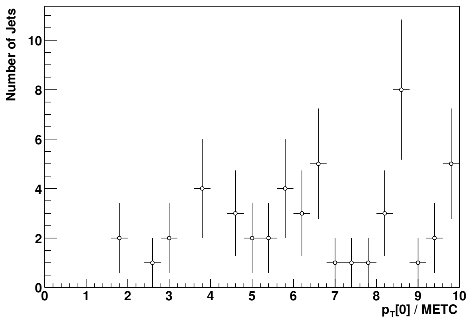

(f) $p_T > 320$ GeV/c

Figure 5.7: Distribution in the ratio $p_T[0]$/METC for all central jets in different ranges of jet p_T. A fit to signal and background is indicated by the solid curve with separate contributions appearing as dotted curves (see text). The vertical line represents the chosen requirement, with jets to the right kept for the cross section measurement.

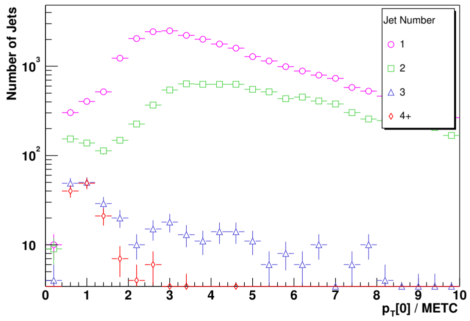

(a) $60 < p_T < 100$ GeV/c

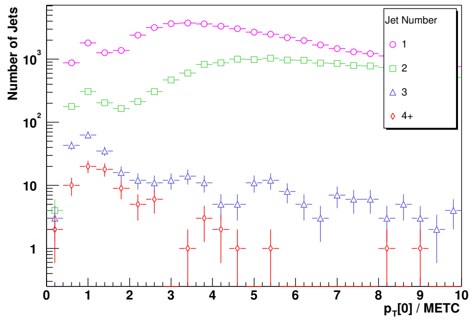

(b) $100 < p_T < 140$ GeV/c

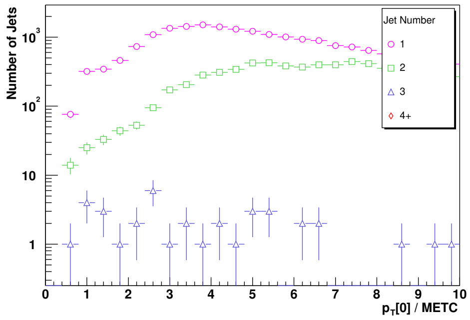

(c) $140 < p_T < 180$ GeV/c

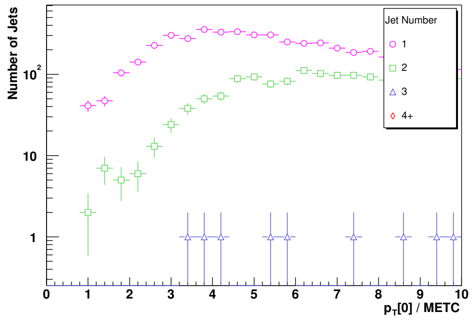

(d) $180 < p_T < 230$ GeV/c

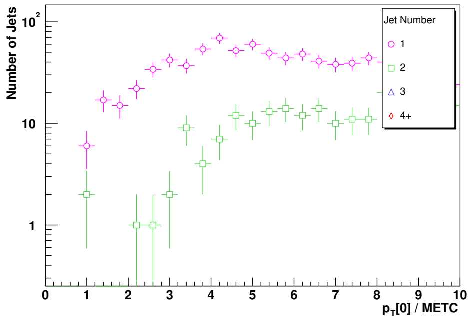

(e) $230 < p_T < 320$ GeV/c

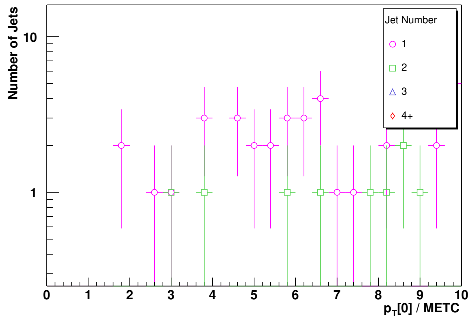

(f) $p_T > 320$ GeV/c

Figure 5.8: The distributions in the ratio $p_T[0]$/METC, with an entry for each central jet that is used in the final cross section measurement, separated into the leading (1), second leading (2), etc. jets in the event. An event where the three leading jets all enter the measurement contributes three entries at the same value of $p_T[0]$/METC, one as a leading jet, one as a second jet, and one as a third jet, but at different values of p_T.

p_T range (GeV/c)	correction for $p_T[0]$/METC	signal removed	background kept	total jets remaining
60 - 100	1.01 ± 0.02	297.6	11.9	25933
100 - 140	1.00 ± 0.02	310.1	162.1	59681
140 - 180	1.00 ± 0.01	52.4	70.7	30023
180 - 230	1.00 ± 0.01	19.8	0.0	8417
230 - 320	1.00 ± 0.01	0.3	7.5	1814
> 320	1.00 ± 0.00	0	0	125

Table 5.3: Corrections to the cross section for $p_T[0]$/METC requirement

5.2 Jet-Quality Criteria

As discussed in Section 3.10, the standard DØ reconstruction software sometimes reconstructs noise and background as jets. To minimize contamination from this background, requirements are placed on jet parameters to assure acceptable jet quality. The requirements are given in Table 5.4 and discussed in this section.

coarse hadronic fraction	CHF $<$ 0.4
electromagnetic fraction	0.05 $<$ EMF $<$ 0.95
hot "fraction"	HotF $<$ 10
number of towers containing 90% of the jet's E_T	n90 $>$ 1
two-dimensional requirement	(CHF $<$ 0.1) or (f90ch $<$ 0.8)

Table 5.4: The jet-quality criteria

In the following sections, we discuss each selection criterion separately. There are two distributions presented for each requirement. One shows the spectra for the variable under discussion, separated into six regions of jet transverse momentum, and the second figure shows the same spectra, but further separated by the jet's ordering in transverse momentum.

Although the requirements may not appear to be optimized for a measurement of the inclusive jet cross section, nevertheless, we use them because the jet energy scale (see Chapter 6) was established from a jet sample that used these chosen criteria. We use our data to determine the efficiency of each requirement as a function of jet transverse momentum, and then apply the corrections to the cross section caused by any observed loss in efficiency.

5.2.1 Coarse Hadronic Fraction

The coarse hadronic fraction (CHF) is defined as the fraction of a jet's measured uncorrected energy that is deposited in the coarse hadronic layer of the calorimeter. Usually, CHF is between zero and one, but can be outside that range because calorimeter cells sometimes readout negative values for energy (see Section 3.7). Only a fraction of shower energy should be deposited in this outermost layer, and therefore when a large fraction of a jet's energy is found here, it suggests that there might be a problem, usually because of noise in the electronics. To limit contamination from such noise, we require CHF < 0.4.

Figures 5.9 and 5.10 show the distributions in CHF for jets, after applying all other quality criteria. Less than 1% of jets are removed by this requirement.

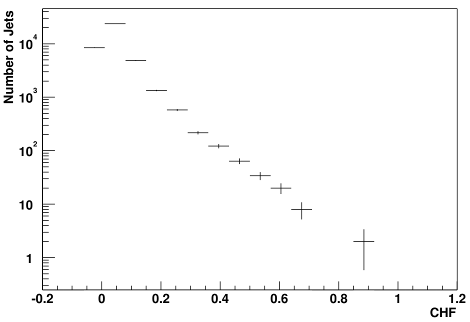

(a) $60 < p_T < 100$ GeV/c

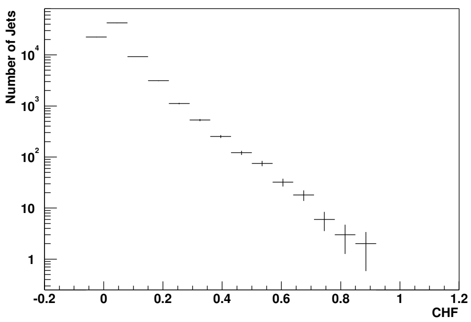

(b) $100 < p_T < 140$ GeV/c

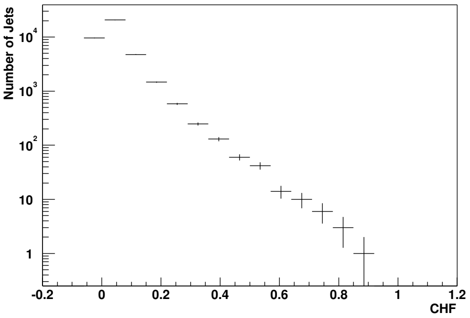

(c) $140 < p_T < 180$ GeV/c

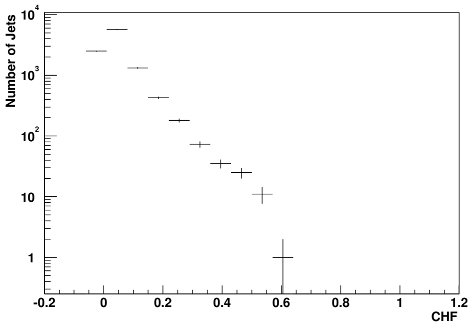

(d) $180 < p_T < 230$ GeV/c

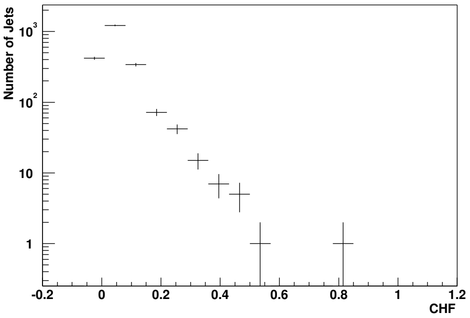

(e) $230 < p_T < 320$ GeV/c

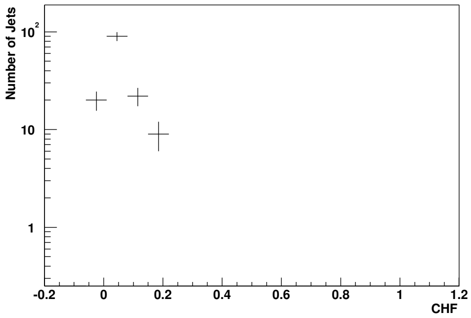

(f) $p_T > 320$ GeV/c

Figure 5.9: Distributions in CHF for jets in different ranges of p_T with jets passing all other requirements. We require CHF < 0.4 for further analysis.

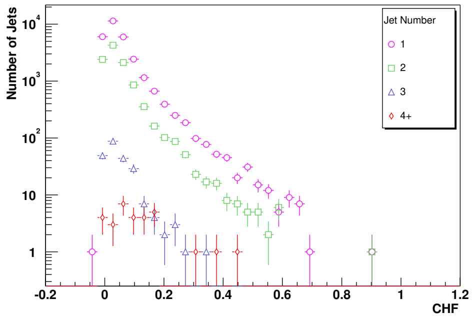

(a) $60 < p_T < 100$ GeV/c

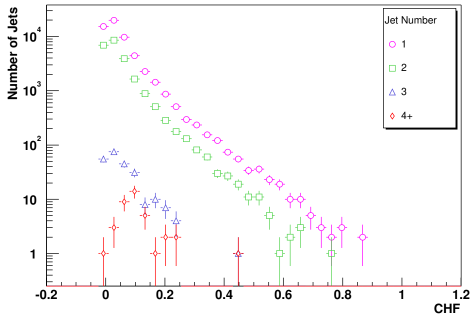

(b) $100 < p_T < 140$ GeV/c

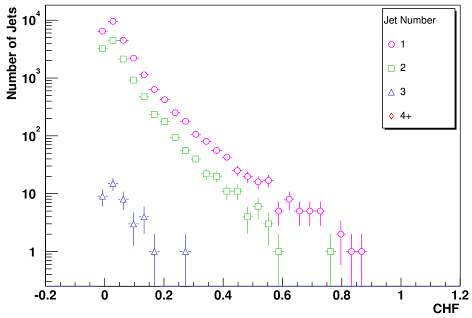

(c) $140 < p_T < 180$ GeV/c

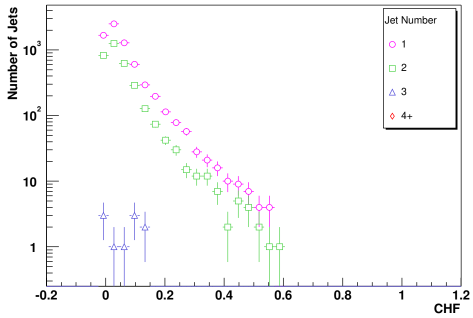

(d) $180 < p_T < 230$ GeV/c

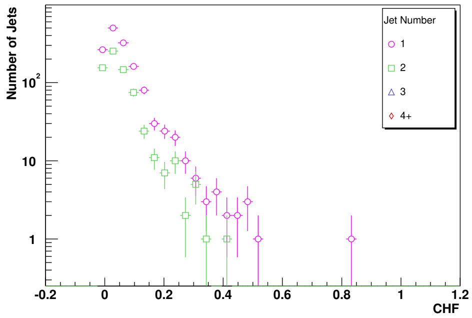

(e) $230 < p_T < 320$ GeV/c

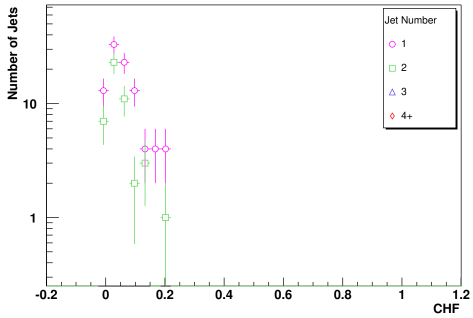

(f) $p_T > 320$ GeV/c

Figure 5.10: Distributions in CHF for jets in different ranges of p_T with jets passing all other requirements. The spectra have been split based on jet p_T ordering. We require CHF < 0.4 for further analysis.

5.2.2 Electromagnetic Fraction

The electromagnetic fraction (EMF) is the fraction of a jet's measured uncorrected energy that is deposited in the four electromagnetic layers of the calorimeter. The distributions in EMF are shown in Figs. 5.11 and 5.12, as usual, separated into several regions of jet transverse momentum. As for CHF, EMF can range somewhat above one and below zero. Unlike the CHF, the EMF for good jets can vary widely. Some jets contain many neutral pions that decay into two photons and therefore shower predominantly in the EM layers of the calorimeter. Other jets have few or no neutral pions and shower almost entirely in the hadronic sections of the calorimeter.

Every jet used for the cross section must satisfy the selection requirement $0.05 < \mathrm{EMF} < 0.95$. Jets with extreme values are likely to have been created by a few noisy cells in the calorimeter. It is also likely that jets with very high values of EMF correspond to photons or electrons.

There are some intriguing features in the EMF spectra. Figure 5.11 shows that lower-p_T jets seem, on average, to have higher values of EMF. Figure 5.12 may help to clarify this effect. It shows that leading jets tend to have lower EMF than second, third, and fourth jets, which is not surprising since showers caused by higher energy particles require more interaction lengths to deposit their energy than showers of lower energy [40]. For this analysis, the most important fact to note is that just like the CHF requirement, we remove less than 1% of the jets from our sample as a result of this selection criterion.

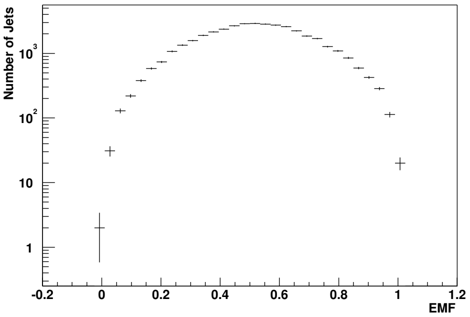

(a) $60 < p_T < 100$ GeV/c

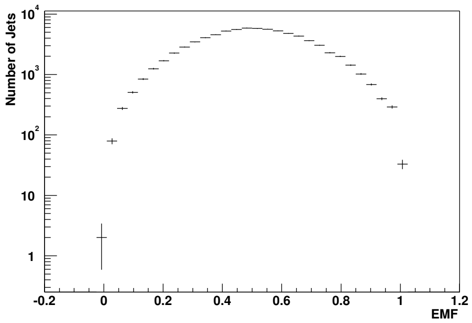

(b) $100 < p_T < 140$ GeV/c

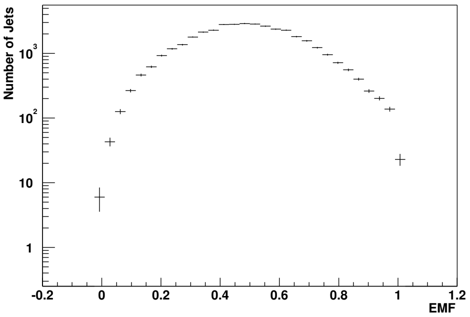

(c) $140 < p_T < 180$ GeV/c

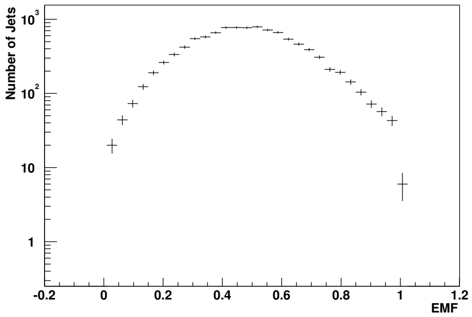

(d) $180 < p_T < 230$ GeV/c

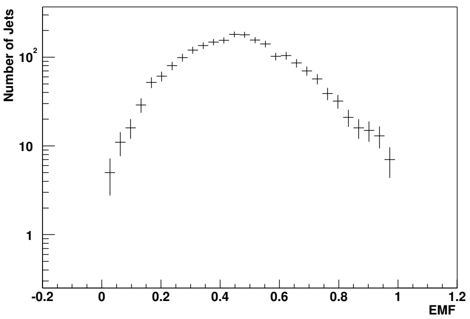

(e) $230 < p_T < 320$ GeV/c

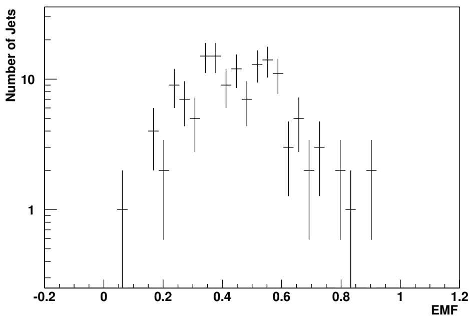

(f) $p_T > 320$ GeV/c

Figure 5.11: Distributions in EMF for jets in different ranges of p_T with jets passing all other requirements. We require $0.05 < \mathrm{EMF} < 0.95$ for further analysis.

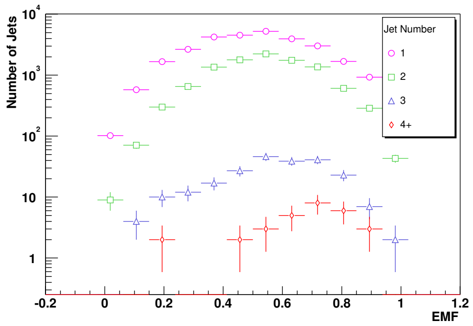

(a) $60 < p_T < 100$ GeV/c

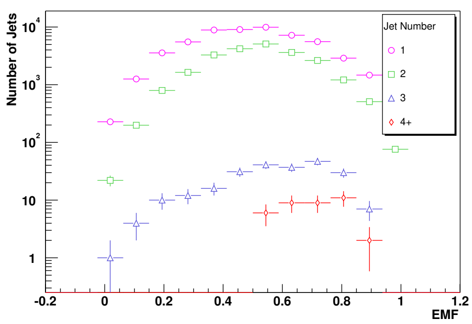

(b) $100 < p_T < 140$ GeV/c

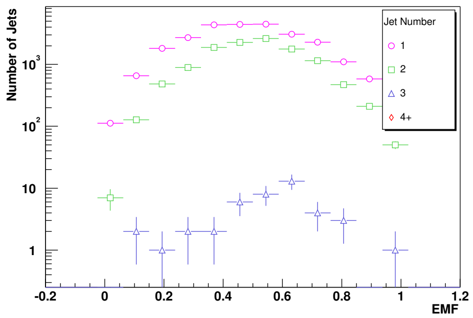

(c) $140 < p_T < 180$ GeV/c

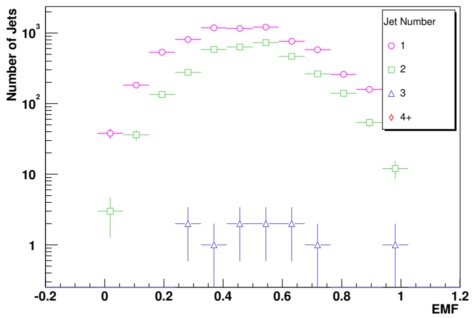

(d) $180 < p_T < 230$ GeV/c

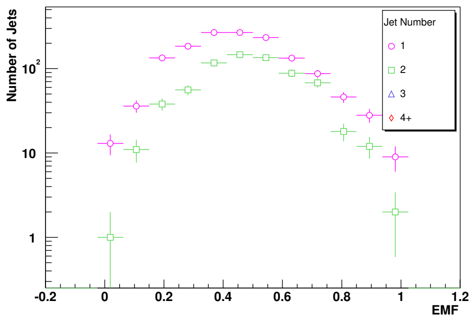

(e) $230 < p_T < 320$ GeV/c

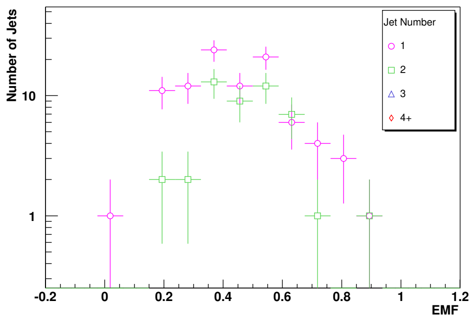

(f) $p_T > 320$ GeV/c

Figure 5.12: Distributions in EMF for jets in different ranges of p_T with jets passing all other requirements. The spectra have been split based on jet p_T ordering. We require $0.05 < \mathrm{EMF} < 0.95$ for further analysis.

5.2.3 Hot Fraction

The "hot fraction" (HotF) of a jet is defined as the largest uncorrected transverse energy observed in any cell divided by that found in the second highest cell in a jet, and must be greater than unity. When a jet has a very large value for HotF, then that jet is likely to have been caused by substantial noise in one readout cell of the calorimeter. Even if a jet has a very energetic particle in it, we would not expect a factor of ten more energy in one cell than in its neighboring layers, and we therefore require good jets to have HotF< 10. This criterion removes only $\approx$0.2% of all jets. Figures 5.13 and 5.14 show the distributions in HotF after all other selection requirements are applied to the data.

5.2.4 The n90 Variable

The variable n90 is defined as the minimum number of towers that contain at least 90% of a jet's measured uncorrected transverse energy. The major difference between n90 and HotF is that HotF refers to single readout cells and not full towers. When a jet is caused by two hot channels in the same tower, a selection on HotF will not remove it, while a requirement on n90 can. Distributions in this variable, with all other requirements applied, are shown in Figs. 5.15 and 5.16. We require n90 > 1. This requirement removes less than 0.001 of all jets.

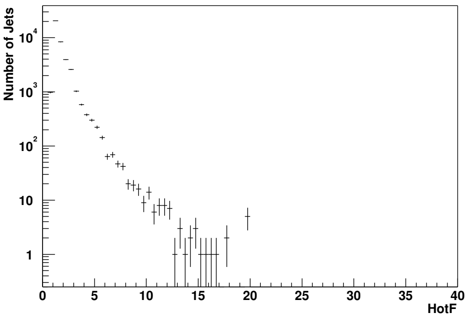

(a) $60 < p_T < 100$ GeV/c

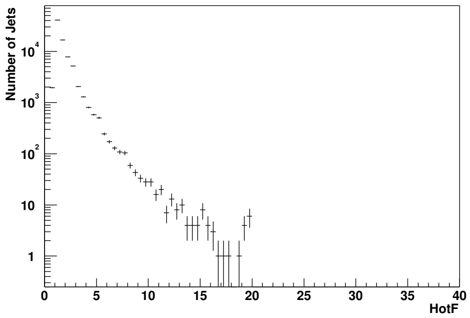

(b) $100 < p_T < 140$ GeV/c

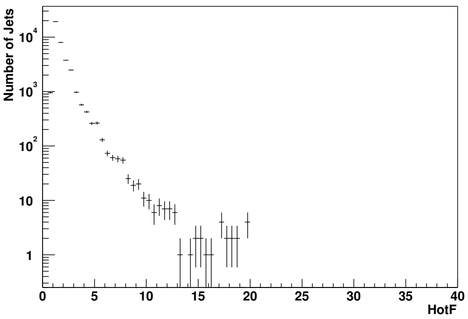

(c) $140 < p_T < 180$ GeV/c

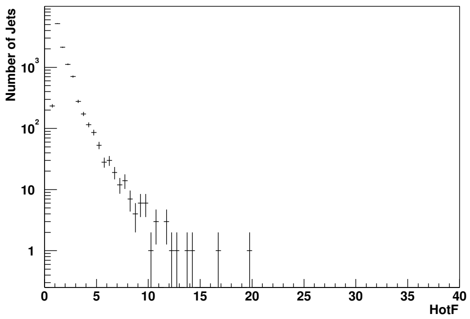

(d) $180 < p_T < 230$ GeV/c

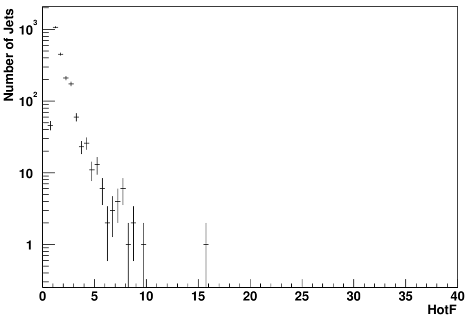

(e) $230 < p_T < 320$ GeV/c

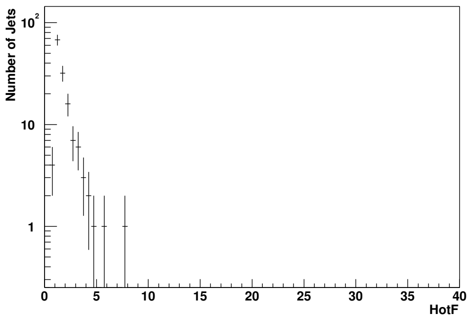

(f) $p_T > 320$ GeV/c

Figure 5.13: Distributions in HotF for jets in different ranges of p_T with jets passing all other requirements. We require HotF < 10 for further analysis.

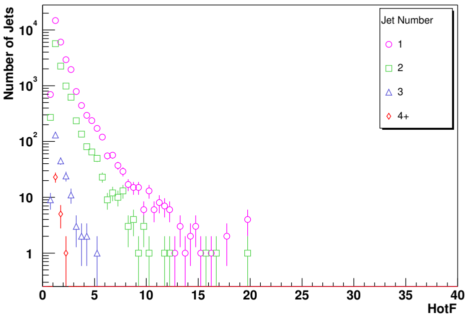

(a) $60 < p_T < 100$ GeV/c

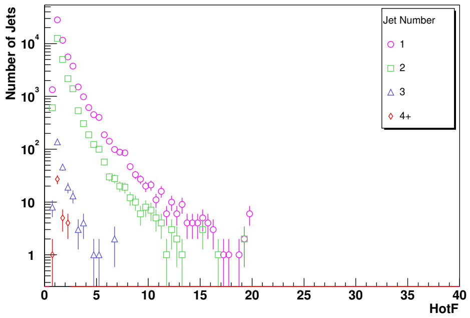

(b) $100 < p_T < 140$ GeV/c

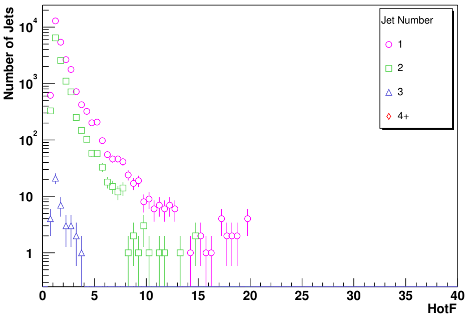

(c) $140 < p_T < 180$ GeV/c

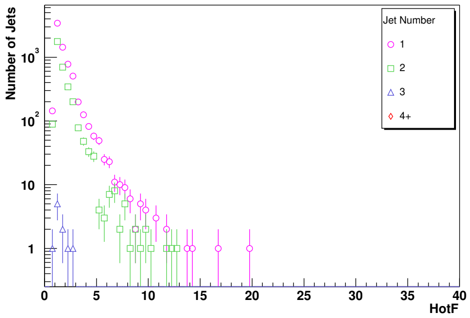

(d) $180 < p_T < 230$ GeV/c

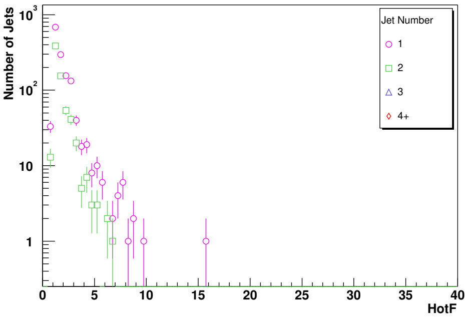

(e) $230 < p_T < 320$ GeV/c

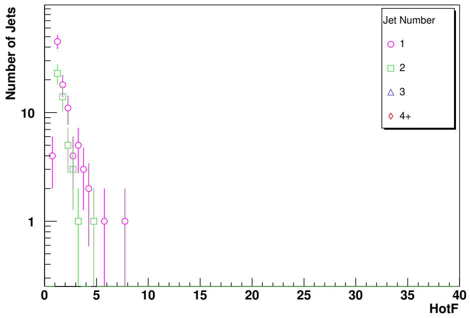

(f) $p_T > 320$ GeV/c

Figure 5.14: Distributions in HotF for jets in different ranges of p_T with jets passing all other requirements. The spectra have been split based on jet p_T ordering. We require HotF < 10 for further analysis.

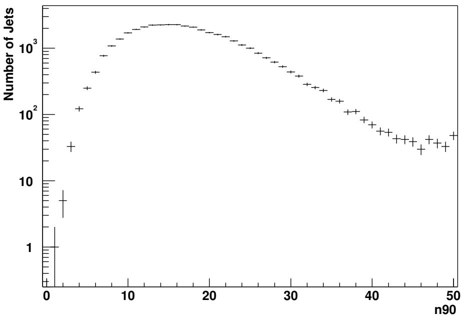

(a) $60 < p_T < 100$ GeV/c

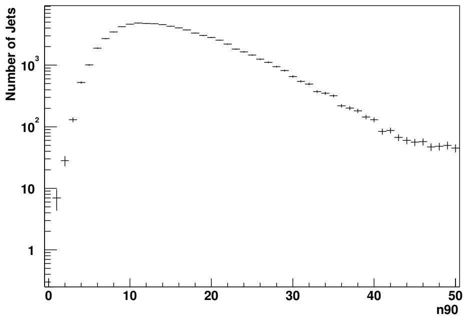

(b) $100 < p_T < 140$ GeV/c

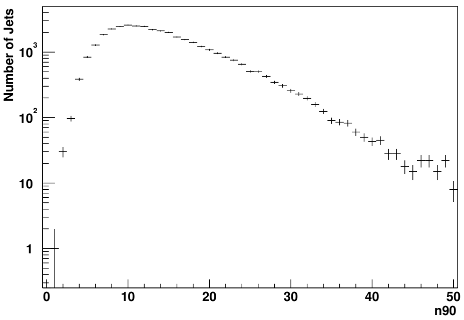

(c) $140 < p_T < 180$ GeV/c

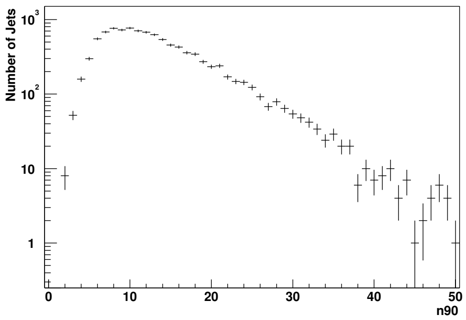

(d) $180 < p_T < 230$ GeV/c

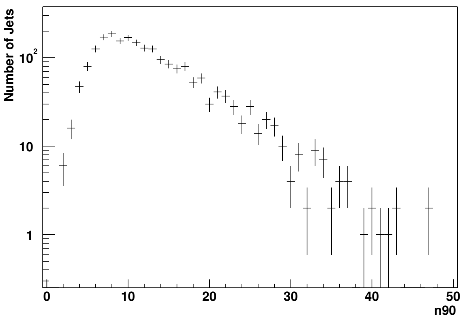

(e) $230 < p_T < 320$ GeV/c

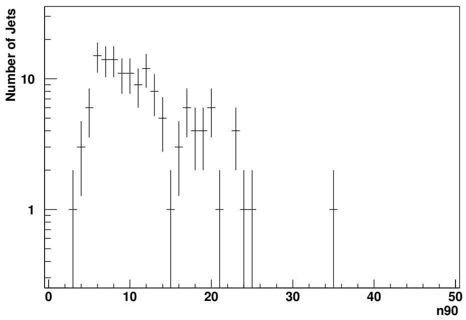

(f) $p_T > 320$ GeV/c

Figure 5.15: Distributions in n90 for jets in different ranges of p_T with jets passing all other requirements. We require n90 > 1 for further analysis.

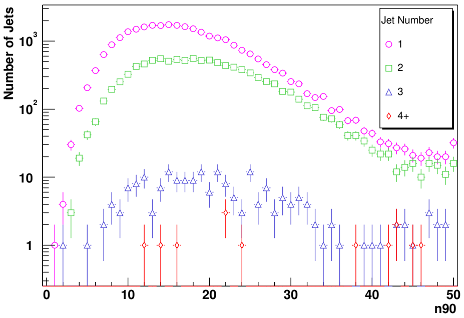

(a) $60 < p_T < 100$ GeV/c

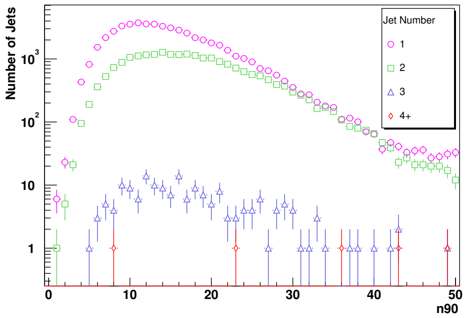

(b) $100 < p_T < 140$ GeV/c

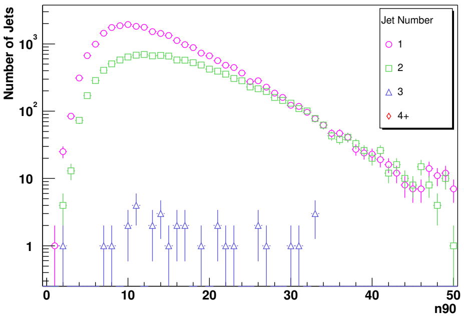

(c) $140 < p_T < 180$ GeV/c

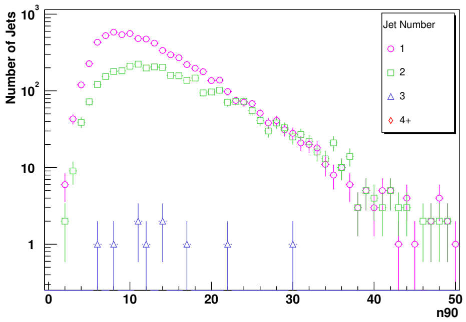

(d) $180 < p_T < 230$ GeV/c

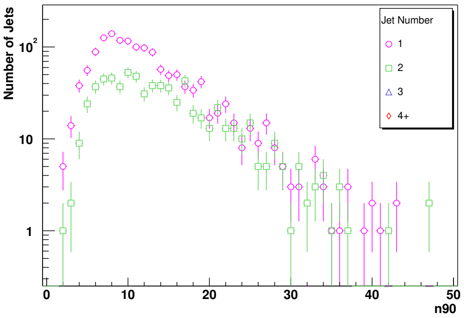

(e) $230 < p_T < 320$ GeV/c

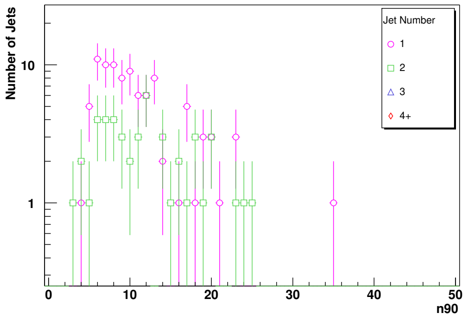

(f) $p_T > 320$ GeV/c

Figure 5.16: Distributions in n90 for jets in different ranges of p_T with jets passing all other requirements. The spectra have been split based on jet p_T ordering. We require n90 > 1 for further analysis.

5.2.5 Correlated Requirement

About 2% of all jets were found to be generated from noise in the coarse hadronic layer of the calorimeter, and through the merging process acquired more energy outside of the CH, and thereby passed the CHF criterion. Another requirement that was correlated with CHF was therefore needed to remove this contamination, and we introduced a final jet-quality requirement to be applied in the plane of the variables CHF and f90. To describe the selection, we define f90ch and f90 as follows:

$$\mathrm{f90ch} \equiv \mathrm{f90} + 0.5 \times \mathrm{CHF} \qquad \text{where} \qquad \mathrm{f90} \equiv \frac{\mathrm{n90}}{\mathrm{nItems}} \tag{5.3}$$

where n90 is defined above, and nItems is the total number of towers in the jet that contain measured uncorrected transverse energy. To contain energy, a readout cell has to be more than 2.5 standard deviations from its mean value with no signal, negative or positive. The tower is counted in nItems if its total energy is positive. The requirement we impose is:

$$\mathrm{CHF} < 0.1 \qquad \text{OR} \qquad \mathrm{f90ch} < 0.8 \tag{5.4}$$

The distributions in f90ch, for jets with CHF > 0.1 are shown in Figs. 5.17

and 5.18, after application of all other jet quality criteria. The bumps in these spectra at high values of f90ch correspond to jets with multiple merges, often more than four.

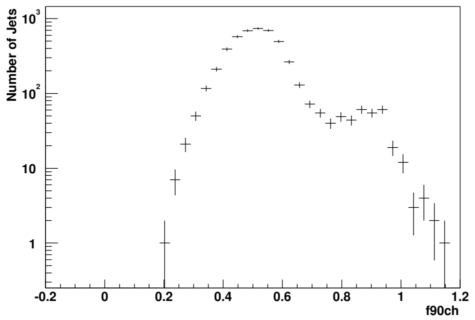

(a) $60 < p_T < 100$ GeV/c

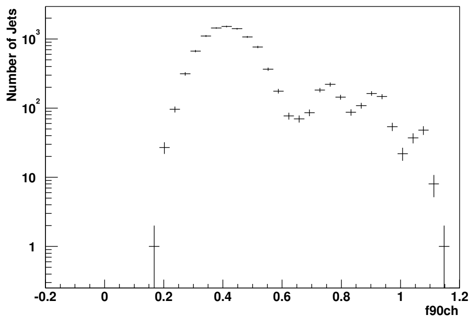

(b) $100 < p_T < 140$ GeV/c

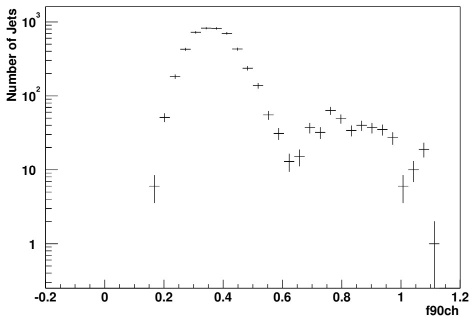

(c) $140 < p_T < 180$ GeV/c

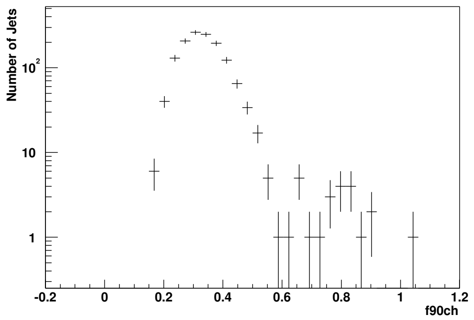

(d) $180 < p_T < 230$ GeV/c

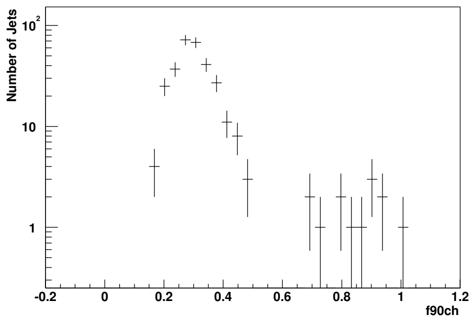

(e) $230 < p_T < 320$ GeV/c

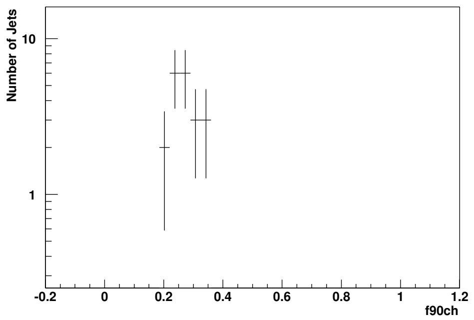

(f) $p_T > 320$ GeV/c

Figure 5.17: Distributions in f90ch for jets in different ranges of p_T with jets passing all other requirements and having CHF > 0.1. We require f90ch < 0.8 for further analysis.

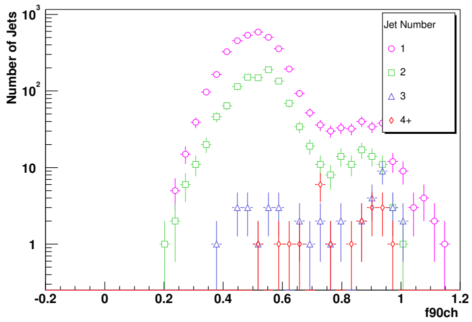

(a) $60 < p_T < 100$ GeV/c

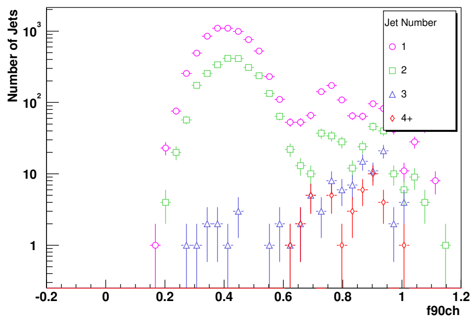

(b) $100 < p_T < 140$ GeV/c

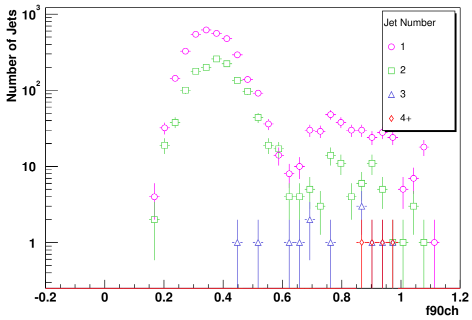

(c) $140 < p_T < 180$ GeV/c

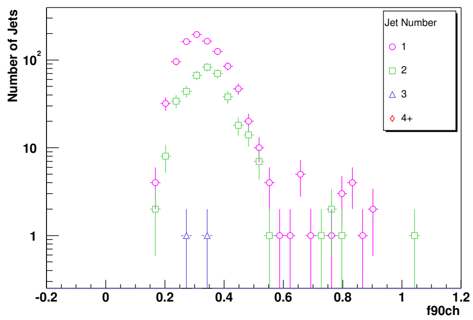

(d) $180 < p_T < 230$ GeV/c

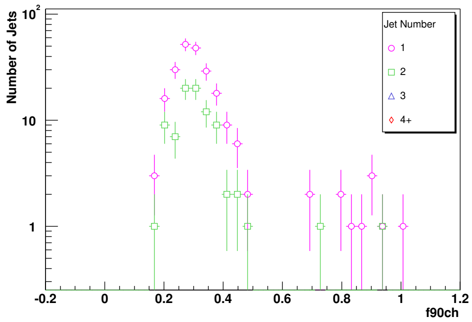

(e) $230 < p_T < 320$ GeV/c

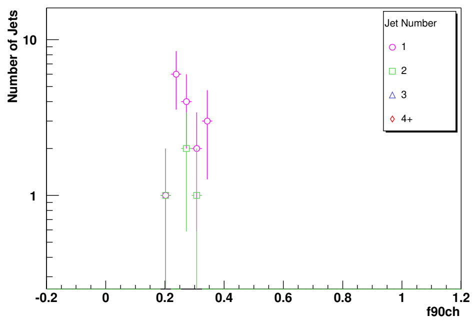

(f) $p_T > 320$ GeV/c

Figure 5.18: Distributions in f90ch for jets in different ranges of p_T with jets passing all other requirements and having CHF > 0.1. We require f90ch < 0.8 for further analysis.

5.2.6 Summary of Jet Selection

To display the effect of jet-quality criteria in greater detail, Fig. 5.19 shows the fraction of jets remaining, after the CHF, EMF, HotF, n90 and f90ch selections are applied to a data sample that has satisfied all other requirements. The fraction of jets that are removed is typically below 0.5%, and never larger than 2.5%. We do not know if these jets should be removed or not, so we assume that half of them should be removed and assign a systematic uncertainty that allows us to either keep all of them or remove all of them. The correction factors that are applied to the data are in Tables 5.5 and 5.6. Table 5.6 also contains the product of all of these corrections.

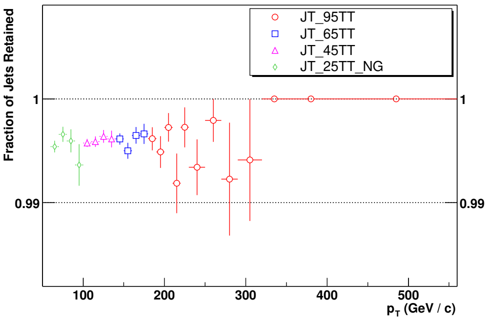

(a) CHF

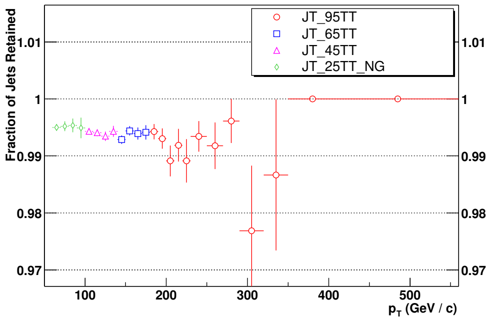

(b) EMF

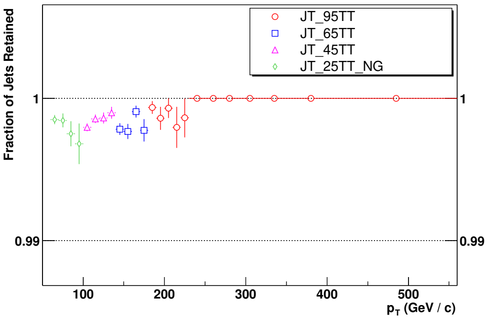

(c) HotF

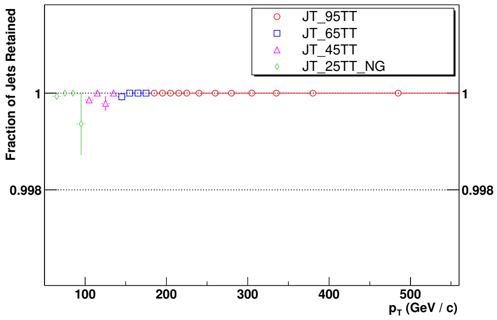

(d) n90

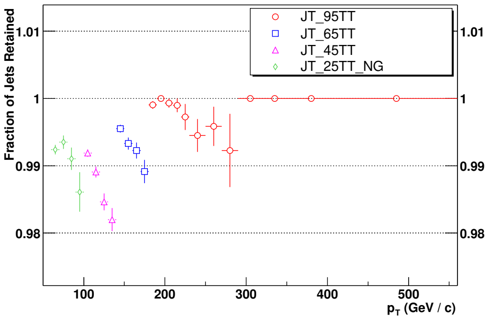

(e) f90ch

Figure 5.19: Fraction of the jets retained after the selection criteria are applied as a function of p_T.

p_T range (GeV/c)	CHF	EMF	HotF
60 − 70	0.9977 ± 0.0023	0.9975 ± 0.0025	0.9993 ± 0.0007
70 − 80	0.9983 ± 0.0017	0.9976 ± 0.0024	0.9992 ± 0.0008
80 − 90	0.9978 ± 0.0020	0.9977 ± 0.0023	0.9987 ± 0.0013
90 − 100	0.9968 ± 0.0032	0.9975 ± 0.0025	0.9984 ± 0.0016
100 − 110	0.9979 ± 0.0021	0.9971 ± 0.0029	0.9990 ± 0.0010
110 − 120	0.9979 ± 0.0021	0.9970 ± 0.0030	0.9993 ± 0.0007
120 − 130	0.9982 ± 0.0018	0.9967 ± 0.0033	0.9993 ± 0.0007
130 − 140	0.9981 ± 0.0019	0.9972 ± 0.0028	0.9995 ± 0.0005
140 − 150	0.9981 ± 0.0019	0.9964 ± 0.0036	0.9989 ± 0.0011
150 − 160	0.9975 ± 0.0025	0.9972 ± 0.0028	0.9988 ± 0.0012
160 − 170	0.9982 ± 0.0018	0.9970 ± 0.0030	0.9995 ± 0.0005
170 − 180	0.9983 ± 0.0017	0.9971 ± 0.0030	0.9989 ± 0.0011
180 − 190	0.9981 ± 0.0019	0.9971 ± 0.0029	0.9997 ± 0.0003
190 − 200	0.9974 ± 0.0026	0.9965 ± 0.0035	0.9993 ± 0.0007
200 − 210	0.9986 ± 0.0014	0.9946 ± 0.0054	0.9997 ± 0.0003
210 − 220	0.9959 ± 0.0041	0.9959 ± 0.0041	0.9990 ± 0.0010
220 − 230	0.9986 ± 0.0014	0.9946 ± 0.0054	0.9993 ± 0.0007
230 − 250	0.9967 ± 0.0033	0.9967 ± 0.0033	1 ± 0
250 − 270	0.9990 ± 0.0010	0.9959 ± 0.0041	1 ± 0
270 − 290	0.9961 ± 0.0039	0.9981 ± 0.0019	1 ± 0
290 − 320	0.9971 ± 0.0029	0.9884 ± 0.0116	1 ± 0
320 − 350	1 ± 0	0.9933 ± 0.0067	1 ± 0
350 − 410	1 ± 0	1 ± 0	1 ± 0
410 − 560	1 ± 0	1 ± 0	1 ± 0

Table 5.5: Jet selection efficiencies.

p_T range (GeV/c)	n90	2D	total efficiency
60 – 70	1 ± 0	0.9962 ± 0.0038	0.9907 ± 0.0051
70 – 80	1 ± 0	0.9968 ± 0.0032	0.9919 ± 0.0045
80 – 90	1 ± 0	0.9956 ± 0.0044	0.9900 ± 0.0056
90 – 100	0.9997 ± 0.0003	0.9931 ± 0.0069	0.9855 ± 0.0082
100 – 110	0.9999 ± 0.0001	0.9959 ± 0.0041	0.9899 ± 0.0055
110 – 120	1 ± 0	0.9945 ± 0.0055	0.9888 ± 0.0066
120 – 130	0.9999 ± 0.0001	0.9923 ± 0.0077	0.9865 ± 0.0086
130 – 140	1 ± 0	0.9910 ± 0.0090	0.9858 ± 0.0096
140 – 150	1 ± 0	0.9978 ± 0.0022	0.9912 ± 0.0047
150 – 160	1 ± 0	0.9967 ± 0.0033	0.9902 ± 0.0052
160 – 170	1 ± 0	0.9961 ± 0.0039	0.9909 ± 0.0053
170 – 180	1 ± 0	0.9946 ± 0.0054	0.9889 ± 0.0065
180 – 190	1 ± 0	0.9995 ± 0.0005	0.9944 ± 0.0035
190 – 200	1 ± 0	1 ± 0	0.9933 ± 0.0044
200 – 210	1 ± 0	0.9997 ± 0.0003	0.9925 ± 0.0057
210 – 220	1 ± 0	0.9995 ± 0.0005	0.9904 ± 0.0059
220 – 230	1 ± 0	0.9986 ± 0.0014	0.9912 ± 0.0058
230 – 250	1 ± 0	0.9973 ± 0.0027	0.9907 ± 0.0057
250 – 270	1 ± 0	0.9979 ± 0.0021	0.9928 ± 0.0047
270 – 290	1 ± 0	0.9961 ± 0.0039	0.9904 ± 0.0058
290 – 320	1 ± 0	1 ± 0	0.9855 ± 0.0119
320 – 350	1 ± 0	1 ± 0	0.9933 ± 0.0067
350 – 410	1 ± 0	1 ± 0	1 ± 0
410 – 560	1 ± 0	1 ± 0	1 ± 0

Table 5.6: Jet selection efficiencies. The final column is the total from all five selection criteria.

Chapter 6

Jet Energy Scale

When the software reconstructs a jet in an event, the jet's energy is calculated initially by summing the energy-momentum four-vectors associated with each calorimeter tower defining the jet. However, because the calorimeter responds to different particles in different ways, the calculated energy may be biased, and must be corrected through a calibration procedure. The jet energy scale (JES) correction is parameterized as follows:

$$E_{corr} = \frac{E_{uncorr} - O}{\rho \cdot S} \tag{6.1}$$

where E_{corr} is the corrected energy and E_{uncorr} is the initial reconstructed energy. O is the offset resulting from calorimeter noise and interactions from other simultaneous $p\overline{p}$ collisions. ρ stands for the response of the calorimeter relative to energy deposited in it. It corresponds to the ratio of observed signal to incident energy, and takes account of any non-linearity, presence of uninstrumented regions in the detector, and the like. S is a correction for physical showering of particles in the detector, and reflects the fact that some of the energy detected inside the cone of a jet may have entered from outside, or vice versa. This occurs when a particle near the edge of the cone produces a shower that crosses the boundary. Also, the solenoid's field can change a particle's trajectory from its emitted angle to an angle outside of a jet's cone, or vice versa.

The parameters O, ρ, and S depend on the position of a jet in the detector as well as on the jet's energy. The parameterization of jet energy scale in this analysis, (v04-01-00 [41]), relies only on a jet's energy and detector η (η_d) defined previously.

Figure 6.1 shows the energy scale corrections (E_{corr}/E_{uncorr}) for ILCA jets with $R = 0.7$. Two of the plots indicate the correction to be applied to the observed energy, and the other two show the uncertainty in the correction.

Currently, all corrections are parameterized in terms of η_d. This accounts for all the main features of the detector, but smaller effects are averaged over. In the future, dependence on azimuthal angle, the fraction of the jet's energy in different layers, and the energy in the preshower detectors will also be taken into account.

Photon plus jet events are used to calculate the jet energy scale correction. We do not require that there be only one jet in the event, but it is required that $\Delta\phi$ between the photon and the leading jet is greater than 2.8 [42]. The energy of a γ can be measured more precisely than a jet's because it is contained in one or at most two towers, EM showers do not have large event-to-event fluctuations [40], and at least 95% of the energy is contained in the four EM layers. The EM layers can be calibrated by using the well known masses of Z^0 and J/ψ particles and their electron-positron decays.

Because a photon's energy can be measured with great precision in γ + jet events, the jet's energy can be deduced from conservation of momentum. From these events, we calculate an average correction for jets of low transverse momentum. The statistical error in Fig. 6.1 gets very large at high energy, because the rate for γ + jet events drops rapidly with increasing p_T.

A single π^0 can often be mistaken for a γ. Also, some jets with high EMF values (rich in π^0s) can be mistaken for photons. A high energy π^0 looks like a γ because it decays into photons that are so close together that the calorimeter cannot resolve them. The result is that a π^0's energy measurement is as precise as a γ's. This means that we can balance it against the other jet, just as if it were a γ [42].

The showering correction S is extracted from the $\gamma+$jet events by looking at how well the jet's transverse momentum balances the photon's transverse momentum as a function jet radius. The response ρ is found by studying the same events, but in this case, the energy is expected to balance with a fixed radius. The offset correction O is found from looking at events that fired the minimum_bias trigger. The energy measured in the calorimeter in such events is not caused by hard scatter processes and so should be subtracted from any jet's energy.

The jet energy scale is applied on each jet individually in this analysis. We do this, rather than include the JES in the reconstruction software, to make it easier to implement corrections. In this way, we can use data reconstructed with different versions of reco and apply to them the same JES corrections.

6.1 Uncertainty in Energy Scale

The uncertainty in the JES arises partially from poor statistics in the γ + jet data. This is represented by the lower curves in Fig. 6.1. The remainder of the uncertainty shown in the figure is from systematics, and can be attributed to several sources. These include the measurement of the γ's energy, uncertainty in position of the vertex, jet, or photon, and possible selection biases from the selection of γ + jet events.

To gauge the impact of the uncertainty in the JES on the cross section, we do the entire analysis three times. First, we use the JES corrections to get jet p_T. In the second and third turns, we assume the jet's energy is one standard deviation lower than the JES prediction and one standard deviation higher. This provides a systematic uncertainty on our measurement of the differential inclusive jet cross section that, at this time, dominates all other uncertainties over the entire range of transverse momentum.

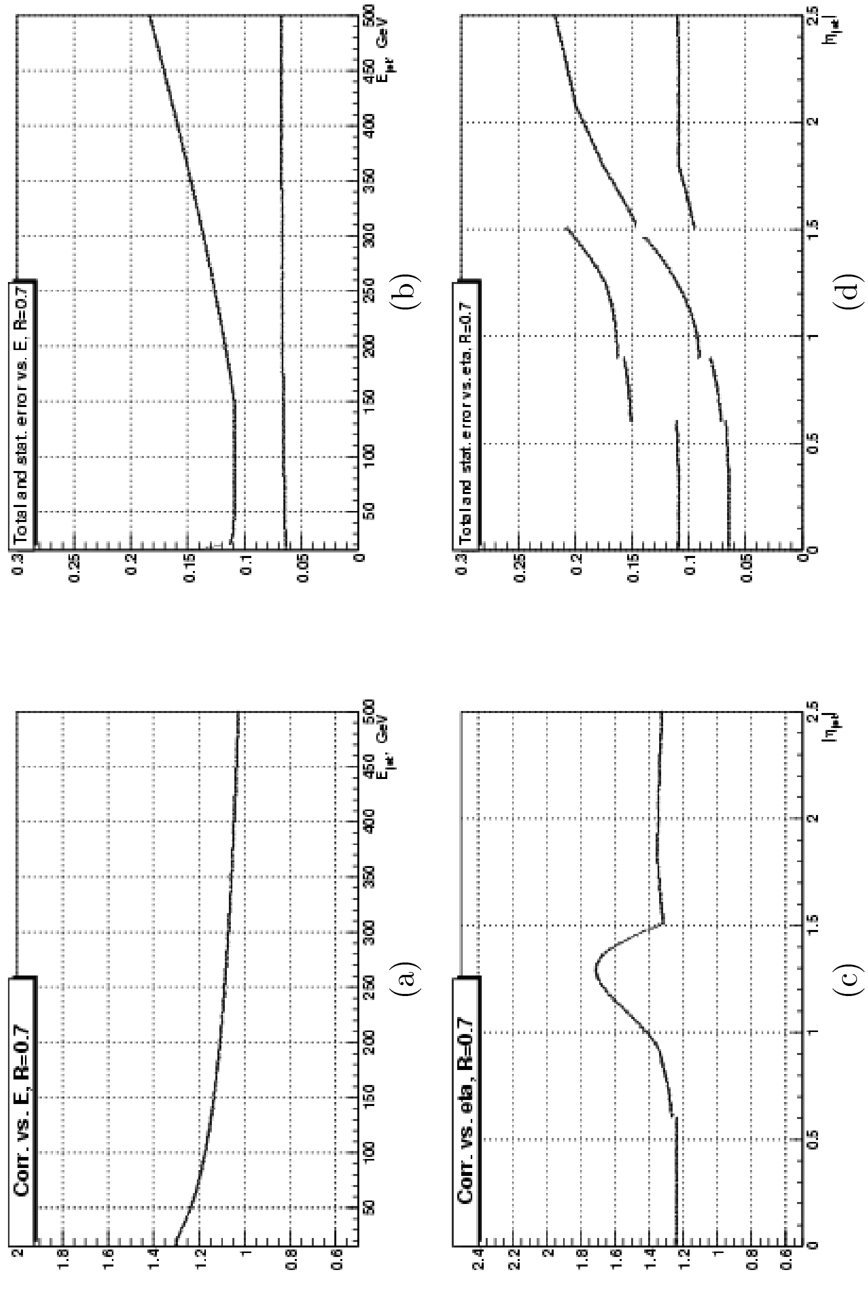

Figure 6.1: The JES correction factors (E_{corr}/E_{uncorr}) for $R = 0.7$ ILCA jets. Plots (a) and (b) are functions of the jet's energy, (a) is the correction and (b) the systematic and total uncertainties. Plots (c) and (d) are as a function of $|\eta_d|$, (c) is the correction and (d) the systematic and total uncertainties. The discontinuities in the $|\eta_d|$ plots correspond to the different regions of the detector; the ICR has a different response than the liquid argon calorimeter.

Chapter 7

Resolution in Jet Momentum

The measured transverse momentum of a jet has an associated uncertainty that affects the differential cross section for jet production. If the resolution is known, it can be deconvoluted from the data, thereby unsmearing or unfolding the observed distribution to extract an improved estimator of the true production cross section. This is the subject of this chapter.

7.1 Jet Transverse Momentum Resolution

The method we used for estimating the p_T resolution of jets is described in detail in Ref. [41]. We examine events containing exactly two jets, and define an asymmetry A for each event:

$$A \equiv \frac{|p_{T1} - p_{T2}|}{p_{T1} + p_{T2}} \tag{7.1}$$

where p_{T1} and p_{T2} are the transverse momenta of the two fully corrected jets. The rms width of this distribution (σ_A) can be related to the resolution in p_T of a single jet (σ_{p_T}) as follows:

$$\frac{\sigma_{p_T}}{p_T} = \sqrt{2} \cdot \sigma_A \tag{7.2}$$

where p_T is the average transverse momentum of the two jets, which are assumed to essentially balance in p_T. Using data very similar to that used in this analysis, the value of σ_{p_T} was determined as a function of p_T. Figure 7.1 shows the resolution with a fit. The functional form of the fit is:

$$\frac{\sigma_{p_T}}{p_T} = \sqrt{\frac{N^2}{{p_T}^2} + \frac{S^2}{p_T} + C^2} \tag{7.3}$$

where the extracted fit parameters for central jets are: $N = 0.0 \pm 2.2$, $S = 0.902 \pm 0.045 \sqrt{\mathrm{GeV/c}}$, and $C = 0.052 \pm 0.008$ GeV/c, with $\chi^2/\mathrm{dof} = 16.6/6$ [41][44]. This parameterization is a model that has worked well in the past [45]. The N term relates to noise fluctuations that dominate in the low momentum range, and the S term is more important at higher momenta where the resolution is dominated by detector imperfections and the different detector response for electromagnetic and hadronic particles [45].

7.2 Unsmearing

For an approximately Gaussian resolution, a jet with a true transverse momentum p_{T0} has the same probability of being measured at $p_{T0} - \delta$ as $p_{T0} + \delta$ for $0 < \delta \ll p_{T0}$. While this smearing is symmetric, the reverse is not true. That is, when a jet's measured transverse momentum is p_{Tm}, it is more likely that the true p_{T0} is $p_{Tm} - \delta$ than $p_{Tm} + \delta$. The reason for this asymmetry is the rapid drop of the cross section with increasing p_T, as discussed below.

Consider the specific example of the true cross section binned as follows: one bin from 100 to 110 GeV/c, another from 110 to 120 GeV/c, and a third from 120 to 130 GeV/c. Suppose the cross section is such that the first bin contains 28000 jets, the next 16000 jets, and the third 9000 jets. Let us consider what happens to the middle bin because of p_T resolution. Suppose that 10% of the jets migrate symmetrically out of that bin, 5% go up and 5% go down in p_T. This decreases the number of jets in the middle bin from 16000 to 14400, but this bin also gains jets from the neighboring bins as follows: it gains 1400 jets (5% of 28000) from the first bin and 450 jets (5% of 9000) from the third bin.

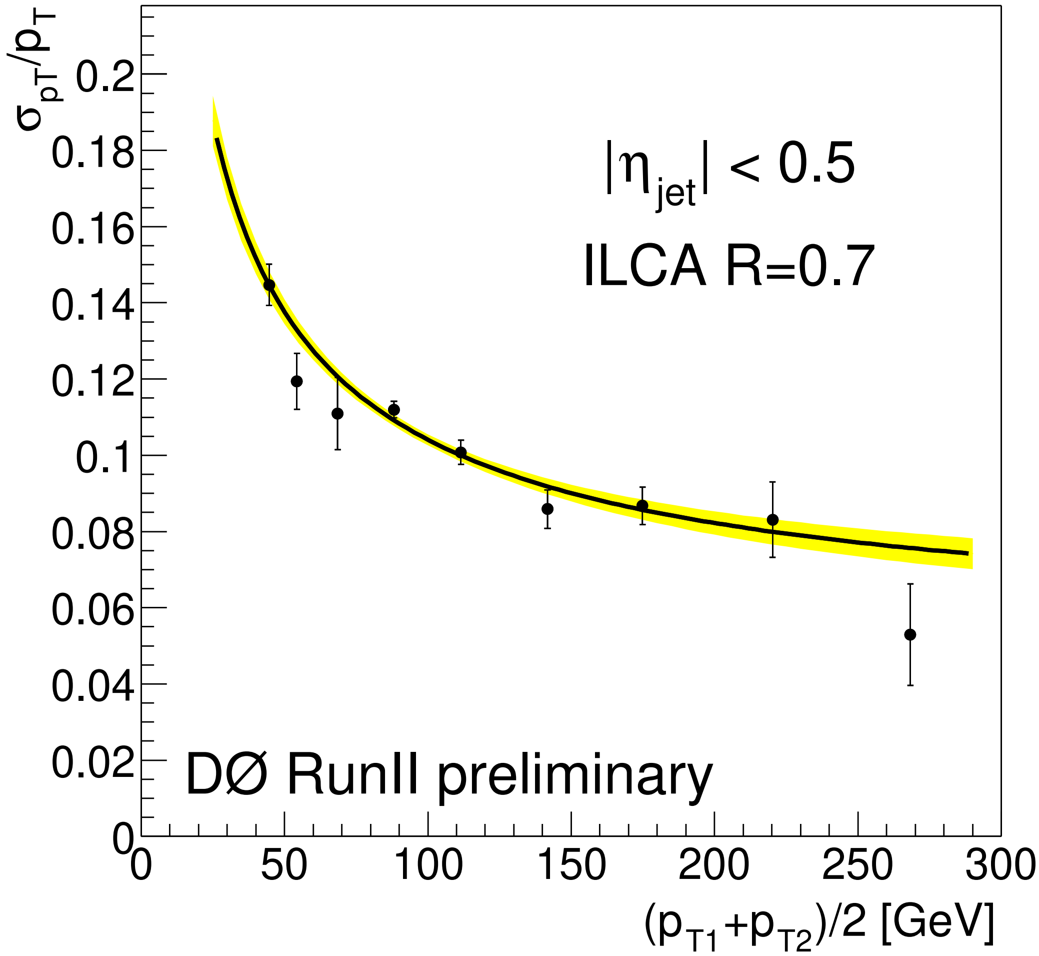

Figure 7.1: The jet transverse momentum resolution estimated from a two-jet data sample. The horizontal axis is equivalent to jet p_T and the vertical axis is the relative uncertainty in p_T. The curve shows a fit to the data (points) corresponding to Eq. 7.3, with an uncertainty band around it that reflects the uncertainties on the fit parameters.

This brings the total in the bin to 16250, which is more than the true value of 16000. Because the bin at lower p_T always loses more jets due to resolution than the higher p_T bin contributes, the observed spectrum shifts to higher p_T. The effect is more pronounced for steeper distributions and poorer resolutions. Clearly, this does not apply to a bin with its lower edge at 0 GeV/c because p_T values are always positive. The feed down begins there.

The observed spectrum $F(p_T)$ can be predicted by convolving the true spectrum $f(p_T)$ with the resolution function $G(p'_T - p_T, p'_T)$:

$$F(p_T) = \int_0^{\frac{\sqrt{s}}{2}} dp'_T \cdot f(p'_T) \cdot G(p'_T - p_T, p'_T) \tag{7.4}$$

where $G(p'_T - p_T, p'_T)$ is assumed to be a Gaussian, with p'_T referring to the true value of transverse momentum in the event. The width of the Gaussian varies with p'_T as in Eq. 7.3. The limits of the integral are set by the range of possible true p_T values for a jet.

Because we do not know the true spectrum, we must assume a fairly generic "Ansatz" function $f(p_T)$ that has several parameters, and then vary those parameters in a fit until the smeared distribution reproduces the measured distribution. Multiplying the measured cross section by the ratio of $f(p_T)$ to $F(p_T)$ provides the final deconvoluted cross section. The function we chose for $f(p_T)$

had four parameters that were extracted through a least squares fit to the data.

$$f(p_T) = f_4(p_T;\nu,\alpha,\beta,\gamma) = 10^{12} \cdot \nu \cdot p_T^{-\alpha} \cdot e^{\frac{-p_T}{\beta}} \cdot \left(1 - \frac{2 \cdot p_T}{\sqrt{s}}\right)^{\gamma} \tag{7.5}$$

The best fit parameters, found using the fitter built into the program Root [46], are in Table 7.1. The $\chi^2/\mathrm{dof} = 20.28/21 = 0.966$, which is acceptable for the fit.

$$\begin{aligned} \nu &= 3.989 \pm 0.505 \\ \alpha &= 4.632 \pm 0.037 \\ \beta &= 102.5 \pm 20.0 \\ \gamma &= 3.435 \pm 1.427 \end{aligned}$$

	β	α	γ	ν
β	1.000	0.773	0.992	0.718
α	0.773	1.000	0.692	0.995
γ	0.992	0.692	1.000	0.633
ν	0.718	0.995	0.633	1.000

Table 7.1: The parameters and correlation coefficients for the fit of function $f_4(p_T)$ to the data.

Using the closed form for $f(p_T)$, we calculate the "weighted center" p_{TC} of each bin in the program Root. It was found using the following equation:

$$f(p_{TC}) = \frac{\int_{p_{T\,low}}^{p_{T\,high}} f(x)\;dx}{p_{T\,high} - p_{T\,low}} \tag{7.6}$$

where $p_{T\,low}$ and $p_{T\,high}$ are the limits of each bin. The data in all plots of the cross section are presented with these weighted points, which can be found in Table 8.1.

The unsmearing was repeated using two other Ansatz functions: $f_3(p_T)$ with three parameters, and $f_{eee}(p_T)$ with six parameters, to check the stability of the result. The comparison to data is given in Figs. 7.2 and 7.3 and appears to produce consistent results. The forms of $f_3(p_T)$ and $f_{eee}(p_T)$ are:

$$f_3(p_T;\nu,\alpha,\gamma) = \nu \cdot p_T^{-\alpha} \cdot \left(1 - \frac{2 \cdot p_T}{\sqrt{s}}\right)^{\gamma} \tag{7.7}$$

$$f_{eee}(p_T;\nu_j,k_j) = \sum_{j=1}^{3} e^{\nu_j + k_j p_T} \tag{7.8}$$

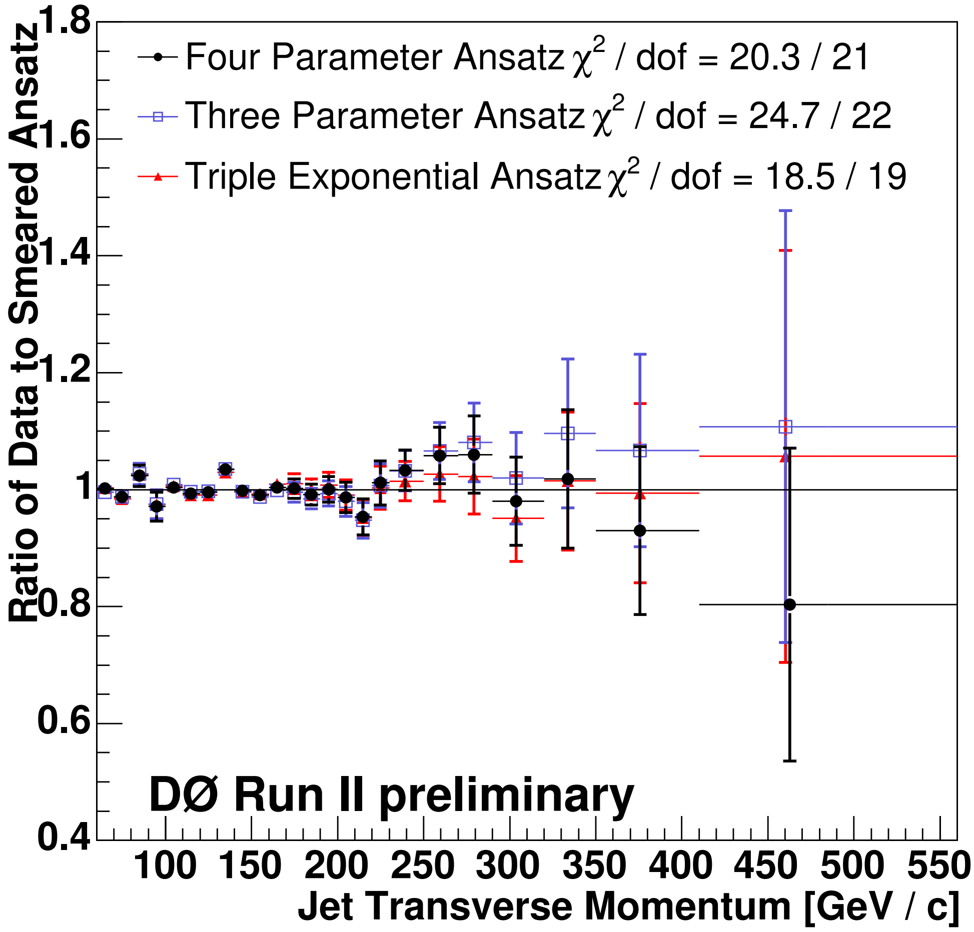

Figure 7.2: The ratio of data to smeared Ansatz functions f_4, f_3, and f_{eee}. The data points are drawn at the cross-section-weighted bin centers found by integrating the different Ansatz functions over individual bins in transverse momentum.

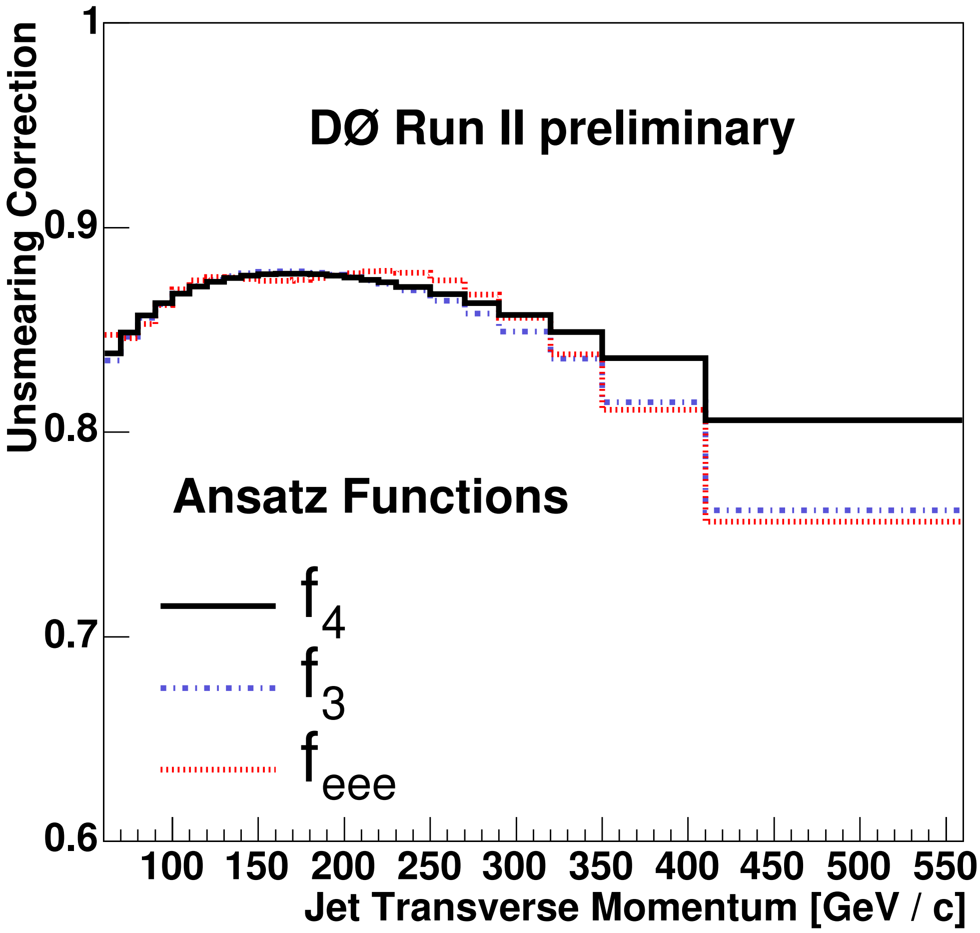

Figure 7.3: Unsmearing correction factors as a function of jet transverse momentum for data, found using the different Ansatz functions f_4, f_3, and f_{eee}.

Chapter 8

The Result and Comparison with Theory

The results presented in this chapter were obtained using the expression discussed in Section 2.4. The differential cross section for each bin of transverse momentum is given by:

$$\left\langle \frac{d\sigma}{dp_T} \right\rangle \bigg|_{p_{T\,average}} = \frac{N_{jets}}{L_{trigger} \times \Delta p_{T\,bin}} \cdot C_{\not{E}_T} \cdot C_{unsmear} \cdot \prod_j \left({\epsilon_j}^{-1} \right) \tag{8.1}$$

where N_{jets} is the number of central ($|\eta| < 0.5$) jets in the bin after they have been corrected for the JES (Chapter 6), $L_{trigger}$ is the integrated luminosity for the trigger used to collect the data, and $\Delta p_{T\,bin}$ is the width of the bin in GeV/c. The C terms are the corrections applied for $\not{E}_T$ and unsmearing, and the ϵ_j correspond to all of the other efficiencies from the imposition of the quality criteria.

The result corresponds to the differential inclusive jet cross section integrated over $|\eta| < 0.5$. The result is shown in Fig. 8.1 and Table 8.1. The data are compared in Fig. 8.1 with a next-to-leading order JETRAD [25] QCD calculation for jet production, using the CTEQ6M [21] parton distribution function, and the parameters given in the figure. The error bars are dominated by systematic uncertainty. Figure 8.2 shows the same results normalized to the theoretical calculation, as well as to a second calculation that used the MRST2001 [20] PDF. The error bars reflect purely statistical uncertainty, and the full uncertainty is indicated by the upper and lower histograms. It is dominated by the uncertainty in the JES.

Although the shape of the MRST2001 curve resembles the results more closely than the CTEQ6M curve, with out current uncertainty in JES, it is not possible to determine which PDFs are favored by the data. With improvement in the understanding of the detector, and with higher statistics, greater sensitivity will become available for a more careful comparison with theory that may also reveal something unexpected at largest momentum transfers. This measurement of the cross section, although limited by systematic uncertainty, is nevertheless

p_T Range (GeV/c)	Cross-Section Weighted Bin Center (GeV/c)	Differential Cross Section (pb/(GeV/c))	Lower Uncertainty (pb/(GeV/c))	Upper Uncertainty (pb/(GeV/c))	Number of Jets	Statistical Uncertainty (%)
60 - 70	64.60	6.95×10^3	4.29×10^3	10.7×10^3	14743	0.82
70 - 80	74.64	3.06×10^3	1.90×10^3	4.90×10^3	6424	1.24
80 - 90	84.68	1.54×10^3	887.	2.36×10^3	3205	1.77
90 - 100	94.71	761.	470.	1.27×10^3	1561	2.53
100 - 110	104.73	431.	249.	685.	28376	0.59
110 - 120	114.75	243.	143.	400.	15950	0.79
120 - 130	124.77	144.	84.2	239.	9412	1.03
130 - 140	134.78	91.3	50.9	145.	5943	1.30
140 - 150	144.79	55.0	30.3	91.9	12912	0.88
150 - 160	154.80	34.9	19.2	60.0	8166	1.11
160 - 170	164.81	23.0	12.1	39.6	5390	1.36
170 - 180	174.82	15.2	7.93	26.4	3555	1.68
180 - 190	184.82	10.1	5.20	18.0	3117	1.79
190 - 200	194.83	6.92	3.46	12.2	2140	2.16
200 - 210	204.84	4.70	2.44	8.65	1455	2.62
210 - 220	214.84	3.16	1.68	6.12	976	3.20
220 - 230	224.84	2.35	1.25	4.37	729	3.70
230 - 250	239.40	1.46	$667. \times 10^{-3}$	2.58	906	3.32
250 - 270	259.43	$771. \times 10^{-3}$	$326. \times 10^{-3}$	1.46	482	4.55
270 - 290	279.45	$408. \times 10^{-3}$	$148. \times 10^{-3}$	$862. \times 10^{-3}$	257	6.24
290 - 320	303.83	$179. \times 10^{-3}$	63.7×10^{-3}	$399. \times 10^{-3}$	169	7.69
320 - 350	333.88	76.6×10^{-3}	19.8×10^{-3}	$180. \times 10^{-3}$	74	11.6
350 - 410	375.82	21.3×10^{-3}	4.34×10^{-3}	61.5×10^{-3}	42	15.4
410 - 560	462.79	1.77×10^{-3}	$186. \times 10^{-6}$	6.83×10^{-3}	9	33.3

Table 8.1: The differential inclusive jet cross section for $|\eta| < 0.5$ as a function of jet transverse momentum. The systematic uncertainty, dominated by the JES, is given by the lower and upper bounds in columns 4 and 5. These uncertainties are completely correlated from bin to bin.

consistent with theoretical prediction over seven orders of magnitude.

If quarks have substructure at an accessible scale it would be exhibited in a rise in cross section at largest transverse momenta due to a new source of deeper interactions. We sketch in Fig. 8.1 the type of departure from QCD that would be observed if the scale of substructure (Λ) is 1 TeV and 2 TeV using the left-handed to left-handed compositeness model built into PYTHIA 6.3 [24], which is discussed in detail in Ref. [47]. This model contains a four fermion interaction with an amplitude proportional to α_s/Λ^2. These scales, which were previously ruled out in Run I [18], correspond to distances on the order of 10^{-19} m. With an improved understanding of the jet energy scale and a factor of sixty more in statistics, we will be able to make a statement about quark substructure at even higher energy scales by the end of Run II.

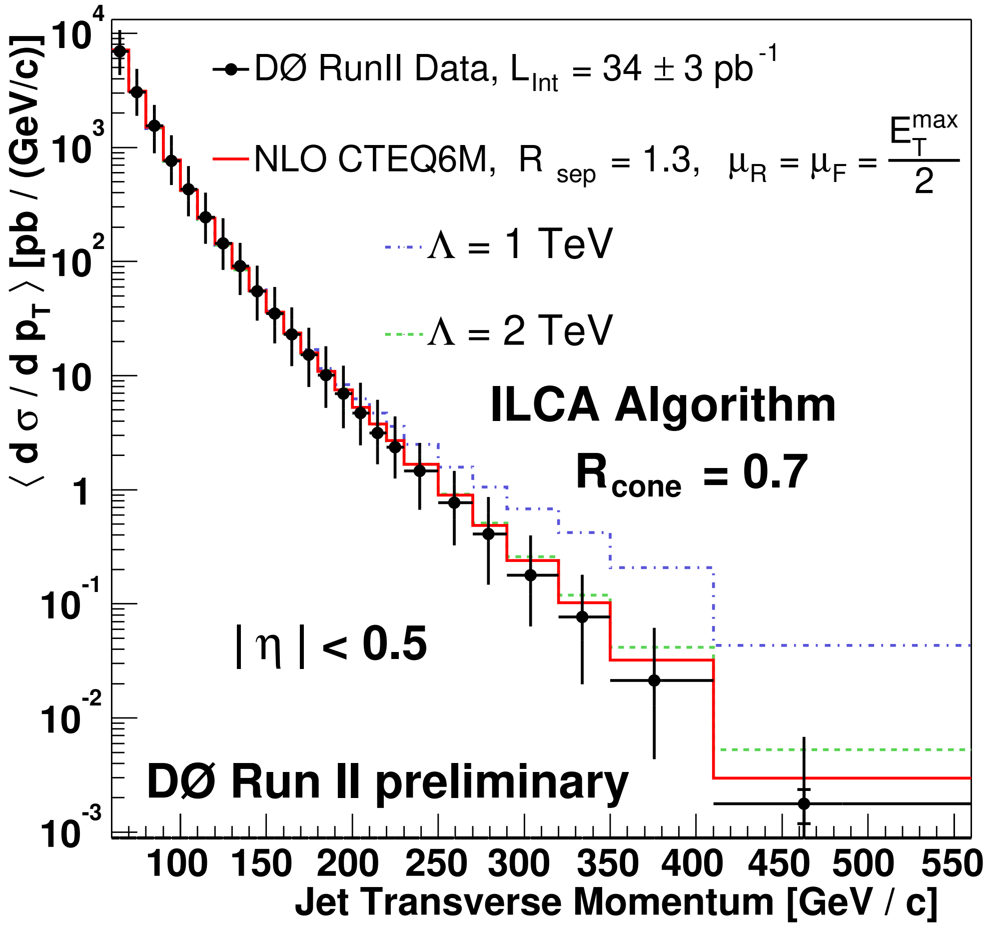

Figure 8.1: The inclusive differential jet cross section as a function of transverse momentum. The data are compared to theoretical predictions of perturbative QCD at NLO, as computed with the program JETRAD (histogram). The error bars include all sources of error except a 10% systematic uncertainty on the normalization from the uncertainty in luminosity. The error bars with horizontal markers indicate the statistical uncertainty, which is negligible except for the highest point in p_T. The dashed histograms labeled $\Lambda = 1$ TeV and $\Lambda = 2$ TeV show the predicted impact of quark substructure at these scales as calculated with PYTHIA.

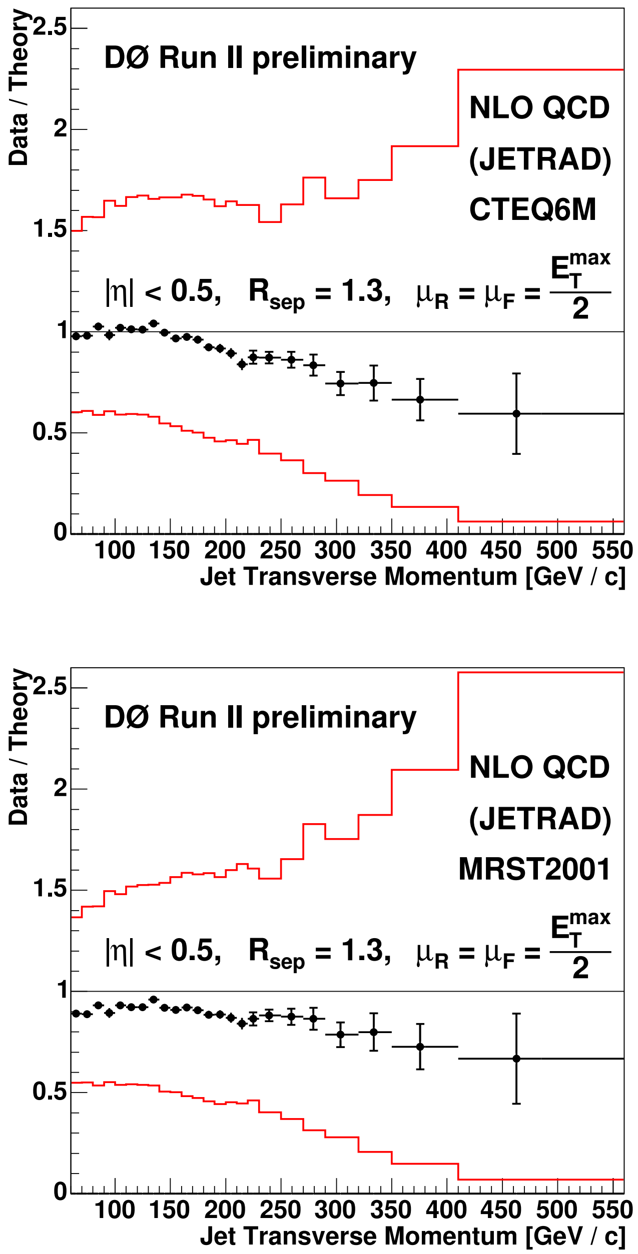

Figure 8.2: The inclusive jet cross section divided by theory as a function of jet p_T. In the upper plot, the theoretical calculation uses the CTEQ6M parameterization for the parton density functions of the proton, and the lower plot uses MRST2001. In both plots, the continuous lines show the single standard deviation uncertainty in JES.

Bibliography

[1] V. V. Ezhela *et al.*, "Particle Physics: One Hundred Years of Discoveries," American Institute of Physics (AIP) Press, Woodbury, New York, 1996.

[2] "Accelerator Concepts Rookie Book", www-bdnew.fnal.gov/operations/rookie_books/Concepts_Rookie_Book_v3.doc.pdf.

[3] Private Communication with Martin Murphy of the Fermilab Accelerator Division, November 2003.

[4] "The Antiproton Source Rookie Book", www-bdnew.fnal.gov/pbar/documents/PBAR_Rookie_Book.PDF.

[5] J.A. MacLachlan, editor, "Prospectus for an Electron Cooling System for the Recycler", www-lib.fnal.gov/archive/1998/tm/TM-2061.html.

[6] L.R. Evans, "The Large Hadron Collider Project," LHC Project Report 53, 1996.

[7] B. Abbott *et al.* [DØ Collaboration], "Hard Single Diffraction in $p\overline{p}$ Collisions at $\sqrt{s}$ = 630 GeV and 1800 GeV," Phys. Lett. B **531**, 52 (2002) [arXiv:hep-ex/9912061].

[8] Gerald C. Blazey *et al.*,"Run II Jet Physics", from "QCD and Weak Boson Physics in Run II", Fermilab-Pub-00/297, edited by U. Baur, R.K. Ellis, and D. Zeppenfeld, pp. 47-77, 2000, or hep-ex/0005012.

[9] S. D. Ellis, J. Huston and M. Tonnesmann, "On building better cone jet algorithms," in *Proc. of the APS/DPF/DPB Summer Study on the Future of Particle Physics (Snowmass 2001)* ed. N. Graf, eConf **C010630**, P513 (2001) [arXiv:hep-ph/0111434].

[10] K. Hagiwara *et al.* [Particle Data Group], "Review of Particle Physics," Phys. Rev. D **66**, 10001 (2002).

[11] S. K. Choi *et al.* [Belle Collaboration], "Observation of a new narrow charmonium state in exclusive $B^{\pm} \to K^{\pm}\pi^{+}\pi^{-}J/\psi$ decays," arXiv:hep-ex/0309032.

[12] R. K. Ellis and W. J. Stirling, "QCD And Collider Physics," FERMILAB-CONF-90-164-T *Based on lectures given at CERN School of Physics, Majorca, Spain, Sep 16-29, 1990 and CERN-JINR School of Physics, Egmond, Netherlands, Jun 25 - Jul 8, 1989.*

[13] V. N. Gribov and L. N. Lipatov, "Deep Inelastic *ep* Scattering In Perturbation Theory," Yad. Fiz. **15**, 781 (1972) [Sov. J. Nucl. Phys. **15**, 438 (1972)]. L. N. Lipatov, "The Parton Model And Perturbation Theory," Sov. J. Nucl. Phys. **20**, 94 (1975) [Yad. Fiz. **20**, 181 (1974)]. G. Altarelli and G. Parisi, "Asymptotic Freedom in Parton Language," Nucl. Phys. B **126**, 298 (1977). Y. L. Dokshitzer, "Calculation of the Structure Functions for Deep Inelastic Scattering and e^+e^- Annihilation by Perturbation Theory in Quantum Chromodynamics. (In Russian)," Sov. Phys. JETP **46**, 641 (1977) Zh. Eksp. Teor. Fiz. **73**, 1216 (1977)].

[14] D. H. Perkins, "Introduction to High Energy Physics, Third Edition", Addison-Wesley Publishing Company, Inc., 1987.

[15] L. W. Whitlow, E. M. Riordan, S. Dasu, S. Rock and A. Bodek, "Precise measurements of the proton and deuteron structure functions from a global analysis of the SLAC deep inelastic electron scattering cross-sections," Phys. Lett. B **282**, 475 (1992).

[16] S. Chekanov *et al.* [ZEUS Collaboration], "Measurement of the neutral current cross section and F2 structure function for deep inelastic e^+p scattering at HERA," Eur. Phys. J. C **21**, 443 (2001) [arXiv:hep-ex/0105090].

[17] C. Adloff *et al.* [H1 Collaboration], "Deep-Inelastic Inclusive ep Scattering at Low x and a Determination of α_s," Eur. Phys. J. C **21**, 33 (2001) [arXiv:hep-ex/0012053].

[18] B. Abbott *et al.* [DØ Collaboration], "High p_T Jets in $p\overline{p}$ Collisions at $\sqrt{s} = 630$ and 1800 GeV," Phys. Rev. D **64**, 032003 (2001) [arXiv:hep-ex/0012046].

[19] T. Affolder *et al.* [CDF Collaboration], "Measurement of the Inclusive Jet Cross Section in $p\overline{p}$ Collisions at $\sqrt{s} = 1.8$ TeV," Phys. Rev. D **64**, 032001 (2001) [Erratum-*ibid.* D **65**, 039903 (2002)] [arXiv:hep-ph/0102074].

[20] A. D. Martin, R. G. Roberts, W. J. Stirling and R. S. Thorne, "MRST2001: Partons and α_S from Precise Deep Inelastic Scattering and Tevatron Jet Data," Eur. Phys. J. C **23**, 73 (2002) [arXiv:hep-ph/0110215].

[21] J. Pumplin, D. R. Stump, J. Huston, H. L. Lai, P. Nadolsky and W. K. Tung, "New Generation of Parton Distributions with Uncertainties from Global QCD Analysis," JHEP **0207**, 012 (2002) [arXiv:hep-ph/0201195].

[22] G. A. Davis *et al.*, "First DØ Measurement of the Inclusive Jet Cross Section in Run II", DØ Note 4157, 2003.

[23] G. Marchesini *et al.*, HERWIG 5.9, hep-ph/9607393.

[24] T. Sjostrand, L. Lonnblad, S. Mrenna and P. Skands, "PYTHIA 6.3 Physics and Manual," arXiv:hep-ph/0308153.

[25] W. T. Giele, E. W. N. Glover and D. A. Kosower, "The Two Jet Differential Cross Section at $\mathcal{O}({\alpha_s}^3)$ in Hadron Collisions," Phys. Rev. Lett. **73**, 2019 (1994) [arXiv:hep-ph/9403347].

[26] C. Avila *et al.* [E811 Collaboration],"A Measurement of the $p\overline{p}$ Total Cross Section at $\sqrt{s} = 1.8$ TeV," Phys. Lett. B **445**, 419 (1999).

[27] F. Abe *et al.* [CDF Collaboration], "Measurement of the $p\overline{p}$ Total Cross-section at $\sqrt{s} = 546$ GeV and 1800 GeV," Phys. Rev. D **50**, 5550 (1994).

[28] M. Begel and H. Schellman, "On avergaing inelastic cross sections across experiments," DØ Note 4153, 2003.

[29] http://www-d0.fnal.gov/collaboration/Map/D0_Map.gif.

[30] S. Abachi *et al.* [DØ Collaboration], "The DØ Detector," Nucl. Instrum. Meth. A **338**, 185 (1994).

[31] T. LeCompte and H. T. Diehl, "The CDF And DØ Upgrades For Run II," Ann. Rev. Nucl. Part. Sci. **50**, 71 (2000).

[32] B. Squires *et al.*, "Design of the 2 Tesla Superconducting Solenoid for the Fermilab DØ Detector Upgrade", Advances in Cryogenic Engineering **39**, 301, (1994).

[33] R.P. Smith *et al.*, "Preliminary Testing of the DØ Superconducting Solenoid", Advances in Cryogenic Engineering **43a**, 229, (1998).

[34] M.T.P. Roco, "Analysis of SMT Beam Tests Data", DØ Note 3405, 1998.

[35] B. Hoeneisen and D. Lincoln, "Visible Light Photon Counter (VLPC) Absolute Quantum Efficiency and Saturation", DØ Note 3889, 2001.

[36] Personal Communication with Robert Zitoun of DØ and The State University of New York.

[37] G. Hesketh, "Central Track Extrapolation Through the DØ Detector", DØ Note 4079, 2003.

[38] A. Schwartzman and M. Narain, "Primary Vertex Selection", DØ Note 3906, 2001.

[39] A. Kupčo *et al.*, "Measurement of the Dijet Mass Cross Section", DØ Note 4145, 2003.

[40] R. Wigmans, "Calorimetry: Energy Measurement In Particle Physics," Oxford University Press, 2000.

[41] J. Coss *et al.*, "Jet Energy Scale and Resolution for p13 Data and Monte Carlo", DØ Note 4115, 2003.

[42] B. Abbot *et al.*, "Jet Energy Scale at DØ ," DØ Note 3287, 1997.

[43] "DØ Jet and MET ID Properties in p11 and p13", www-d0.fnal.gov/~d0upgrad/d0_private/software/jetid/certification/v2_0/jetid_p13.html.

[44] Personal Communication with Miroslav Kopál of DØ and the University of Oklahoma.

[45] I. Bertram *et al.*, "Single Jet Resolutions at DØ for Run I", DØ Note 3414, 1998.

[46] R. Brun, F. Rademakers and S. Panacek, "ROOT, an Object Oriented Data Analysis Framework," *Prepared for CERN School of Computing (CSC 2000), Marathon, Greece, 17-30 Sep 2000.*

[47] E. Eichten, I. Hinchliffe, K. D. Lane and C. Quigg, "Super Collider Physics," Rev. Mod. Phys. **56**, 579 (1984) [Addendum-ibid. **58**, 1065 (1986)].